

An Investigation into the Feasibility of Electric Propulsion in the Design of a Failsafe Deorbiting Device for End-of-Life Satellites in MEO and GEO.

Gary Stewart

Supervisor: Dr Stuart Grey

*A thesis submitted in partial fulfilment of
the requirements of the MEng Mechanical
Engineering*

2020

Word count: 10494

Abstract

This work investigated the use of electric propulsion as a space-debris mitigation technique for higher altitude satellites. The proposed solutions had to adhere to current industry regulations while reducing the risk of further collisions in orbit. A review of literature was conducted in order to generate research into chemical and electrical space-borne propulsion systems, to generate metrics for comparison between the two different systems. After which a review of potential mission trajectories was discussed as well as the required power systems. A numerical model of a two-body orbit was devised in Python 3.7 to simulate the thrust, J2-effect and aerodynamic-drag acting on the satellite, several qualified thrusters were simulated across a series of orbital altitudes. Thrusters were evaluated in terms of power, mass, cost and manoeuvre times. The results produced two candidates that could manoeuvre a 2000kg satellite from geostationary orbit to a deorbit altitude of 200km; one offered shorter manoeuvre times with reduced power requirements, however, the other offered a significant reduction in propellant mass at the expense of higher power. Utilising electric propulsion over chemical propulsion yielded an average 94.2% propellant saving, which translated to an estimated \$30-65M USD saving from launch.

Acknowledgements

I would like to express my sincere appreciation towards my project supervisor Dr Stuart Grey in agreeing to supervise this project. His enthusiasm, expertise and ingenuity – has been key in formulating and delivering this project. I would like to extend my gratitude for his guidance across the duration of my time with the University of Strathclyde and the Engineering Academy.

I would like to thank my partner, Caroline. The motivation you provided me with each and every day has kept me going through what has been a difficult six months. Your unconditional support and willing ears have allowed me to share the best and worst of it with you - debugging code!

I would like to thank my family, friends and peers who helped me along the way with their interest, advice and encouragement.

Lastly, I would like to dedicate this work to my late mother Wilma Stewart, who sadly now will never read its conclusion but who will always remain the inspiration for its completion.

Contents

Acknowledgements	iii
Table of Figures	vi
Table of Tables	vii
Nomenclature.....	vii
1.0 Introduction	1
1.1 Scope.....	1
1.2 Background.....	1
2.0 Literature Review	3
2.1 Orbital Mechanics	3
2.1.1 Historical Review.....	3
2.1.2 Hohmann Transfer Design	4
2.1.3 Low Thrust Transfer Design	6
2.2 Chemical Propulsion	9
2.2.1 Liquid Rocket Design	9
2.2.2 Solid Rocket Design.....	11
2.2.3 Hybrid Rocket Design.....	12
2.3 Electric Propulsion	13
2.3.1 Electrothermal Thruster Design.....	13
2.3.2 Electrostatic Propulsion Design.....	15
2.3.3 Electromagnetic Thruster Design	17
2.3.4 Thruster Design Comparison	19
2.4 Power System Design.....	22
2.4.1 Power Generation	22
2.4.2 Power Conditioning	25
3.0 Method	26
3.1 Overview	26
3.2 Deriving the System: Two-body Mechanics	27
3.2.1 Newton's Law of Gravitation.....	27
3.2.2 Implementation of Numerical Integrator	28
3.2.3 State Vector to Classical Orbital Elements (COES)	28
3.3 Implementation of Orbital Perturbations.....	30
3.3.1 J2 Effect	30
3.3.2 Aerodynamic Drag.....	31

3.3.3	Thrust	32
3.4	Mission Parameters	33
3.4.1	Thruster Selection	33
3.4.2	Orbit Selection.....	34
3.4.3	Stop Conditions	34
4.0	Results	35
4.1	Simulation Outputs	35
4.2	Model Validation	40
5.0	Discussion.....	41
5.1	Model Limitations	41
5.2	Thruster Evaluation.....	41
5.3	Power Source	42
5.4	Mission & Cost Analysis.....	43
6.0	Conclusions	45
7.0	Further work.....	45
8.0	References.....	46
9.0	Appendices	52
	Appendix 1 – Source code Hyperlink.....	52
	Appendix 2 – Main Script.....	52
	Appendix 3 - Planetary Data File	53
	Appendix 4 - Orbit Propagator	54
	Appendix 5 - Tools.....	61
	Appendix 6 – ‘SAT-1’ Satellite Details	65
	Appendix 7 - Auxiliary Orbital Element Plots	65
	Appendix 8 – Attached Technical Paper.....	66

Table of Figures

Figure 1.2.1 – Spatial density of objects across earths orbits [4]	2
Figure 2.1.1 - Illustration of an orbit using classical orbital elements [9]	3
Figure 2.1.2 - Example of a two burn Hohmann Transfer [9]	4
Figure 2.1.3 - Low thrust spiral transfer [13].	6
Figure 2.2.1 - Simplified P&ID diagram for a monopropellant rocket [26]. ...	10
Figure 2.2.2 - Simplified P&ID diagram for bi-propellant rocket [27].	10
Figure 2.2.3 - Schematic of a solid rocket with ignitors illustrated [27]......	11
Figure 2.3.1 - Schematic of an operational hydrazine Resistojet [34].	13
Figure 2.3.2 - Arcjet concept, with propellant flow path [34].....	14
Figure 2.3.3 - Ion thruster concept: electron bombardment [34].	15
Figure 2.3.4 - Hall effect thruster schematic [34].....	16
Figure 2.3.5 - MPDT concept [34].	18
Figure 2.3.6 - APPT concept [34]......	18
Figure 2.3.7 - Regions of mission utility for EP systems [38].	20
Figure 2.3.8 - Historical use of EP systems in GEO satellites [44]......	21
Figure 2.4.1 - Various performance envelopes for power systems [43].	22
Figure 2.4.2 - Degradation of solar cells from radiation [43].	23
Figure 2.4.3 - Various cells normalized powers values [52].	24
Figure 3.1.1 - Methodology scheme for Chapter 3.1 & Chapter 3.2.....	26
Figure 4.1.1 - Manoeuvre from 7825km to 200km with EP systems	35
Figure 4.1.2 - Manoeuvre from 19100km to 200km with EP systems.	35
Figure 4.1.3 - Simulated manoeuvre from 23222km to 200km with EP	37
Figure 4.1.4 - Simulated manoeuvre from 35786km to 200km with EP	37
Figure 4.1.5 - Mass vs. time performance curve (GEO, BPT4000).....	39
Figure 4.1.6 - Mass vs. time performance curve (GEO, XIPS-25)	39
Figure 5.4.1 - Propellant mass requirements afor EP & CP.....	43
Figure 5.4.2 – Cost of launching propellant across tested altitudes	43
Figure 5.4.3 - GNSS perturbations after decommissioning [6]......	44

Table of Tables

Table 1 - CP and EP thruster performance ranges [38].	19
Table 2 - EP Specifications for thrusters simulated [38] [34].....	33
Table 3 - Results from 7825km with EP systems.....	36
Table 4 - Results from 19100km with EP systems.....	36
Table 5 - Results from 23222km with EP systems.....	38
Table 6 - Results from 35786km with EP systems.....	38
Table 7 - Model validation with initial velocity.	40
Table 8 - Model validation with total mission ΔV 's	40
Table 9 - XIPS-25 with PPS1350 (x2) to highlight the effect of clustering....	42

Nomenclature

<u>Symbol</u>	<u>Description</u>	<u>Units</u>
A	Satellite area	m^2
ATM	Atmospheric direction vector	ms^{-1}
a_{J2}	J2 component of acceleration	ms^{-2}
a_d	Acceleration component due to drag	ms^{-2}
a_t	Acceleration component due to thruster	ms^{-2}
C_d	Coefficient of drag	-
e	Orbital eccentricity	-
E_m	Energy required for manoeuvre	GJ
F_t	Total Thrust Force	N
F_d	Atmospheric drag force	N
g_0	Gravitational Constant for earth	ms^{-2}
h	Angular momentum vector	m^2s^{-1}
H_i	Scale height	m
i	Orbital Inclination	rad
I_{sp}	Specific Impulse	Sec
J_2	Earth's zonal harmonic constant of 2 nd degree	-
M	Mean molecular molar mass	$kg.mol^{-1}$
\dot{m}	Mass flow rate	$kg.s^{-1}$
m_1	Mass of earth	kg
m_2	Mass of satellite	kg

<u>Symbol</u>	<u>Description</u>	<u>Units</u>
m_{prop}	Mass of propellant required for manoeuvre	kg
m_{ppu}	Mass of required power conditioning units	kg
n	Nodal line	m
N	Ratio of initial & final radii	-
R	Gas Constant	-
\vec{r}_1	Radial vector of earth	m
\vec{r}_2	Radial vector, earth to satellite	m
r_i	Initial radial distance of transfer	m
r_f	Final radial distance of transfer	m
T	Mean atmospheric temperature	K
t_m	Time taken to deorbit	seconds
V	Instantaneous magnitude of satellite velocity	ms^{-1}
V_i	Initial velocity of transfer	ms^{-1}
V_f	Final velocity of transfer	ms^{-1}
v_n	Velocity unit vector	-
$V_{\text{sc/atm}}$	Spacecraft velocity relative to atmosphere	ms^{-1}
z	Altitude	m
α	Semi-major axis	m
Δv	Change in Velocity	ms^{-1}
ΔV_H	Hohmann Transfer – change in velocity	ms^{-1}
ΔV	Perturbation Theory – change in velocity for EP	ms^{-1}
μ	Standard gravitational parameter	m^3s^{-2}
ν	True anomaly	rad
ρ	Air density	kgm^{-3}
ρ_{SL}	Air density at sea-level	kgm^{-3}
$\rho(z)$	Air density as a function of altitude	kgm^{-3}
Ω	Rising ascending node	m
ω	Argument of periapsis	rad

1.0 Introduction

1.1 Scope

The work aimed to investigate the feasibility of using electric propulsion (EP) for deorbiting end of life satellites. Several thrusters were simulated across various altitudes to investigate the suitability of the thrusters in terms of power, mass, cost and manoeuvre times. Four thrusters were selected, and system architecture was discussed alongside a cost comparison of chemical propulsion (CP) thrusters to assess the cost-benefit of the transition.

1.2 Background

It had become evident that space debris was a serious issue facing the space industry as early as 1993 with the formation of the Inter-Agency Space Debris Coordination Committee (IADC) [1]. If not suitably addressed, current models indicate that space debris poses a significant risk of setting off a chain reaction known as the Kessler Syndrome [2]. The reaction Kessler described would cause an exponential increase in the creation of new debris through a higher object collision rate, which would elevate the risk above a safe level for space operations. This study investigated EP as a new space debris mitigation strategy which would, when implemented, reduce the risk of further collisions. Furthermore, it was imperative that solutions adhered to the National Aeronautics and Space Administration (NASA) and European Space Agency (ESA) spaceflight guidelines specified below [3] [4].

1. *“The final orbit shall grant a decay time of less than 25 years...”*
2. *“The final orbit must pose no risk to human space flights...”*
3. *“The final orbit shall allow the debris to leave the region within 1 year.”*

The above stipulations were developed to mitigate the risk of collision in protected regions - lower earth orbit (LEO), which covers 200km up to 2000km altitude, and geostationary orbit (GEO), which encompasses an altitude of $35786\text{km} \pm 200\text{km}$ [4]. The proposed deorbit strategy for LEO satellite typically involves a transfer to low altitudes, where atmospheric drag would take effect and induce re-entry [1] [5].

An equivalent deorbit manoeuvre from middle earth orbit (MEO), and GEO requires a substantial change in energy to reach such a low altitude. Due to technical limitations of CP systems, the additional manoeuvre would require a significant increase in fuel storage and incur increased costs, which in most cases make deorbiting from MEO and GEO an unfeasible solution [6]. Therefore, satellite operators tend to use designated graveyard orbits, which were at least $\pm 300\text{km}$ from the operational altitude of the satellite. Such a manoeuvre requires approximately a three-month reserve of propellant fuel, and when the final altitude has been achieved, the electrical and chemical systems were passivated. After which the defunct satellite is expected to have an orbital lifespan of millions of years [7].

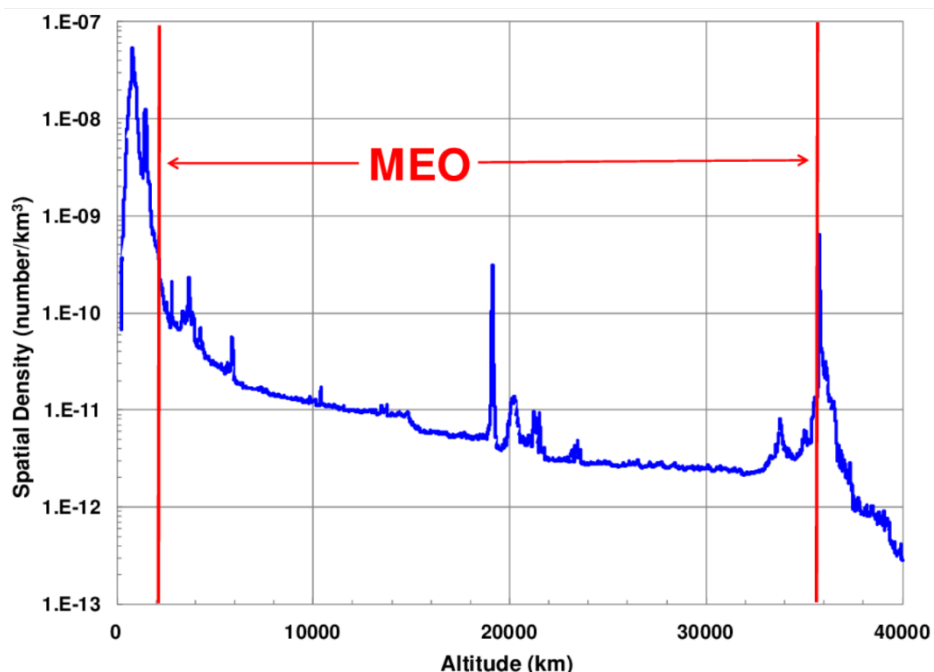


Figure 1.2.1 - Shows spatial density of objects across all of earth's useful orbits [4]

Figure 1.2.1 indicated that the LEO region and GEO region both have substantially higher object densities. However, there is growing concern over the use of graveyard manoeuvres, particularly in the global navigation services satellite (GNSS) region, approximately between 19000km and 23000km [8].

2.0 Literature Review

2.1 Orbital Mechanics

2.1.1 Historical Review

The study of modern astrodynamics can be attributed to Brahe's exhaustive, life-long observations of planetary motion, which upon his death, was passed to his assistant Johannes Kepler. Kepler famously used Brahe's data along with Newton's derivation of the universal law of gravitation, to produce laws of planetary motion, providing geometric descriptors for orbits and the equations for idealised orbital motion. The motion is interchangeably referred to as Keplerian and two-body motion in recognition of both Kepler's and Newton's work on the subject [9]. Kepler's description of orbits, often referred to as classical orbital elements, remains widely used today. Kepler identified six parameters to define the motion of a body in orbit fully, these include; semi-major axis a , eccentricity e , inclination i , right ascension of the ascending node Ω , argument of periapsis ω , and true anomaly ν [10], as illustrated in Figure 2.1.1.

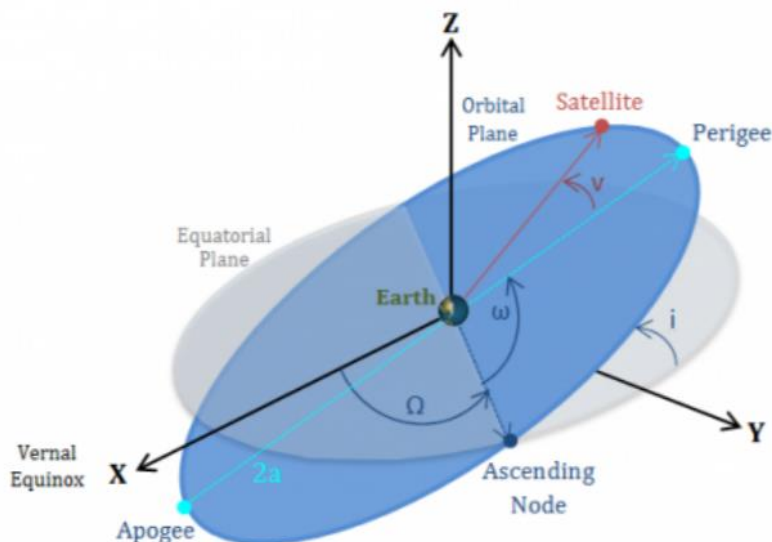


Figure 2.1.1 - Illustration of a Geocentric orbit using classical orbital elements [9]

Figure 2.1.1 illustrated orbital elements within an Earth-centred two-body orbit, except for eccentricity, which defined how far from circular an orbit is. Moreover, figure 2.1.1 defines the periapsis and apoapsis – commonly referred to as perigee and apogee points for earth - as the lowest and highest points respectively on the given orbit.

The orbital elements a, e, i, ω & Ω are constants that define the shape, size and orientation of the orbital motion. However, true anomaly can be defined as the angle between the instantaneous position of the satellite and the defined perigee point and hence, was not constant. Kepler's 1st law stated that bodies in orbit move in conic sections, which encompass circular, elliptic, parabolic and hyperbolic motion. However, the technical content of this work was primarily concerned with reducing circular and quasi-circular orbits with small eccentricities, typical of earth-orbiting satellites [11]. The state of a satellite may alternatively be represented by its position and velocity in cartesian coordinates, which can be referred to as a state vector. Consequently, the velocity vector of a satellite can be stated as the time dependant derivative of its position vector. This representation implied that a satellite's state vector would vary at each time-step throughout a full revolution, where the true anomaly would elapse past 360° and lead to periodic repetition, limiting its usefulness in comparing orbits.

2.1.2 Hohmann Transfer Design

According to Bates et al. [9], orbital transfer design aims to apply an instantaneous change to a satellite's velocity in order to change its trajectory. The instantaneous change in velocity describes the total energy required to make the orbit manoeuvre, often facilitated by fuel expenditure from a propulsion system to generate thrust, the quantity of energy was denoted ΔV . Bates et al. expanded on this and suggested that orbital transfer optimisation commonly looks to minimise ΔV in order to reduce fuel expenditure.

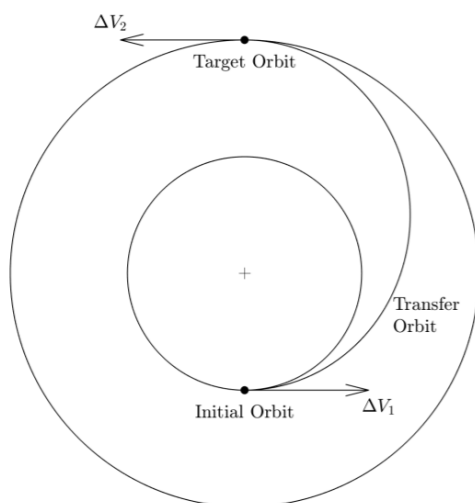


Figure 2.1.2 - Example of a two burn Hohmann Transfer [9]

Perhaps the most notable minimum ΔV transfer was the two burn Hohmann transfer, detailed in Figure 2.1.2. The Hohmann transfer was commonly used to increase a satellite's semi-major axis from an initial orbit by applying a burn proportional to ΔV_1 to reach the desired apoapsis of the transfer orbit. In the instant of the burn, the initial position becomes the periapsis state, yielding a highly elliptical transfer orbit. Once the transfer orbit had been achieved, ΔV_2 was applied at the apoapsis point in order to circularise the orbit. Due to the reversibility of orbits, Schonenberg & Schoyer [5] postulated a strategy for deorbiting a satellite using a solid rocket CP system, modelled on a reversed Hohmann transfer. The manoeuvre required scheduled retrograde burns to decrease the apoapsis velocity until the final circularised orbit had been reached. The final position tends to be within very low earth orbit (VLEO) to allow atmospheric drag to rapidly decelerate and heat the craft to burn up prior to re-entry. The propellant requirement for the manoeuvre adheres to another renowned result, the Tsiolkovsky rocket equation – equation 1.

$$\Delta V = I_{sp} g_0 \ln\left(\frac{m_{sat}}{m_{sat} - m_{prop}}\right) \quad \text{eqn. 1}$$

Where I_{sp} denoted specific impulse, a dimensional ratio measured in seconds, which was used to measure how effectively a propulsion system used propellant mass in order to produce thrust. Moreover, g_0 was the gravitational constant, m_{sat} was the total satellite mass prior to the applied ΔV and m_{prop} was the mass of the satellite after the manoeuvre. I_{sp} was defined below in equation 2:

$$I_{sp} = \frac{F_t}{\dot{m} g_0} \quad \text{eqn. 2}$$

Where F_t was the thrust produced by the propulsive system, \dot{m} denoted the propellant mass flowrate of a thruster. Equation 2 indicated that for a fixed value of thrust a lower mass flow rate yields a greater specific impulse and hence increased fuel efficiency. Equation 1 was rearranged to yield m_{prop} to remonstrate this point.

$$m_{prop} = m_{sat} e^{-\frac{\Delta V}{I_{sp} g_0}} \quad \text{eqn. 3}$$

Equation 3 indicated that if two fictitious thrusters performed an identical manoeuvre which required the same ΔV , the thruster with the greater I_{sp} would yield reduced propellant requirements. However, Goebel, Katz [12] suggested that equation 1 and hence equation 3 are inadequate to evaluate low thrust manoeuvres. Moreover, they indicated that low thrust propulsion methods indeed offer improved ΔV capability but, the assumption of an instantaneous ΔV becomes incorrect, as manoeuvre time t_m has a finite duration. Hence, the substitute terminology for instantaneous ΔV was considered finite burn. Goebel, Katz further suggested that required propellant mass or delivered mass payload were more appropriate measures of trajectory and thruster performance for low thrust manoeuvres.

2.1.3 Low Thrust Transfer Design

Aziz indicated [13] that the span of a low thrust finite burn may last the entirety of the given transfer. An example of a continuous thrust transfer which included the thrust vector direction was shown in Figure 2.1.3. The thrust vectoring approach guided the satellite to target a circular orbit but omitted a small eccentricity and thus, led to a quasi-circular state. To reach the target orbit with no eccentricity and in optimal time, required the implementation of an oscillating vector angle with a variable amplitude throughout the transfer [14].

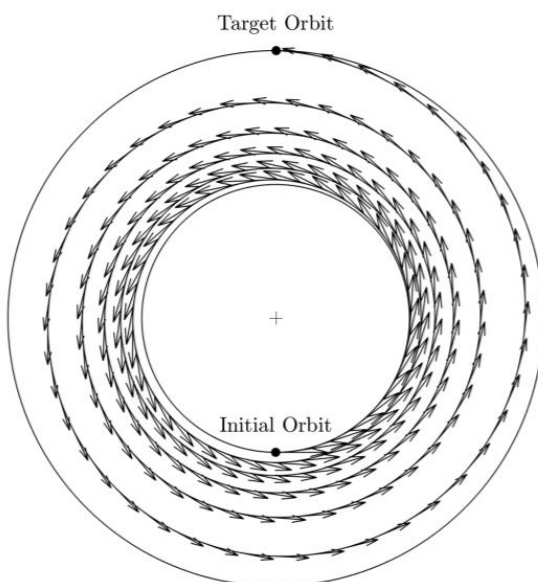


Figure 2.1.3 - Low thrust spiral transfer [13].

In 1961, Edelbaum [15] postulated an approach to solving low thrust manoeuvres between inclined circular orbits by averaging of the Gauss equations. Edelbaum's analytical method in equation 4 was valid for constant thrust F_t , in the direction of the radius vector \vec{r}_2 . Moreover, the equation assumes that the trajectory remains quasi-circular, and that incremental changes to the classical orbital elements are averaged across a full period on orbit. Also, the method was valid through an inclination range of $0^\circ < i < 114.6^\circ$

$$\Delta V = \sqrt{V_i^2 + V_f^2 - 2V_i V_f \cos\left(\frac{\pi}{2} \Delta i\right)} \quad \text{eqn. 4}$$

Edelbaum's assumptions were upheld and his assertions were expanded upon through a series of lectures conducted at MIT [16] which explored approximate analytical expressions for a spiral climb/descent and in-orbit repositioning, or otherwise known, 'walking' manoeuvres. It was demonstrated that the analytical equations are limited by the relationship viewed in equation 5:

$$n > \frac{r_i}{r_f} \quad \text{eqn. 5}$$

Where n represents the number of revolutions required to achieve a manoeuvre given by the ratio of the initial and final radial positions r_i, r_f . Equation 5 indicated that if the number of revolutions was less than the ratio of the initial and final orbit, the manoeuvre cannot be assumed quasi-circular. Moreover, it was stated that the sum of the ΔV required for a given manoeuvre, can be given simply as the difference in the initial and final velocity of the satellite, and is detailed in equation 6.

$$\Delta V \approx V_i - V_f \approx \sqrt{\frac{\mu}{r_i}} - \sqrt{\frac{\mu}{r_f}} \quad \text{eqn. 6}$$

Unlike Hohmann transfers, spiral manoeuvres were constant thrust and non-Keplerian and in most cases were only solvable through numerical integration, where time became a key parameter.

It was noted that ΔV for a spiral manoeuvre would be greater than the equivalent Hohmann transfer, but was useful to assess the efficiency of a low thrust manoeuvre by comparison with an equivalent Hohmann transfer [16]. Longuski et al. [17] outlined a low fidelity approach to modelling low thrust manoeuvres, which entailed the addition of a thrust force to the two-body equation of motion. The two bodies were defined as a satellite with negligible mass, and Earth as a central body. Model fidelity may then be improved by including additional perturbations such as non-spherical gravitation terms, gravity interference of other massive bodies and aerodynamic drag. This approach, although considered non optimal, was implemented in several similar studies to evaluate low thrust manoeuvre technologies on various missions [18] [19].

The circular orbit and constant angle assumptions made in Edelbaum's work [15] were reasonably sound, however, constant thrust was considered a poor model for a satellite powered by EP, as it failed to account for coasting. Colasurdo, Casalino [20] defined coasting as a period of time in which the satellite entered an eclipse period due to Earth's shadow, and thus a satellite would not generate any electricity from a solar source to power the manoeuvre.

Extensive work has since been conducted for non-constant low thrust trajectory optimisation problems. Such as Kechichian, 1997 [21] who reformulated Edelbaum's work and produced semi-analytical equations which account for Earth's shadow, Colasurdo and Casalino [20] expanded on Ketchikan's work for thruster switching while performing hyperbolic escape trajectories. Most valuable to this work was Kluever [22] who evaluated Edelbaum's method for low thrust transfers against solutions for several direct optimisation methods. Kluever selected a 1200kg satellite to perform LEO to GEO and LEO to MEO transfers and surmised that errors between Edelbaum and direct optimisation methods were 0.81% and 0.68% respectively. The numerical method set out by Longuski et al. [17] does not address an Earth shadow eclipse period and therefore introduced an inherent error, however Kluever [22], demonstrated that the percentage error was relatively small and the model could achieve moderate fidelity.

2.2 Chemical Propulsion

Central to the concept of space propulsion was the conservation of momentum. The law of conservation of momentum stated that a force imparted on an object must be accompanied by an equal and opposite reaction force [23]. *Chapter 2.2 & 2.3* primarily focused on investigating means of generating reaction forces through an expulsion of internal mass, widely referred to as propellant. The first and most commonly employed method of producing thrust in space was CP, which produced thrust through a combustion process between a fuel and an oxidiser, occurring typically in a high pressure reaction chamber where high temperature gas was accelerated through a nozzle to provide thrust [24]. CP systems can be categorised into three groups by how the propellant was stored: liquid, solid and hybrid rocket systems. The subsequent review of their design follows in *Chapter 2.2.1, 2.2.2 and 2.2.3*.

2.2.1 Liquid Rocket Design

CP systems that utilise a liquid rocket design store their propellant in pressurised tanks, which were supplied on demand to the combustion chamber. Propellant supply was delivered by either direct pressurisation or a turbopump system, but in each case, high fidelity valves and regulators were required to manage mass flow into the combustion chamber. Liquid CP systems required high temperature combustion to access an improved range of impulse, Huzel and Huang [25] suggested that heat management of the combustion chamber and nozzle section was vital to maintain structural integrity. Propellants for liquid rockets can be stored in a gaseous state. However, since the gaseous state required an increased storage volume and mass, when compared to that what was required for liquid propellant, meant that gas storage was only feasible for small rockets [26]

Monopropellant thrusters rely on a single propellant and were most widely used for satellite attitude and orbit control. Monopropellant systems typically use hydrazine N_2H_4 or hydrogen peroxide H_2O_2 due to their ease of use and throttling capabilities, which leads to less complicated design requirements. Figure 2.2.1 demonstrates a simplified pneumatic and instrumentation diagram, (P&ID) for a monopropellant system.

Turner [27] suggested that a limiting factor for the use of monopropellants via direct pressurisation was the structural mass required to withstand the high static pressure load within the vessel. Moreover, prior to the combustion chamber, operating pressures of monopropellant systems were limited due to the catalyser. This in turn resulted in a low specific impulse range of 150 - 250s.

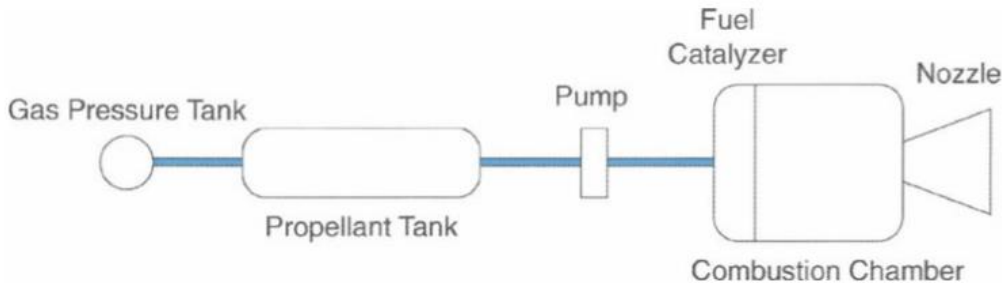


Figure 2.2.1 - Simplified P&ID diagram for a monopropellant rocket [26].

The bipropellant design separated fuel and oxidiser storage and were both independently fed to the combustion chamber, as per Figure 2.2.2. The stability of the feeding process and maintenance of the required mix between fuel and oxidiser, were outlined as critical issues in this rocket type. Bipropellant designs often use a turbopump to deliver pressurised propellant, in order to overcome issues associated with direct pressurisation. The process was powered by using a small proportion of the exhaust gas to drive a gas generator. There were a large variety of fuel combinations available with specific impulses ranging from 200 - 470s.

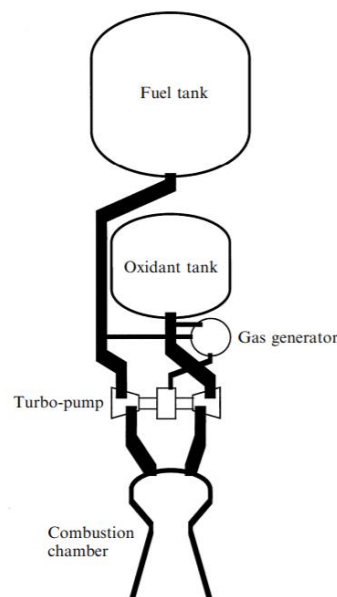


Figure 2.2.2 - Simplified P&ID diagram for bi-propellant rocket [27].

2.2.2 Solid Rocket Design

Fuel and oxidisers were stored together in a granulated form in solid rocket designs; and were typically glued together to form rubber-like materials. Modern propellants were typically based on hydrocarbon rubber synthetics and used ammonium perchlorate as an oxidiser [27]. Kubota [28] suggested that aluminium power was commonly introduced to the propellant as aluminium's thermal properties increase the temperature in the combustion chamber and hence, improved the achievable specific impulse. Figure 2.2.3 illustrated a schematic setup of such a solid propulsion engine. An igniter started the combustion process and the hot gases were expelled through a nozzle in a similar process to liquid propulsion systems.

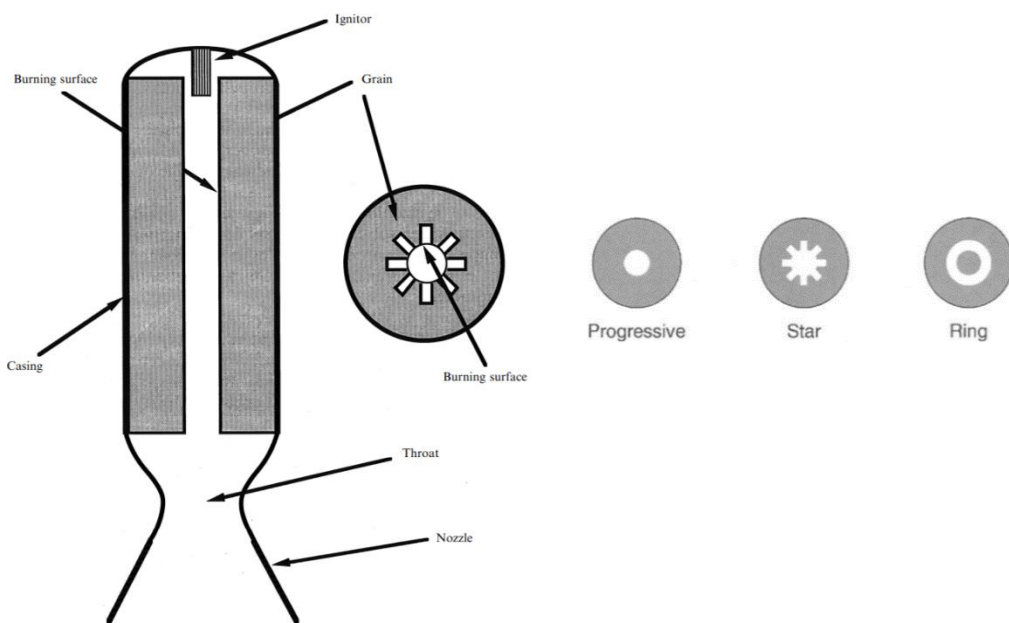


Figure 2.2.3 - Schematic of a solid rocket with varying ignitors illustrated [27].

Solid propellant grains can be arranged in various configurations to influence the thrust profile of a thruster. Figure 2.2.3 shows several common ignitor types. The progressive ignitor burns from the inside surface to the outer surface, this increases both mass flow rate and thrust with respect to time. Star ignitors tend, due to their geometry, to produce constant mass flow rates and hence thrust. The flattest thrust profiles were achieved with a ring ignitor, which has the most intricate design and were typically more costly to manufacture [29].

Some advantages of solid rockets were their simple design and relatively low cost, moreover, solid rockets can yield high mass flow rates which in turn produce high thrusts up to 10^7N . However, the drawback of a solid rocket design was that it cannot easily be stopped once ignited, and specific impulse was relatively low, meaning that a solid rocket design would require additional propellant mass to perform the transfer. Low I_{sp} , additional propellant mass and reliability issues around throttling issues detailed above, excluded solid rocket designs for this study.

2.2.3 Hybrid Rocket Design

Hybrid rockets were conceived to surpass the shutdown and restart problems associated with solid rocket engines, either by storing fuel or oxidiser as liquid and the other in solid form. Conceptually this improves safety and enabled throttling of the engine. Hybrid rockets mostly utilised hydroxyl-terminated polybutadiene as a solid fuel grain, and liquid oxygen as an oxidiser. A distinctive feature of hybrid rocket designs was the low rate of fuel regression, which was found to be approximately 33% that of equivalent solid rocket propellants. Altmann [30] suggested that obtaining hybrid rocket regression rates was significantly more challenging than finding the fuel regression rates in solid rockets.

Consequently, experimental high thrust hybrid rocket designs were created to include multiple perforations, otherwise known as combustion ports, in sections of fuel grain to produce the required fuel surface area to generate thrust. The performance of a hybrid rocket, with respect to I_{sp} depends critically on the degree of flow mixing achieved in the combustion chamber. Zilliac and Karabeyoglu [31] suggest that improved performance in hybrid rocket systems stem from achieving high combustion efficiency. They considered efficiency a direct function of how well unburned oxidiser was exhausted from the combustion chamber, where it would mix with residual fuel from within the boundary layers. Hence, the specific impulse in developed prototypes have been limited to 240 - 270s. Although several studies of hybrid rockets trace back to the space pioneer Hermann Oberth, numerous technical hurdles remain and must be overcome before reliable hybrid rockets were feasible and hence, cannot be considered for this body of work.

2.3 Electric Propulsion

EP was a hypernym for a range of systems that exploit the interaction between an electromagnetic field and charged particles. The interaction was facilitated by the ionisation and acceleration of propellant gas to produce thrust. Although EP systems tend to operate on the same underlying principle, they can be categorised into three groups by how they accelerate particles: electrothermal, electrostatic and electromagnetic [32]. Analysis of the physical phenomena defined above had limited value to the technical study and was out-with the scope of this work. However, an in depth explanation of their physical characteristics can be found in the literature [32] [33]. Therefore, subsequent *Chapter 2.3.1* to *Chapter 2.3.4* reviewed thruster concepts native to each group.

2.3.1 Electrothermal Thruster Design

Electrothermal thrusters use electromagnetic fields to generate plasma in order to increase the overall temperature of the propellant. The thermal energy added to the propellant gas was then converted into kinetic energy by a nozzle. The nozzle can either be structural or created by a manipulation of magnetic fields. Low molecular weighted gases were preferred propellants for these systems. A mature technology within the field of electrothermal propulsion was the resistojet. Figure 2.3.1 shows a sectioned schematic of a hydrazine resistojet, where the propellant was passed through a resistively heated chamber before entering the downstream nozzle.

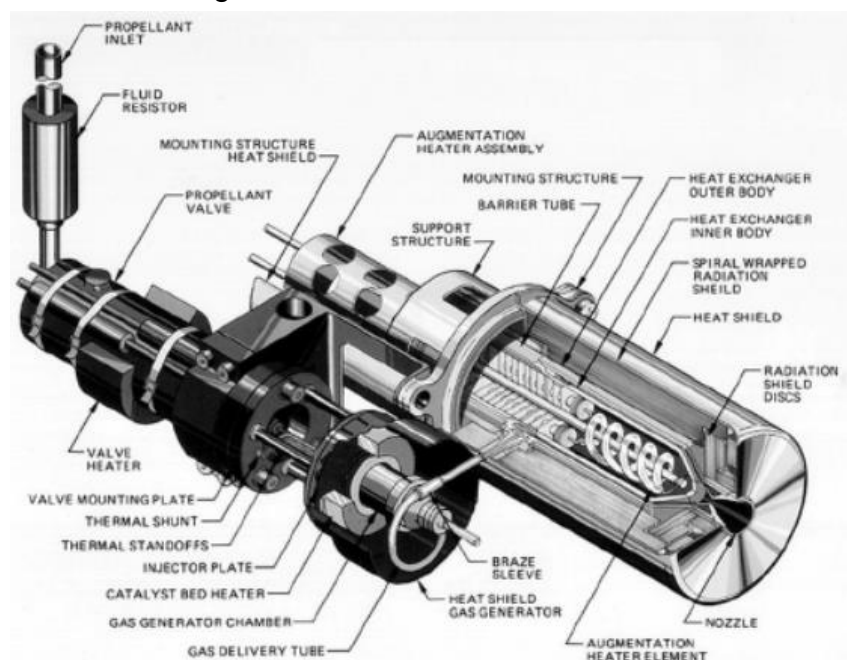


Figure 2.3.1 - Schematic of an operational hydrazine resistojet [34].

A resistojet's acceleration of particles was a function of the thermal heat transfer to the propellant gas and was limited by the material of the walls and heater coils to approximately 3000K. This result limited the resistojet to a modest I_{sp} range of 200 - 400s. Jahn and Choueiri [34] suggested that this I_{sp} range offers only a small improvement in fuel requirements when compared to modern bi-propellant CP systems, as outlined in *Chapter 2.2.1* and hence, has limited value in reducing propellant mas over CP. The arcjet was designed to circumvent material limitations outlined by Jahn and Choueiri [34] by passing high current through an arced wire, streamwise to the propellant gas, between a conical cathode and a downstream annular anode integral, to the exhaust nozzle. The arrangement, which can be viewed in Figure 2.3.2, generated heat in a tightly constricted wire arc that maintained surface temperatures of approximately 30,000K - 50,000K to ionise the flow. Propellant was typically injected into the arc chamber tangentially, where it travelled streamwise in a vortex motion through the arc chamber. The gas was expelled at the nozzle section to a maximum exhaust velocity of around $10,000\text{ms}^{-1}$. Turchi [35] clarified that the relatively low exhaust velocity was due to plasma effects being inconsequential in the electric discharge involved in the propellant path, and as a result the exhaust velocity was low because the propellant was weakly ionised.

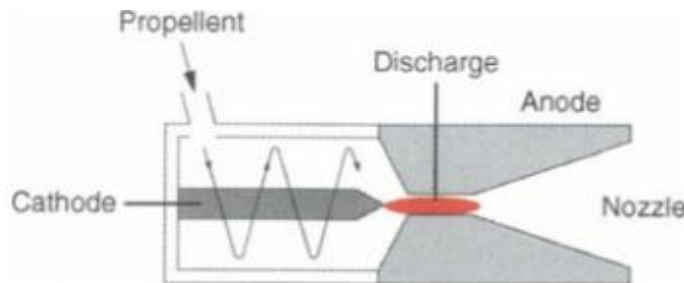


Figure 2.3.2 - Arcjet concept, trajectory of propellant through the system [34].

Much like the resistojet, the arcjet offers a relatively low improvement on CP rockets with an I_{sp} range of 200 - 1000s. Moreover, the upper end of the I_{sp} range remains largely theoretical, and would necessitate a large electrical power, upwards of 10kW, accompanied by a relatively massive power conditioning unit. Therefore, adopting electrothermal propulsion within the design would yield limited benefit as the end of life manoeuvre would require both, a considerable increase in propellant mass, as well as higher power demands, when compared to chemical propulsion [36].

2.3.2 Electrostatic Propulsion Design

Jahn [32] suggested that the fundamental thermal limitations that impede electrothermal thrusters in attaining greater exhaust velocities can be bypassed if the propellant was directly accelerated by an external body force. The most straightforward concept of this nature was the electron bombardment ion thruster, which can use a variety of plasma generation schemes to accelerate atomic ions by way of using an electrostatic field. The concept was illustrated in Figure 2.3.3, where it was detailed that positively charged electrons escaped from the source, and were subsequently accelerated towards an aperture grid, which maintains high voltages of approximately 1000V, which then acted to accelerate the ions by using electrostatic fields to Bohm velocity, the ambipolar speed of sound [37].

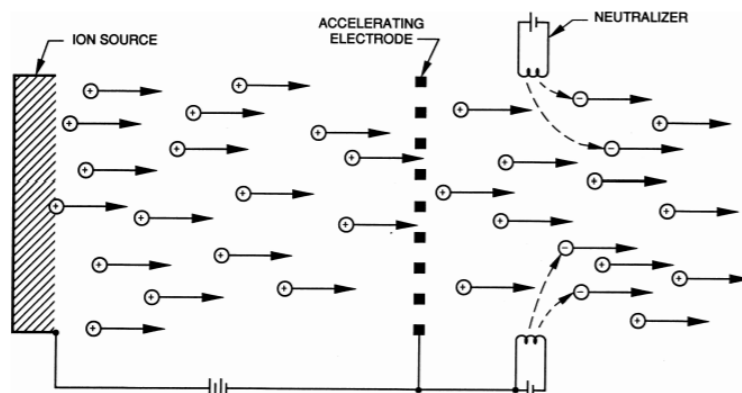


Figure 2.3.3 - Ion Thruster Concept utilising electron bombardment [34].

Once the positively charged ions were accelerated through the aperture grid, the thrust was produced. The neutraliser acted as a hollow cathode and expelled an equal amount of negatively charged electrons to keep the charge of the exhaust gas neutral. Without a neutraliser, the system would build up a negative charge and eventually ions would be drawn back to the thruster, which would reduce thrust and cause erosion. Jahn and Choueiri [34] demonstrated by calculation that exhaust velocities can exceed 10^5 ms^{-1} , the calculation assumed an average electrode geometry, attainable grid voltage and available charge to mass ratio. Moreover, Goebel [12] suggested that ion thrusters have the potential to yield the highest efficiency range of all EP systems and currently vary between 60% to 80% with potential for I_{sp} between 2000 to 10,000s.

However, Sutton & Biblarz [38] suggested that due to the relatively large power requirements, power supply mass penalties scaled strongly with ion thruster designs. Moreover, the concepts typically optimised their thrust efficiencies at too high an exhaust velocity for most near earth and interplanetary missions. The most problematic issue was that regardless of electrode configuration or propellant species, the class of thrusters were severely limited by maximum attainable thrust densities of around 5 N/m^2 . Electrostatic thrust densities were considered trivial when compared to magneto-plasma-dynamic-thrusters, where thrust densities reached 10^4 Nm^{-2} or $10^6\text{-}10^7 \text{ Nm}^{-2}$ achievable with chemical rockets. Hall effect thrusters (HET) were a type of ion drive thruster which can be viewed in Figure 2.3.4, which uses a cross-field discharge described by the Hall effect [39] in order to generate plasma. The electric field is perpendicular to an applied magnetic field, which electrostatically accelerated ions to high exhaust velocities, while the transverse magnetic field inhibits electron motion that would otherwise short the electric field. Jahn [32], and Sutton and Biblarz [38] concurred that although HET efficiency and I_{sp} ranges were lower than those observed in ion thrusters, the electrostatic and magnetic interdependence meant that they were capable of producing higher thrust at a given power. Moreover, HET tended to be of simpler design and required less massive power supplies to operate optimally.

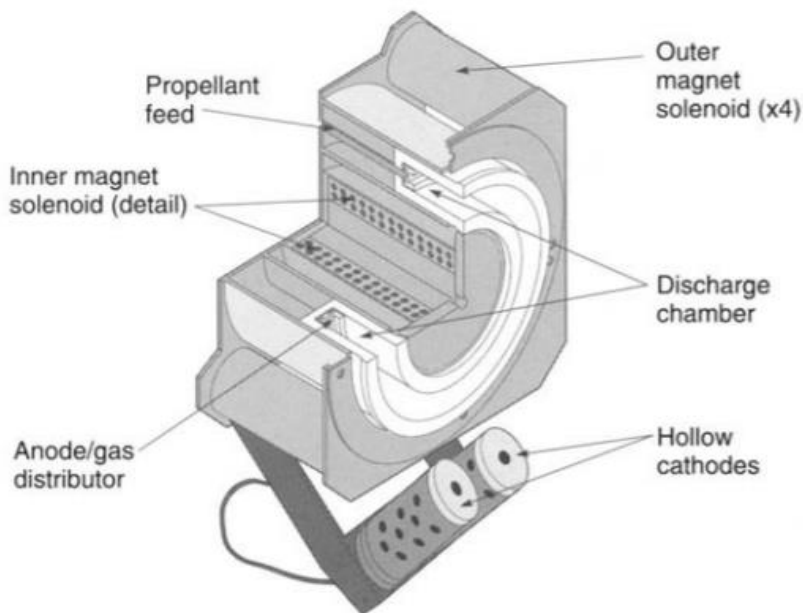


Figure 2.3.4 - Hall Effect Thruster Schematic [34].

Electrospray and Field Emission Electric Propulsion (FEEP) thrusters were two variants of electrostatic propulsion systems which produced small thrusts, typically below 1 mN. Electrospray systems obtained ions from a conductive liquid which was supplied through fine needles; ions were electrostatically accelerated with biased, aligned apertures [34]. Field emission electric propulsion (FEEP) thrusters transport liquid metals - typically indium or caesium - through needles and extract ions from the sharp tip by field emission processes. This branch of electrostatic device was typically suited to precision control of satellite attitude and was not suited to large orbit transfers [40].

2.3.3 Electromagnetic Thruster Design

Electromagnetic thrusters accelerate ionised propellant through self-induced or applied magnetic fields. The accelerating body force was expressed by the Lorentz law [41] and such systems can produce exhaust velocities considerably greater than those observed in electrothermal thrusters, at thrust densities much higher than those noted in electrostatic thrusters. Electromagnetic thrusters realised these improvements as the propellant mass was typically highly ionised but remains neutral at the macroscopic level, and hence was not constrained by total mass flow density, by the space charge limitations observed in electrostatic thrusters. However, Jahn [32] stated that electromagnetic devices tend to be phenomenologically more complex and difficult to analytically model, which may have hindered their development over time. In further contrast to electrothermal and electrostatic classes, electromagnetic acceleration presents a multitude of possibilities for implementation. The applied fields and internal currents may be steady, pulsed, or alternating over a wide range of frequencies. There exists a broad variety of propellant types, including liquids and solids, which may be employed, along with a host of geometries [34]. Magneto-plasma-dynamic thrusters (MPDT) are an established concept of electromagnetic thrusters that can be viewed in Figure 2.3.5, that use large currents through an arc to ionise a large portion of propellant, and then employ electromagnetic forces in the plasma ejection to accelerate the charged propellant.

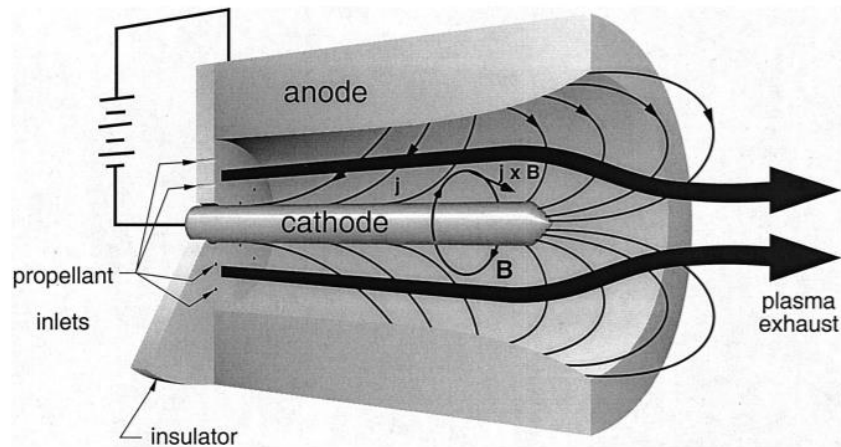


Figure 2.3.5 - MPDT concept [34].

Since the plasma discharge usually generated both the current and the magnetic field, MPDT must operate at very high power to generate enough force for high specific impulse operations [34]. However, the characteristic performance envelope requires at least a minimum of 10kW input power, which indicated the concept was not suitable for this work. Ablative pulsed plasma thrusters (APPT) illustrated in Figure 2.3.6 was a concept developed to overcome MPDT large power requirements. It does so by utilising pulsed discharge to ionise a reaction of a solid propellant, ablated into a plasma arc, and thus using the electromagnetic effects of the pulse to accelerate the ions to high exit velocity. The pulse repetition rate was used to determine the thrust level, but typically Isp ranges from 800 to 1100s and generally operates at relatively low input powers below 1kW. However, Jahn and Choueiri [34] suggest that APPT applications were limited to microsatellites due to their poor efficiency below 15%.

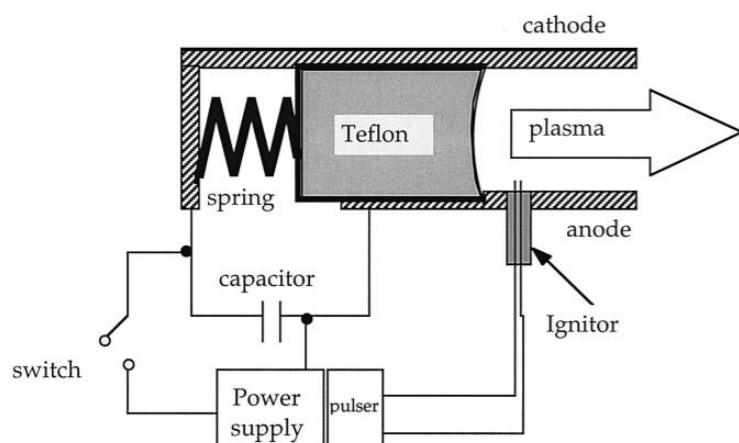


Figure 2.3.6 - APPT concept [34].

2.3.4 Thruster Design Comparison

The advantages of EP were realised by Table 1 along with a restatement of equation 2 from *Chapter 2.1.2*. Recall that I_{sp} was defined as the power to thrust ratio of a propulsion system, and hence defined how efficiently a thruster uses propellant. EP systems typically have a higher I_{sp} range which could yield a factor of ten improvement to payload to mass fractions, due to lower \dot{m} but typically were operated at lower F_t ranges [33]. In order to realise this potential, from herein, thrusters were only considered if their I_{sp} was greater than 1500s.

$$I_{sp} = \frac{F_{thrust}}{\dot{m}g_0} \quad eqn. 2$$

Table 1 - CP and EP thruster performance ranges [38].

Thruster Type	Specific Impulse (sec)	Thrust Range (mN)	Input Power (kW)	Efficiency (%)	Typical Propellant Utilisation
Cold Gas	50-75	500-60000	-	-	Various
Monopropellant	150-250	30-80000	-	-	N_2H_4 H_2O_2
Bipropellant	270-450	30-100000	-	-	Various
Resistojet	200-350	200-300	0.5-1.1	65-90	N_2H_4
Arcjet	400-1000	200-1000	0.9-2.2	25-45	N_2H_4
Ion Thruster	1000-5000	0.01-500	0.4-4.3	40-80	Xenon
Hall Thruster	800-3000	0.01-2000	1.5-4.5	35-60	Xenon
PPT's	850-1200	0.05-10	0.2	7.5-13	Teflon

Table 1 showed that, along with preceding *Chapters 2.3.1 – 2.3.3*, EP was power intensive compared to CP. The limitations of power generation in space were often a deciding factor in selecting propulsion systems [38]. However, the combined effect of improved solar arrays, advanced lithium-ion batteries, and sophisticated power conditioning units led to an increase in satellite power capacity, which was be discussed in detail in *Chapter 2.4* [42].

The study required the identification of a power limit that would be available at end of life for thruster operations, launch power of communications satellites can typically operate from 3kW to 18kW, and hence, the mean value was assumed of 10.5kW [43]. Larson and Pranke [44] suggested that to compensate for efficiencies and degradation of the power systems, across a mission life of 10 to 15 years, the assumption of 20% power loss from degraded power systems was considered appropriate, hence the maximum available power for thrusters to perform the manoeuvre was considered approximately 8kW.

The minimum I_{sp} of 1500s identified above was used along with the assumed maximum 8kW power, with Figure 2.3.7, which identified EP systems' regions of mission utility for various thrusters. Figure 2.3.7 was used in order to select thrusters with the goal of maximising I_{sp} in order to minimise propellant requirements, which made it apparent that HET and ion thrusters were the most suitable candidates for the deorbit manoeuvre.

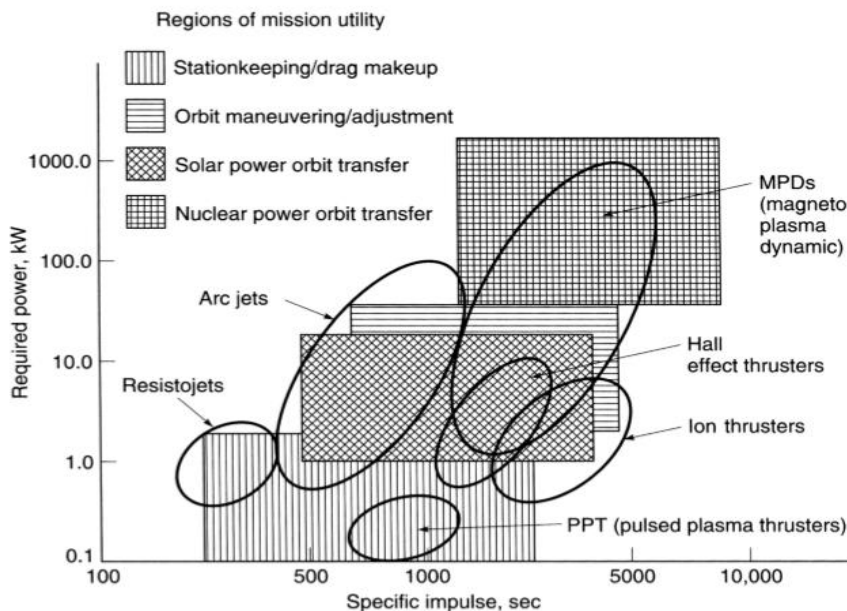


Figure 2.3.7 - Regions of mission utility for EP systems [38].

Furthermore, Figure 2.3.7 indicated that the application of EP requires an optimisation and trade-off of mission objectives, propellant, power supply mass, manoeuvre time and overall system reliability.

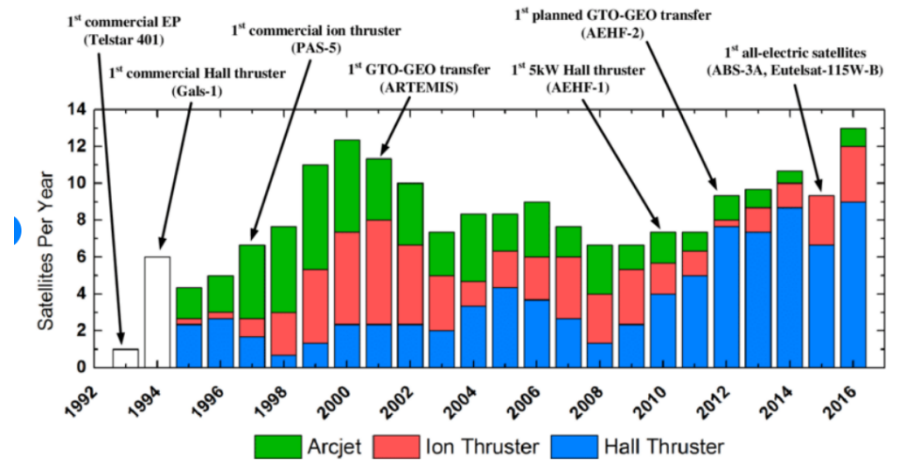


Figure 2.3.8 - Historical use of EP systems in geostationary satellites [44].

Figure 2.3.8 demonstrated an enduring international program of research spanning decades, which led to the use of several EP concepts on satellites in GEO, with the implementation of ion thrusters and HET growing significantly. Chapter 2.3.1 – 2.3.3 elaborated on the designs of various thrusters, ion thrusters and HET were selected for their relatively low power range P_{in} , of 1 – 5 kW and large I_{sp} , ranges of 1000 – 5000s. Moreover, this assertion was supported by a host of successful spaceflight missions such as; GOCE, SMART-1, Hayabusa, Deepspace-1 and Dawn [45] [46] [47].

Moreover, the above technical assertion was supported by an ever-increasing financial incentive from operators, indicative of the attractive I_{sp} range of both ion and HET, as referenced in the below quotation.

“About half the bid requests we receive today include at least an option for electric propulsion. There is a real interest among customers for all electric propulsion. Sometimes it’s even the baseline requirement in the request for proposals. Then it’s a question if its fully electric or just for station keeping or partial orbit raising as a hybrid with chemical, in our view eventually at least 50% of the market will use electric in one way or another.”

Eric Beranger – Former head of space systems, Airbus – April 2015 [48]

2.4 Power System Design

2.4.1 Power Generation

Although Figure 2.4.1 indicated that numerous chemical, nuclear and solar thermal conversion processes had been considered as possible satellite power sources [38], almost all present satellites depend completely on solar arrays and secondary batteries. Consequently, progress in photovoltaic cell technology is critical to the continued growth of EP applications on near earth satellite's [34].

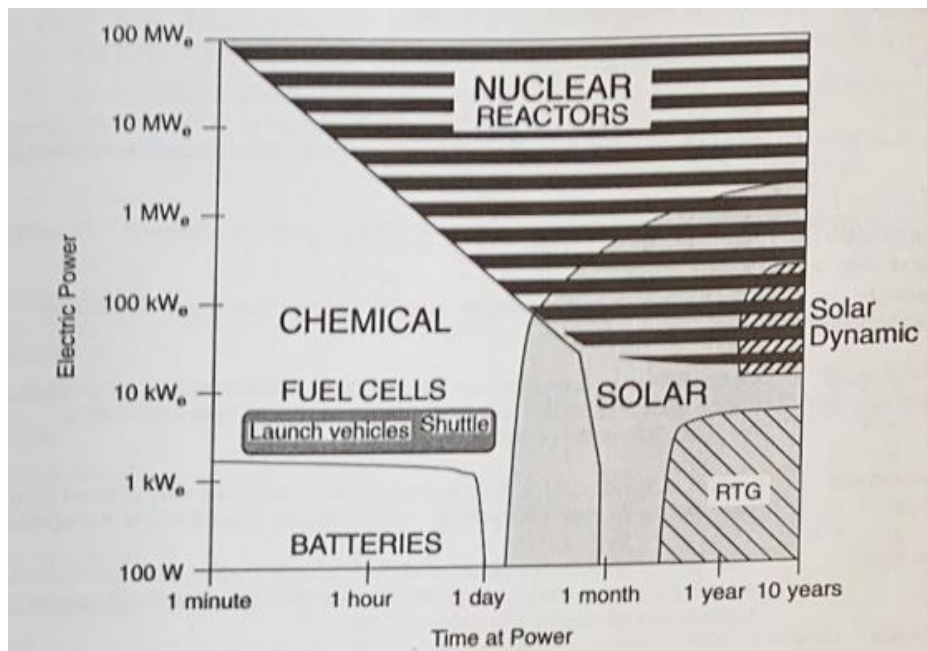


Figure 2.4.1 - Various performance envelopes for power systems [43].

Solar cells rely on the photovoltaic effect, to convert the sun's electromagnetic radiation to electricity. In silicon cells, sunlight generates voltage and a photocurrent across a p-n junction, which operates as an inverse photodiode. Current silicon cell technologies have achieved a maximum of approximately 25% efficiency, however single-junction semiconductors suffer from a theoretical upper limit of 31% [49]. Multi-junction solar cells can circumvent this limitation because, as light passes through the junction, each layer can absorb a separate part of the light spectrum. Recently, Dimroth et al. [50] published that multi-junction arrays have experimentally yielded 46% efficiency with a theoretical upper limit of 86%, which suggested potential for further improvements in efficiency.

Historical improvements in cell efficiency have furthered its use and improved reliability and power available per unit mass. For instance, Jahn [34] and Sutton and Biblarz [38] both stated that standard silicon cells deliver approximately 180 W/m^2 and that arrays can produce 40 W/kg . However, newer, fully space qualified gallium arsenide cells produce 220 W/m^2 and when integrated with parabolic concentrators can produce 100 W/kg .

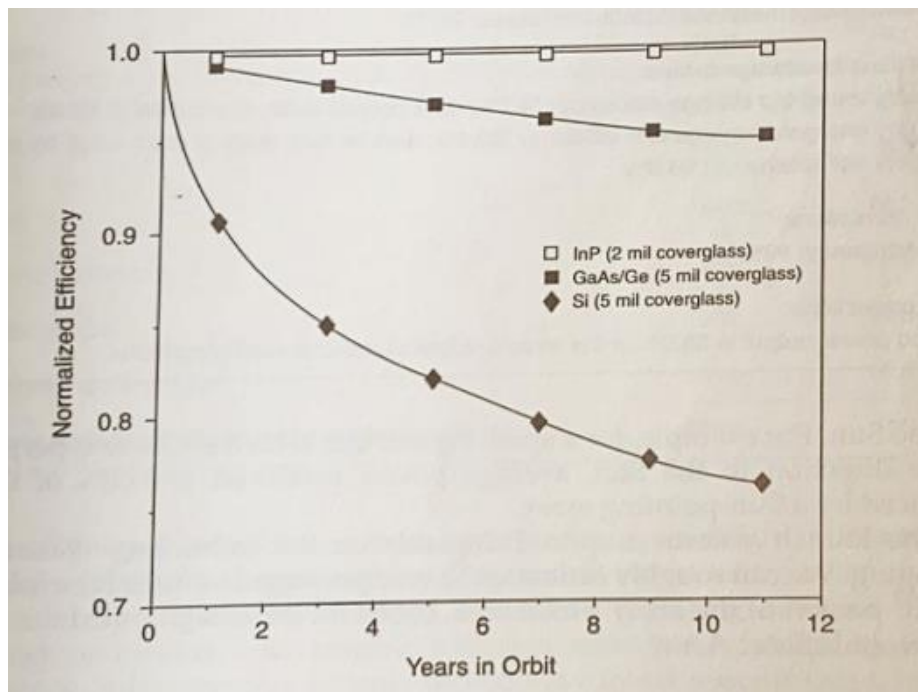


Figure 2.4.2 - Degradation of solar cells from radiation [43].

Figure 2.4.2 compared the radiation resistivity of operational gallium arsenide (GaAs/Ge) and silicone (Si) cells to an indium phosphate (InP) cell, which was still largely under development [44]. Figure 2.4.2 indicated that gallium arsenide cells yielded a significant improvement in radiation resistance over that observed in silicon cells [40]. Other factors that affect the specific mass of a solar array include the solar constant - which fluctuates inversely with the square of the distance from the sun - and the manufactured thinness of the cell [49]. Figure 2.4.3 shows various cells normalised power as a function of altitude on a 60° inclined orbit over a ten-year period - using $75\mu\text{m}$ cover glass. The decreased performance in lower MEO was attributed to an increased radiation particle flux in the region [51]. Moreover, cell performance can be defined as a function of cell temperature; cell performance suffers up to 20% for a 37K increase in operating temperature, and so thermal control was critical in maintaining optimal power generation performance [38].

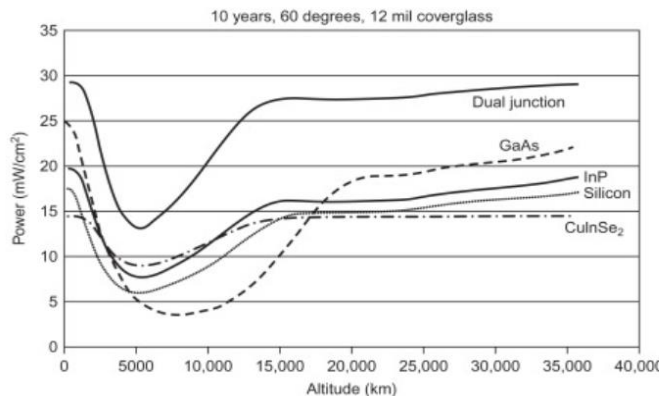


Figure 2.4.3 - Various cell normalized powers as a function of altitude on a 60° inclined orbit for ten years [52].

Solar cells can be fixed, and body mounted to the satellite, or they can be stowed upright and deployed safely once in space. Other developments include flexible panels that were designed to be rolled/unfolded. In addition to the solar arrays, their structure, orientation equipment, deployment mechanisms and other elements including batteries, power conditioning and distribution systems must be accounted for within their design [34]. Solar cell issues related to EP compatibility arise from the fact that historically, solar cell arrays had been designed for 28 VDC output, and EP technologies generally require a magnitude of 1 to 10 kVDC [52]. Kerslake [52] elaborates that new designs have since improved the VDC output of solar arrays - the ISS power bus operates at 160 VDC and the NSTAR and DAWN missions operated on a range of 80 to 160 VDC. Therefore, in order to achieve the required voltage levels, power conditioning as outlined in *Chapter 2.4.2* was required. However, direct drive designs produced increased output voltages of the solar cells, up to 300 VDC and beyond. When direct drive reaches maturity, the production of high output voltages will be considerably simplified, and therefore the power-conditioning equipment required may be reduced or in some cases completely redundant, further improving mass savings [53]. Solar cells have supplied electrical power for a large amount of long-duration space missions and was testament to their reliability. Typically, solar cell arrays were designed for 20% overcapacity to allow for material degradation towards the end of life. Cells loss in performance was primarily due to radiation and particle impact damage, particularly in the radiation belts around the earth, so an increased factor of safety must be considered for the additional end of life manoeuvre [49] [40].

2.4.2 Power Conditioning

As previously discussed, generating and processing large amounts of electrical power in space had been one of the most significant factors limiting EP use. All concepts reviewed in *Chapter 2.3*, with the exception of resistojets, operate at significantly larger voltages than those provided by the standard bus of a solar powered satellite [32] [33][34]. This necessitates the use of power processing units (PPU) that can transpose the power generated from solar arrays to the requisite voltages, currents, and duty cycles. Sutton and Biblarz [38] estimated specific mass β , in terms of kg/kW required to operate various EP systems, and it was surmised that the largest contributing factor to specific mass was PPU and associated power subsystems. Aside from voltage conditioning, each thruster class presented unique problems and demands on the PPU architecture, some of which were still largely in developmental phases. One such problematic example was an electromagnetic PPT, which required the PPU to modulate pulse-forming grids for short, high currents, and hence must obtain high-fidelity time-dependant control over various outputs, while controlling charge and the discharge of condenser systems. Thus, PPTs tend to yield large specific mass at around 50kg/kW but breakthroughs in energy storage capacitors may improve the attractiveness of PPT in future [54].

Whereas, electrostatic thrusters required 1000 to 10,000 VDC; the output of solar cell arrays ranged from 28 to 300 VDC, the incompatibility was addressed with the use of DC-to-DC inverters and step up transformers, which inevitably increased the mass of the overall system [34]. Pinero, Bowers and Lafontaine [55] added that a typical ion thruster PPU can include up to six power supplies and electronics for additional functions. They concluded that the mass of PPU for an electrostatic device was primarily determined by the number of power converters, the switching frequency and power duty. As a result, the PPU complexity of ion thrusters meant that they had the lowest specific mass of considered thruster at approximately 10kg/kW, where HET had a range 6 to 8kg/kW [56]. Only the most mature concepts have underwent flight-qualified development, one of which was the arcjet. With its typical operating voltage peaking at 100 V, the PPU efficiency was rated at 91% and has a specific mass of approximately 2.5kg/kW [34].

3.0 Method

3.1 Overview

The below programme was built using Python 3.7 with NumPy, SciPy and Matplotlib [57] [58]. The source code was made available in appendix¹⁻⁵ and online through [GitHub](#). The methodology outlined in Figure 3.1.1 below details the logic used to implement the scheme, Chapters 3.1 and 3.2 were concerned with detailing the underlying mathematics and physics used to construct the model.

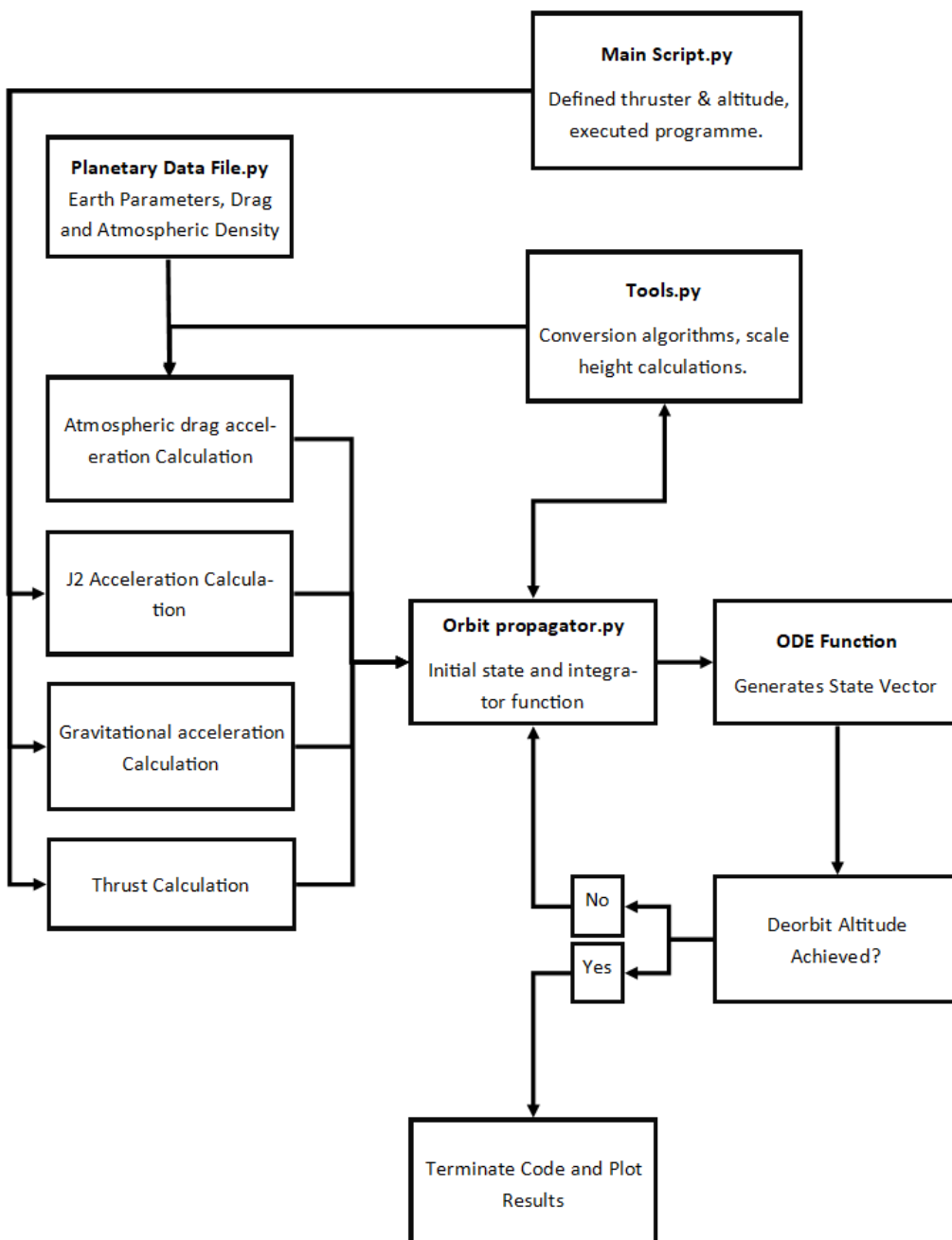


Figure 3.1.1 - Methodology scheme to be detailed in Chapter 3.1 & Chapter 3.2.

3.2 Deriving the System: Two-body Mechanics

Chapter 3.1 detailed key components of building a steady state two-body mechanics problem, which could be used to implement perturbations detailed in *Chapter 3.2*.

3.2.1 Newton's Law of Gravitation

It was pertinent to the body of work to first understand the underlying physics of two-body orbit problems, between a satellite and earth. Both objects were treated as point masses, and in the absence of external forces, the equation of motion for the masses were stated as equation 7 and 8 [59].

$$m_1 \frac{d^2 \vec{r}_1}{dt^2} = G m_1 m_2 \frac{\vec{r}_2 - \vec{r}_1}{|\vec{r}_2 - \vec{r}_1|^3} \quad \text{eqn. 7}$$

$$m_2 \frac{d^2 \vec{r}_2}{dt^2} = -G m_1 m_2 \frac{\vec{r}_2 - \vec{r}_1}{|\vec{r}_2 - \vec{r}_1|^3} \quad \text{eqn. 8}$$

The position vector was defined as $\vec{r}_2 - \vec{r}_1 = \vec{r}$, and hence equation 8 was subtracted from equation 7 and yielded a single equation of motion below, equation 9.

$$\frac{d\vec{v}}{dt} + \mu \frac{\vec{r}}{r^3} = 0 \quad \text{eqn. 9}$$

Where $v = \frac{dr}{dt}$ and $\mu = G(m_1 + m_2)$. The mass of the satellite m_1 was negligible with respect to the mass of the earth m_2 , therefore $\mu = Gm_1$. Newton's law of gravitation was directly integrated, yielding an acceleration vector $a = [a_x, a_y, a_z]$. Equation 9 was defined in the function ODE within the `orbit_propagator` script [60].

3.2.2 Implementation of Numerical Integrator

The integrator LSODA was selected from the SciPy package to numerically evaluate equation 9. LSODA utilised the Adam Bashford multistep method, which produced highly accurate results and reduced computational cost when compared to lower order schemes [61].

3.2.3 State Vector to Classical Orbital Elements (COES)

The programme required a conversion algorithm with an input of cartesian state vectors to COES, to accurately define the manoeuvre in all six degrees of freedom [62] [63]. COES were defined as inclination, eccentricity, rising-ascending node, argument of periapsis, true anomaly and semi major axis as per *Chapter 2.1.1.*

The angular momentum vector denoted h was required for calculating inclination, eccentricity and node line, it was computed by taking the cross product of position and velocity vectors in equation 10. The orbital inclination i , was calculated in equation 11 by dividing h_z by the magnitude of the angular momentum vector.

$$h = r \times \dot{r} \quad \left[\frac{m^2}{s} \right] \quad \text{eqn. 10}$$

$$i = \arccos \frac{h_z}{\|h\|} \quad \text{eqn. 11}$$

Next, the eccentricity vector was calculated from equation 12 where $\mu = \mu_{earth} = 6.67408E-11$. As per equation 13 the node line was computed.

$$e = \frac{h \times \dot{r}}{\mu} - \frac{r}{\|r\|} \quad \text{eqn. 12}$$

$$n = (0 \quad 0 \quad 1)^T \times h = (-h_y \quad h_x \quad 0)^T \quad \text{eqn. 13}$$

The longitude of the rising ascending node Ω , was calculated using equation 14 with applied conditional statements, regarding the input of the node line vector.

$$\text{if; } n_y \geq 0, \quad \Omega = \arccos \frac{n_z}{\|n\|} \quad \text{eqn. 14}$$

$$\text{else; } n_y < 0, \quad \Omega = 2\pi - \arccos \frac{n_z}{\|n\|}$$

Similarly, in equation 15, conditional statements were imposed on the input of eccentricity to calculate the argument of periapsis.

$$\text{if; } e_z \geq 0, \quad \omega = \arccos \frac{\langle n, e \rangle}{\|n\| \|e\|} \quad \text{eqn. 15}$$

$$\text{else; } e_z < 0, \quad \omega = 2\pi - \arccos \frac{\langle n, e \rangle}{\|n\| \|e\|}$$

The required eccentricity was derived from the normalised magnitude of the eccentricity vector, and henceforth, mathematically $e = \|e\|$.

Normalised eccentricity was used to calculate true anomaly v in equation 16.

$$\text{if; } r, \dot{r} \geq 0, \quad v = \arccos \frac{\langle e, r \rangle}{\|e\| \|r\|} \quad \text{eqn. 16}$$

$$\text{else; } \quad v = 2\pi - \arccos \frac{\langle e, r \rangle}{\|e\| \|r\|}$$

Finally, the semi major axis, α was calculated as per equation 17.

$$\alpha = \frac{1}{\frac{2}{\|r\|} - \frac{\|\dot{r}\|^2}{\mu}} \quad \text{eqn. 17}$$

3.3 Implementation of Orbital Perturbations

Perturbations considered were subsequently defined in *Chapter 3.3.1, 3.3.2 and 3.3.3* – their characteristics were specified within the function; `null_perts()` within the `main` script which returned a dictionary. This allowed the use of Boolean logic to turn perturbations on and off while building and testing the model.

3.3.1 J2 Effect

The J2 effect [64], or earth's oblateness, was the strongest perturbation of all the non-spherical J terms, therefore it was practical to consider its effects. The J2 effect was introduced into the model by the addition of the a_{J2} , into equation 18, and was rearranged for acceleration in equation 19, Newton's law of gravitation.

$$\frac{d\vec{v}}{dt} + \mu \frac{\vec{r}}{r^3} + a_{J2} = 0 \quad \text{eqn. 18}$$

$$\therefore a_{xyz} = \mu \frac{\vec{r}}{r^3} + a_{J2} \quad \text{eqn. 19}$$

a_{J2} was calculated with perturbation theory by partially differentiating v_{J2} using the spatial component of position vectors to generate expressions for acceleration in equation 20 [65].

$$\begin{aligned} a_x &= -\frac{\mu \vec{r}_x}{r^3} \left\{ 1 + \frac{3}{2} J_2 \left(\frac{r}{r} \right)^2 \left(1 - \frac{5z^2}{r^2} \right) \right\} \\ a_y &= -\frac{\mu \vec{r}_y}{r^3} \left\{ 1 + \frac{3}{2} J_2 \left(\frac{r}{r} \right)^2 \left(1 - \frac{5z^2}{r^2} \right) \right\} \quad \text{eqn. 20} \\ a_z &= -\frac{\mu \vec{r}_z}{r^3} \left\{ 1 + \frac{3}{2} J_2 \left(\frac{r}{r} \right)^2 \left(3 - \frac{5z^2}{r^2} \right) \right\} \end{aligned}$$

The components of equation 20 were passed as an array into equation 19 and were simply added to the acceleration vector.

3.3.2 Aerodynamic Drag

Aerodynamic drag was considered to have a substantial effect in satellites within lower earth orbit. The magnitude of equation 21 was dependent on a satellites effective area A, velocity magnitude V, variable density value of ρ and a coefficient of drag C_d - which was assumed to be 2.2 [66] [67].

$$F_d = -C_d \cdot A \cdot \rho \cdot \frac{V^2}{2} \quad \text{eqn. 21}$$

The U.S. Standard Atmosphere model 1976 [68] was applied to model variations in atmospheric density at approximately; 60.096km, 251.189km and 1000km, the vector quantity was stored within the `planetary_data_file`.

The first step of the algorithm, equation 22, was to calculate the satellites instantaneous altitude:

$$z = |\vec{r}_2| - |\vec{r}_1| \quad \text{eqn. 22}$$

The algorithm required computation of air density at the satellite's instantaneous altitude. It was assumed that the effects of the atmosphere were negligible above 1000km and hence $\rho = 0$. Therefore, density as a function of altitude can be calculated as equation 23 [69]:

$$\rho(z) = \rho_{SL} \cdot e^{-\frac{z}{H_i}} \quad \text{eqn. 23}$$

Where ρ_{SL} was defined as air density at sea level and H_i was defined as altitude increment where the density decreases by a factor of $e^{-1} \approx 0.4$ which can be derived from gas law relation observed in equation 24;

$$H_i = \frac{RT}{Mg} \quad \text{eqn. 24}$$

Moreover, the atmosphere was not fixed within the earth centred inertial frame and instead rotates with the earth. Equation 25 was used to calculate the motion of the satellite relative to the atmosphere by using the satellite velocity in an earth centred inertial frame and subtracting the cross-product of the atmospheric velocity vector $|ATM|$, and the satellite's position vector.

$$V_{sc/atm} = V - |ATM| \cdot |R| \quad \text{eqn. 25}$$

The atmosphere vector was calculated as per equation 26 by taking one full revolution of earth and dividing it by the hours in one day [70].

$$|ATM| = \frac{2\pi}{86160 \text{ (23 hours 56 minute)}} = |ATM| \hat{z} \quad \text{eqn. 26}$$

The above values were substituted into equation 27 and divided by the satellite mass and added to the acceleration vector.

$$a_d = - \frac{C_d \cdot A \cdot \rho(z) V_{sc/atm}}{m_{sat}} \quad \text{eqn. 27}$$

3.3.3 Thrust

Acceleration provided by EP modules could be calculated using Newton's 2nd law:

$$F_t = m_{sat} \cdot a_t \quad \text{eqn. 28}$$

The thrust vector was given direction by taking the velocity vector V and dividing it by the normalised vector quantity, yielding the unit vector [26]. The parameter was assigned a thrust direction integer of -1 to indicate that the thrust vector must act against the velocity vector, and act as a deorbit manoeuvre.

$$v_n = \frac{[v]}{|v|} \quad \text{eqn. 29}$$

Equation 28 and equation 29 were multiplied together and rearranged to yield equation 30:

$$a_{thrust} = - \left(\frac{[v]}{|v|} \right) \frac{F_{thrust}}{m_{sat}} \quad \text{eqn. 30}$$

All perturbations were then substituted into Newton's law of gravitation which gives the full equation of motion in equation 26.

$$a = \mu \frac{\vec{r}}{r^3} + a_{J2} + a_{drag} + a_{thrust} \quad \text{eqn. 31}$$

3.4 Mission Parameters

3.4.1 Thruster Selection

Table 2 - EP Specifications for thrusters simulated [38] [34].

Thruster	Power (W)	Impulse (sec)	Thrust (mN)	Efficiency (%)	Mass (kg)	Max-Burn (hr)
SPT100D	2500	2200	112	52	4.7	11680
XIPS-25	4250	3550	165	67	13.7	13370
PPS1350	1400	1660	90	55	5.3	9500
BPT 4000	4500	1950	270	59	7.5	8000

Table 2 showed the selected thruster systems that were identified for testing, Table 2 comprises of two HET; Safran's PPS1350 and Aerojet's BPT4000. Ion thrusters to be simulated included OBK Fakel's SPT100D and L3Harris Technology's XIPS-25. The EP systems were selected to represent a broad range of power, I_{sp} and thrust. Their selection was based on available manufacturer data, proven operational history in spaceflight and high max burn times - the maximum recommended time the thrusters should be operated for.

3.4.2 Orbit Selection

Manoeuvres were simulated at altitudes of 7825km, 19100km, 23222km and 35786km using the devised 2000kg satellite ‘SAT-1’ – Appendix⁶ - to assess various thrusters. Two-line element files were extracted from Celestrak API [71] in order to generate accurate satellite input data at epoch 12th March 2020.

3.4.3 Stop Conditions

The study assumed constant power and did not account for an eclipse period. Thus, continuous thrust was applied from the satellite’s initial position until 200km altitude was reached. The final altitude was considered sufficiently deorbited, due to the prominence of atmospheric drag at that altitude [19]. With stop conditions defined, total change in velocity ΔV was calculated as equation 32:

$$\Delta V \approx \sqrt{\frac{\mu}{r_0}} - \sqrt{\frac{\mu}{r}} \quad \text{eqn. 32}$$

The Hohmann transfer detailed in Chapter 2.1.2 was given as equation 33.

$$\Delta V_H = \left(\sqrt{\frac{2\mu r}{r_0(r+r_0)}} - \sqrt{\frac{\mu}{r_0}} \right) + \left(\sqrt{\frac{\mu}{r}} - \sqrt{\frac{2\mu r_0}{r(r+r_0)}} \right) \quad \text{eqn. 33}$$

Hence, by assuming radii r and r_0 were related by $r = Nr_0$ where N was the number of revolutions, the ratio of divergence from Hohmann transfer was calculated as equation 34:

$$\frac{\Delta V}{\Delta V_H} = \left[\sqrt{2 \left(1 + \frac{2\sqrt{n}}{n+1} \right)} - 1 \right]^{-1} \quad \text{eqn. 34}$$

4.0 Results

Chapter 4.1 details simulation results for deorbit manoeuvres across various altitudes with thrusters specified in *Chapter 3.2.3*.

4.1 Simulation Outputs

Figure 4.1.1 showed manoeuvre times from 7825km with selected thrusters with additional data in Table 3. BPT4000 produced the lowest manoeuvre time (t_m) of 4319 hours. PPS1350 took 13045 hours, which disqualified its use, as t_m was out-with the thruster's maximum burn-time of 9500 hours. Disqualified thrusters were highlighted red and suitable thrusters green in Table 3 - 6.

MEO Manoeuvre (7825km) - Altitude vs Time

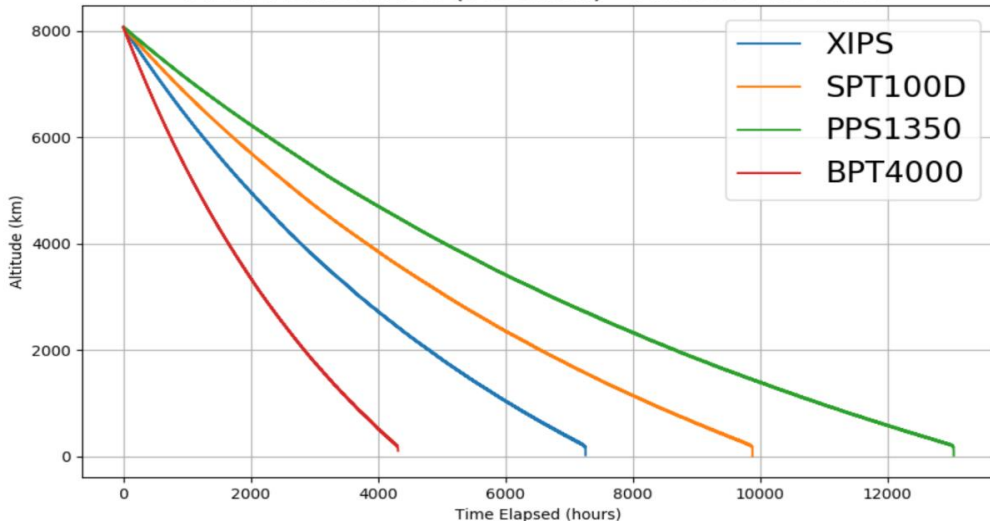


Figure 4.1.1 - Simulated manoeuvre from 7825km to 200km with EP systems

Figure 4.1.2 & Table 4 show results from 19100km, SPT100D was disqualified from use as t_m was 14975 hours with a maximum bur of 11680 hours.

MEO Manoeuvre (19100km) - Altitude vs Time

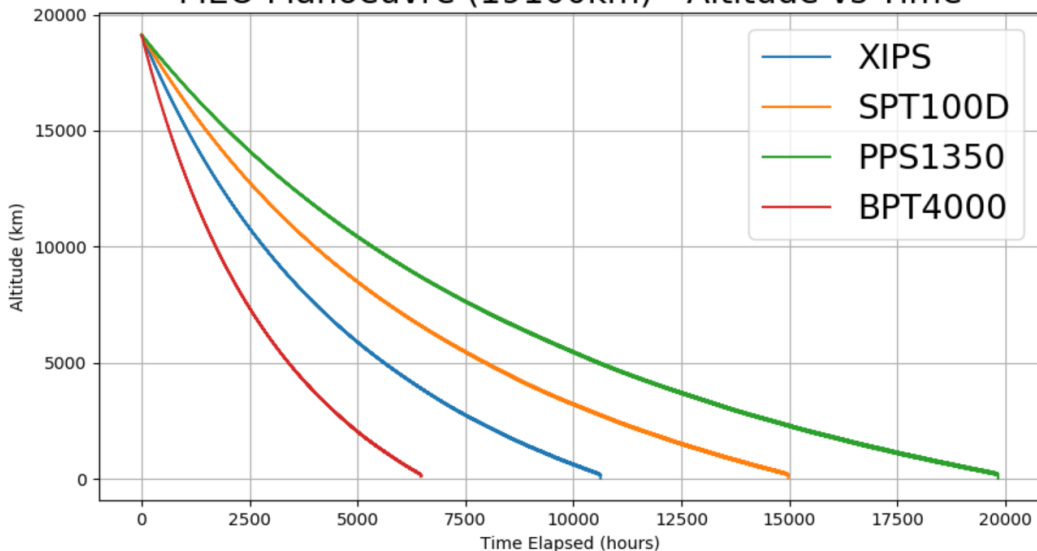


Figure 4.1.2 - Simulated Manoeuvre from 19100km to 200km with EP systems.

Table 3 - Results from 7825km with EP systems, where tm denoted time, Em denoted energy used and M denotes mass.

Manoeuvre from 7825km									
	t_m (second)	M_{prop} (kg)	M_{ppu} (kg)	t_m (hour)	t_m (days)	E_m (GJ)	M_{total} (kg)	$\frac{\Delta V}{\Delta V_H}$	Max Burn Time (Hour)
SPT100D	35581350	184.65	20.83	9883.71	411.82	89	2710.18	1.614	11680
XIPS	26140350	123.85	21.57	7261.21	302.55	111	2659.12	1.614	13370
PPS1350	46962750	259.55	14.14	13045.21	543.55	65.7	2778.99	1.614	9500
BPT 4000	15549750	213.99	24.19	4319.38	179.97	70	2745.68	1.614	8000

Table 4 - Results from 19100km with EP systems, where tm denoted time, Em denoted energy used and M denotes mass.

Manoeuvre from 19100km									
	t_m (second)	M_{prop} (kg)	M_{ppu} (kg)	t_m (hour)	t_m (days)	E_m (GJ)	M_{total} (kg)	$\frac{\Delta V}{\Delta V_H}$	Max Burn Time (Hour)
SPT100D	53911200	279.77	31.25	14975.33	623.97	135	2815.72	1.815	11680
XIPS	38260500	181.27	32.36	10627.92	442.83	163	2727.34	1.815	13370
PPS1350	71408700	394.65	21.21	19835.75	826.49	100	2921.17	1.815	9500
BPT 4000	23305050	320.71	36.29	6473.63	269.73	105	2864.50	1.815	8000

Figure 4.1.3 detailed the manoeuvre from 23222km, due to the weakened gravity field and the relatively small distance, similar results were recorded between 19100km and 23222km – see Table 4 - 5.

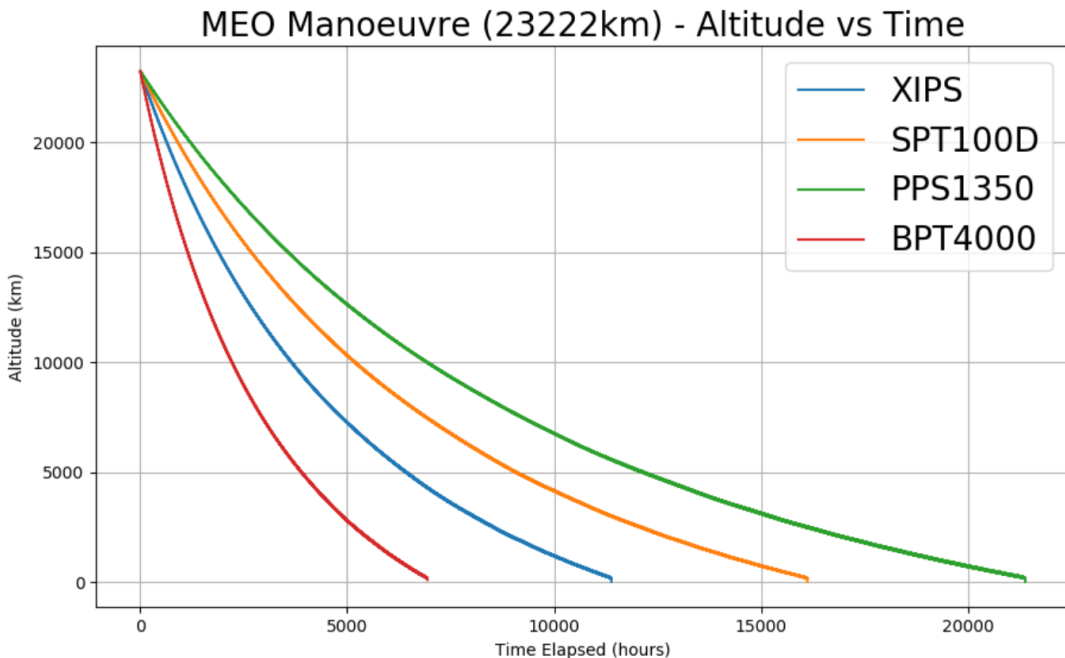


Figure 4.1.3 - Simulated manoeuvre from 23222km to 200km with EP

Figure 4.1.4 highlighted two suitable thrusters for satellites in GEO. XIPS-25 and BPT4000 both have a suitable range for a 2000kg satellite, XIPS-25 greater I_{sp} , yielded a 181kg propellant saving over BPT4000 but takes a further 4270 hours to complete the manoeuvre. Additional COES data for successful manoeuvres can be viewed in Appendix⁷

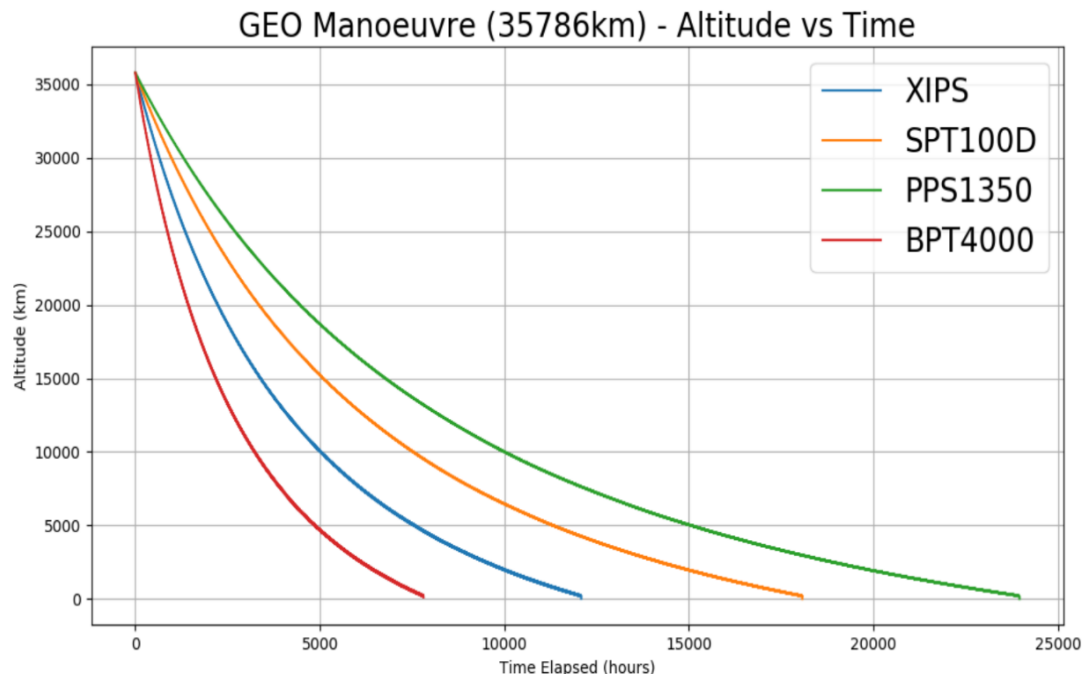


Figure 4.1.4 - Simulated manoeuvre from 35786km to 200km with EP

Table 5 - Results from 23222km with EP systems, where tm denoted time, Em denoted energy used and M denotes mass.

Manoeuvre from 23222km									
	t_m (second)	M_{prop} (kg)	M_{ppu} (kg)	t_m (hour)	t_m (days)	E_m (GJ)	M_{total} (kg)	$\frac{\Delta V}{\Delta V_H}$	Max Burn (Hour)
SPT100D	58027800	301.14	41.67	16118.83	671.62	135	2847.50	1.856	11680
XIPS	40985400	194.19	43.15	11384.83	474.37	163	2751.03	1.856	13370
PPS1350	76990650	425.50	28.28	21386.29	891.10	100	2959.09	1.856	9500
BPT 4000	24946800	343.30	48.39	6929.67	288.74	105	2899.19	1.856	8000

Table 6 - Results from 35786km with EP systems, where tm denoted time, Em denoted energy used and M denotes mass.

Manoeuvre from 35786km									
	t_m (second)	M_{prop} (kg)	M_{ppu} (kg)	t_m (hour)	t_m (days)	E_m (GJ)	M_{total} (kg)	$\frac{\Delta V}{\Delta V_H}$	Max Burn (Hour)
SPT100D	65050650	337.58	52.08	18069.63	752.90	163	2894.36	1.94	11680
XIPS	43494300	206.07	53.93	12081.75	503.41	185	2773.71	1.94	13370
PPS1350	86241300	476.63	35.35	23955.92	998.16	121	3017.28	1.94	9500
BPT 4000	28122600	387.01	60.48	7811.83	325.49	127	2954.99	1.94	8000

Performance plots were generated for BPT4000 and XIPS-25 thrusters at geostationary orbits. Figure 4.1.5 and 4.1.6 showed BPT4000 and XIPS-25, altitude against t_m plots, where mass was incrementally increased by 200kg up to 6000kg. Thrusters t_m increased on average by 35.68 and 57.6 days per increment for BPT4000 and XIPS-25 respectively.

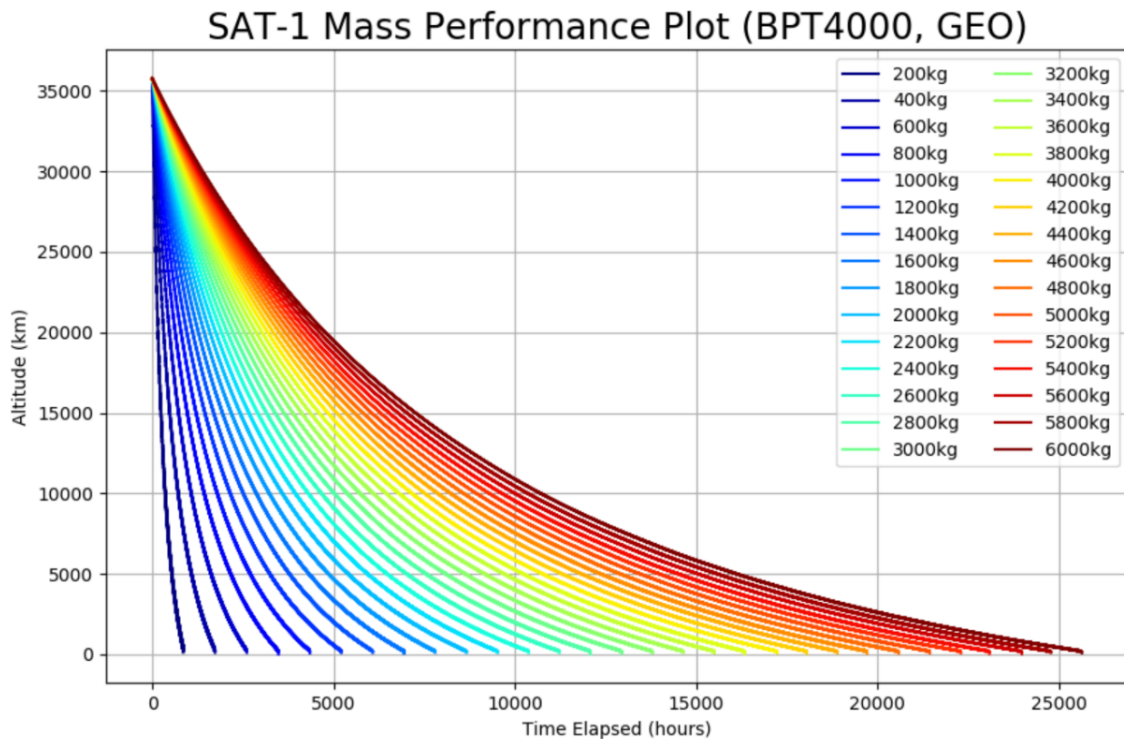


Figure 4.1.5 - Mass vs. time performance curve (GEO, BPT4000)

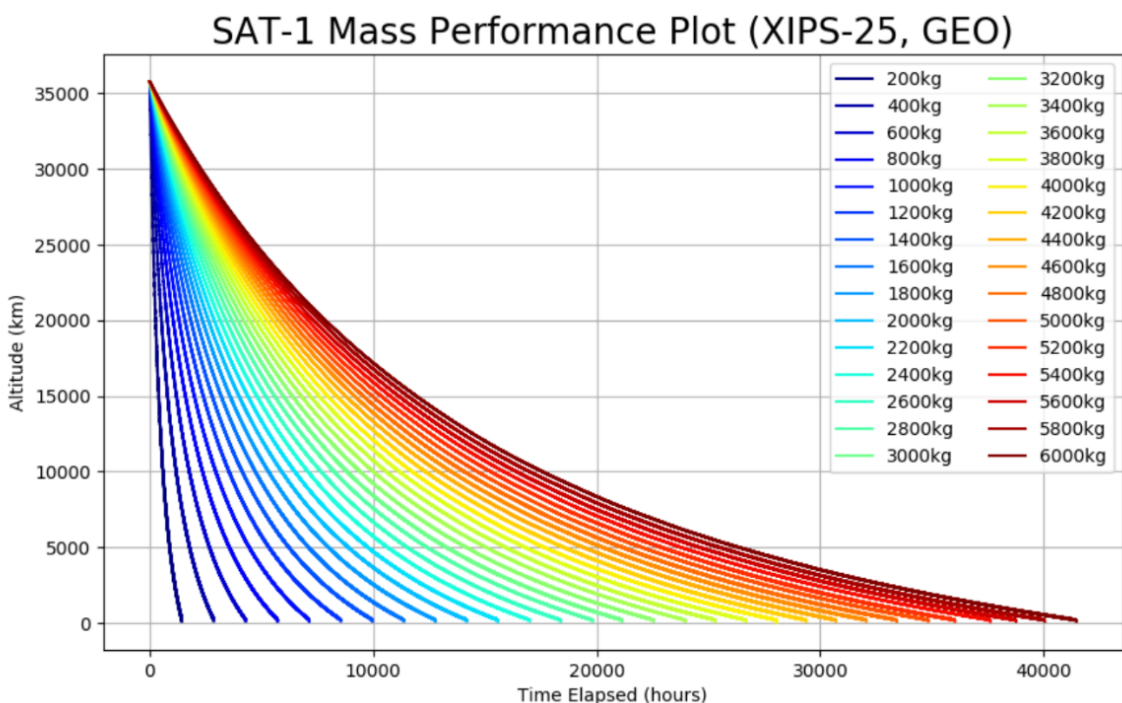


Figure 4.1.6 - Mass vs. time performance curve (GEO, XIPS-25)

4.2 Model Validation

The model was validated in order to confirm accuracy of results. Initial velocities were calculated analytically, and the model results, detailed in Table 7, were printed to the console.

Table 7 - Model validation with initial velocity.

Velocity at Initial Altitude Verification					
Analytical Solution		Model Solution		Calculated Error	
Altitude (km)	Speed (km/s)	Altitude (km)	Speed (km/s)	ABS Error (km/s)	REL Error (%)
7825	5.29780	7825	5.29759	0.00021	0.0040
19100	3.95539	19100	3.95535	0.00036	0.00092
23222	3.66964	23222	3.66963	0.00016	0.00037
35786	3.07464	35786	3.07466	-0.00019	0.00063

The calculated absolute and relative errors shown in Table 7 indicated less than 0.01% error in all recorded instances for initial velocity. The model was built and tested across the range of altitudes, mission ΔV was noted and was calculated analytically for the comparison below, Table 8.

Table 8 - Model validation with total mission ΔV 's

Mission ΔV Verification					
Analytical Solution		Model Solution		Calculated Error	
Altitude (km)	Mission ΔV (km/s)	Altitude (km)	Mission ΔV (km/s)	ABS Error (km/s)	REL Error (%)
7825	2.4874	7825	2.4867	0.00073	0.029
19100	3.8298	19100	3.8289	0.00091	0.023
23222	4.1156	23222	4.1147	0.00093	0.022
35786	4.7106	35786	4.7096	0.00096	0.020

Mission ΔV errors between the analytical and model in the absence of perturbations, yielded an approximate relative error of 0.0242%.

5.0 Discussion

5.1 Model Limitations

Errors outlined in *Chapter 4.2* indicated that results gained were highly accurate and, in all instances, yielded below 0.01% relative error between analytical and model solutions. However, there were inherent limitations with the model that were abstract and difficult to quantify, one limitation was utilising velocity thrust vectoring, which although appropriate for this estimation, was not the optimal method of transfer. Furthermore, the range of perturbations modelled were limited to the J2 effect and aerodynamic drag, as they exerted the most noticeable perturbation effects on the satellite. However, given the length of such manoeuvres, there exists a host of J parameters where, in the interest of greater precision, it would be prudent to model [18]. Further simulations could be undertaken to account for eclipse periods, more J parameters, the moon's gravity alongside the implementation of solar radiation pressure effects. One limitation of deorbiting in this manner would be the manoeuvring of a satellite through debris dense zones with reduced attitude control capacity, which, may increase the risk of a collision with existing debris.

5.2 Thruster Evaluation

A 15-year operational life was assumed, and all simulated manoeuvres achieved deorbit altitude within well within NASA 25-year guidelines [4]. However, the PPS1350 was unsuitable for the range of required manoeuvres. At 7825km, three thrusters (Table 3) could perform the manoeuvre, as their maximum burn time exceeded the t_m . However, at higher altitudes (Table 4, 6) SPT100D exceeded its burn time, hence BPT4000 and XIPS-25 were the only thrusters capable of performing the manoeuvre across all altitudes. BPT4000 could supply 41.07% more thrust and was suitable for manoeuvring heavier satellites but required 170kg more fuel than XIPS-25 to perform a GEO manoeuvre for a 2000kg satellite. Conversely, XIPS-25 improved fuel efficiency came at the expense of greater energy requirements and increased t_m . This study only simulated single thrusters in operation but in many instances multiple thrusters can be clustered together to increase thrust [72]. Clustered configurations were not considered in this work, but their advantages were noted, for comparison the PPS1350 was arranged in a two-thruster arrangement and compared to the XIP-25 available data.

Table 9 - XIPS-25 with PPS1350 (x2) to highlight the effect of clustering.

Thruster Types	Power (W)	Impulse (sec)	Thrust (mN)	Efficiency (%)	Mass (kg)	Run-Time (hr)
XIPS-25 (x1)	4250	3550	165	67	13.7	13370
PPS1350 (x2)	2800	1660	180	55	10.6	9500

Table 9 shows the PPS1350 in a clustered arrangement against XIPS25. PPS1350 remained limited by lower efficiency, maximum runtime and 46.8% of XIPS-25s I_{sp} but PPS1350 required 15.55W/mN where the XIPS-25 requires 25.75W/mN. The two-thruster configuration yielded greater thrust than the XIPS at a significantly lower power, this indicated that the clustered PPS1350 and various smaller systems may be suitable in cluster arrangements. Finally, it was noted that performance curves in Figure 4.1.5 – 4.1.6 indicated failure to deorbit within max burn time occurred at approximately 2100kg. Clustering of larger thrusters (BPT4000, XIPS-25) would increase the payload capacity of the mission but would exceed the power limits defined in *Chapter 2.3.4*.

5.3 Power Source

Energy required (E_m) calculated in Table 3 - 6 excluded the use of batteries as a primary power candidate for the thrusters. An optimistic average of space qualified lithium-ion batteries yielded power densities of approximately $250\text{Wh}.\text{kg}^{-1}$ [73]. Given the duration of the missions, the power supply mass would vary between 70 to 205 metric ton. Solar arrays were a suitable candidate to generate adequate power. Gallium-arsenide cells (GaAs) were favoured over crystalline silicone in space due to higher efficiencies, and greater resistance to radiation which ensures slower degradation [49]. 3-Junction cell arrays yielded an energy density of 321Wm^{-2} which meant that the manoeuvre would require 7.8 to 14.02m^2 of coverage, which would incur additional mass of 90 to 165kg, if the system was to be an autonomously powered. However, mass penalties would be avoided if the satellite had enough power available at the end of mission, but must be appropriately oversized to account for redundancies and failures [74].

5.4 Mission & Cost Analysis.

Mass and cost were inextricably linked for spaceborne systems. Equation 28 was used to determine ΔV_H for the given altitudes, outputs were then substituted into the Tsiolkovsky Rocket equation [75]. This allowed for the calculation of propellant mass required for an equivalent CP mission, the results were plotted in Figure 5.4.1.

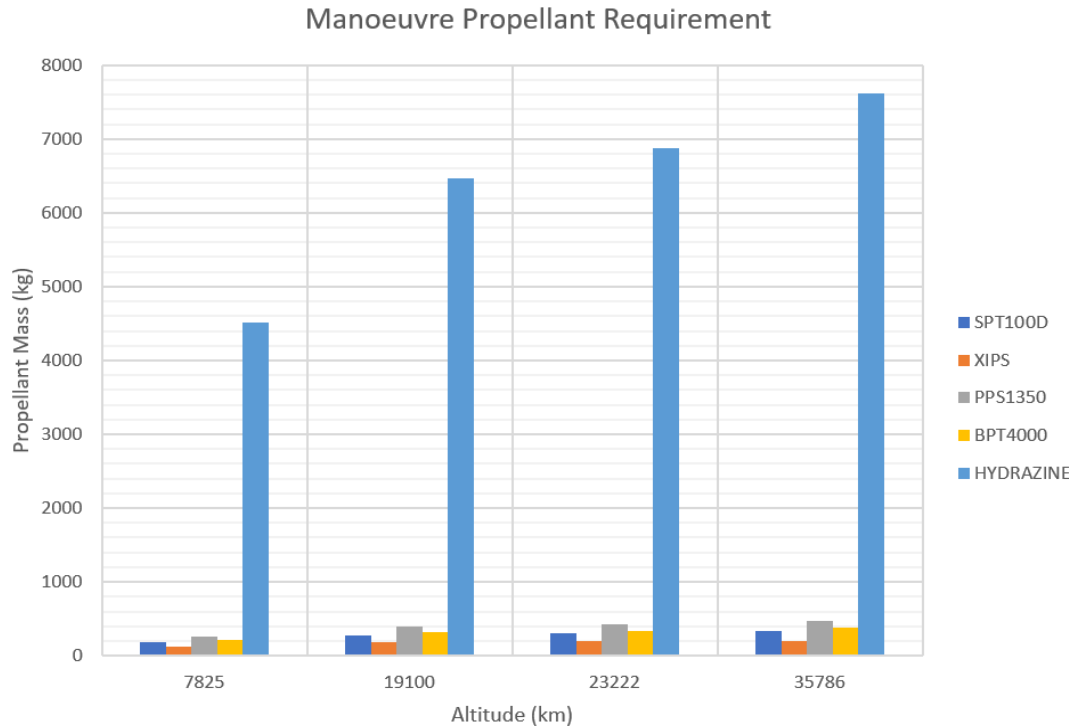


Figure 5.4.1 - Propellant mass requirements at tested altitudes for EP & CP.

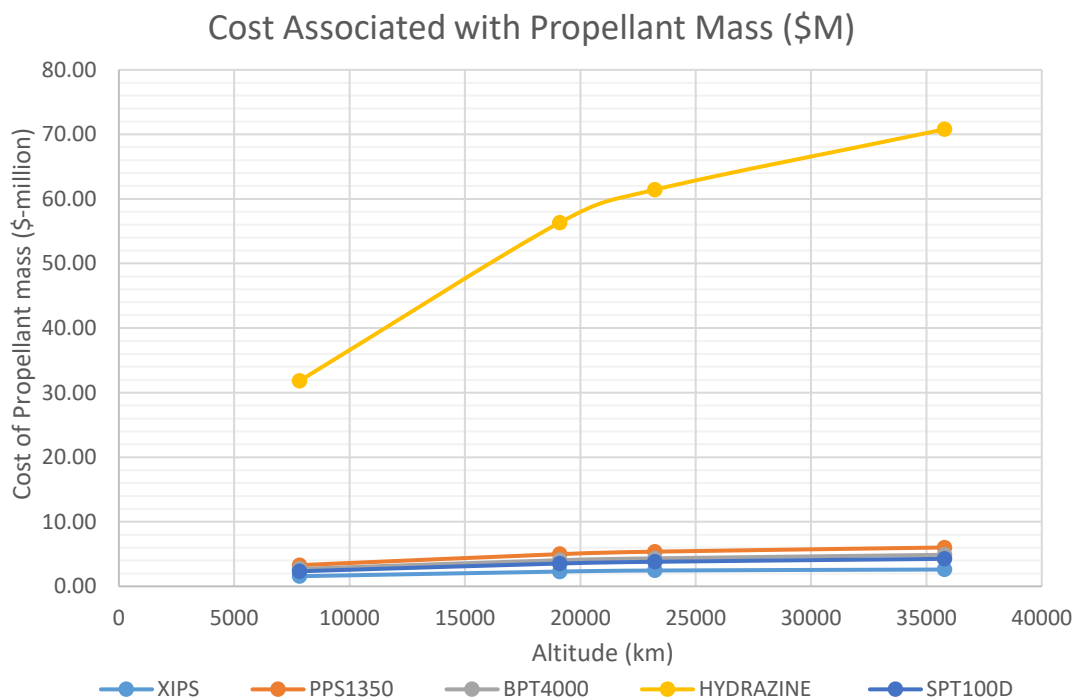


Figure 5.4.2 - Costs associated with launching propellant across tested altitudes

It was assumed the 2000kg satellite was launched into a transfer orbit with a Falcon 9 rocket [76]. The \$/kg (USD) to launch for a Falcon 9 was calculated as 12,618.55\$/kg. Figure 5.4.2 displays propellant cost associated with launch. As expected, the largest propellant cost was incurred at GEO where EP exceeded \$6M, and a hydrazine CP thruster exceeded \$70M which made CP unfeasible for use [37]. Therefore, EP incurred an average propellant saving of 94.2%, yielding \$30 to 65M savings across tested altitudes. The analysis related explicitly to launching extra propellant, and did not pertain to costing the associated technologies.

This work posited that MEO satellite designers and in particular, operators with global navigation system satellites (GNSS) should be considered the biggest benefactor of improved EP technology for deorbiting end of life satellites. Petrovski and Tsuji [8] suggested along with the aid of Figure 5.4.3 that there was although no immediate threat from using graveyard orbits in MEO and GEO orbits. However there existed a medium term risk of GNSS to other MEO satellites within the next 30 year. Long term risks could see a small eccentricity grow and perturbate over time to affect protected LEO and GEO regions after a century.

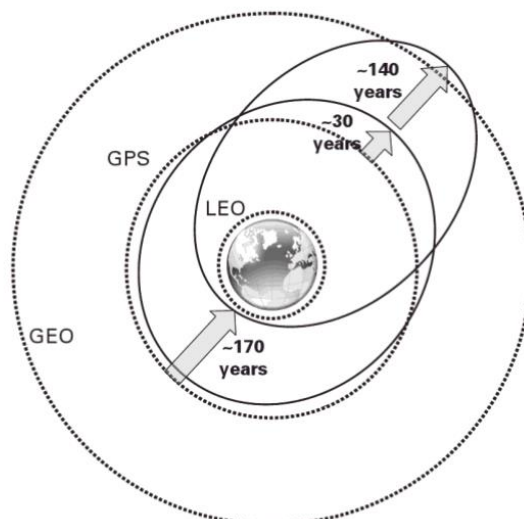


Figure 5.4.3 - GNSS perturbations after decommissioning [6].

Thus, coupling a lack of regulation in the region [8] with the imminent launch of new constellations in coming years [77], suggested that operators within this region should consider the long-term implications of failing to implement more robust measures in deorbiting end of life satellites.

6.0 Conclusions

The study concluded that EP systems were adequate to manoeuvre a 2000kg MEO and GEO end of life satellite to a final orbit of 200km, while conforming with the 25-year mitigation rule, under constant thrust conditions. EP systems would significantly reduce propellant mass requirements. The propellant saving could be used to improve payload capacity or reduce propellant costs by at least a factor of ten. BPT4000 and XIPS-25 were the only thrusters capable of performing within their capacity across all altitudes tested. Their use would require a trade-off between t_m and propellant savings. While BPT4000 and XIPS-25 were the most appropriate single thrusters, the advantages of clustering smaller thrusters in parallel may yield improved t_m over larger single thrusters. In any case, solar arrays seemed the most cost effective, mission ready solution in terms of generating power for the manoeuvre. Battery systems were deemed too heavy as a primary generation system, however rechargeable battery should be considered in mitigating the effects of coasting due to Earth's shadow.

7.0 Further work

Model verification indicated an accuracy greater than 99.99%, but inherent errors detailed in *Chapter 5.1* suggested that further work should account for all J parameter perturbations, the gravity of the moon and solar radiation pressure to gain a higher degree of precision over long time scales. Furthermore, it would be prudent that further work would include an investigation of optimal transfer manoeuvres and hence account for eclipse periods.

Further work must consider the effectiveness and risks associated with applying an ageing control system in coordinating such a manoeuvre and should explore control strategies tasked in mitigating risk of collisions while passing through critical protected altitudes in order to ascertain the associated risks. Lastly, further work would consider an analysis of collision probability in MEO in conjunction with review of regulation with the aim of providing greater foresight in to decommissioning end of life satellites within the GNSS region in MEO.

8.0 References

- [1] N. Johnston, "Origin of the Inter-Agency Space Debris Coordination Committee," National Aeronautics and Space Administration, 2014. [Online]. Available: <https://ntrs.nasa.gov/archive/nasa/casi.ntrs.nasa.gov/20150003818.pdf>. [Accessed 2020 04 19].
- [2] D. Kessler and B. Cour-Palais, "'Collision frequency of artificial satellites: The creation of a debris belt.," *Journal of Geophysical Research*, vol. 83, no. (A6), p. p.2637., 1978..
- [3] Anselmo, P. (ASI), Crowther, T.-S. (BNSC), Alby, Baccini, B. (CNES), A. (DLR), Flury, Jehn and K. (ESA), "'European Code of Conduct for Space Debris Mitigation", no. Issue 2, p. p.6, 2007.
- [4] NASA, "Technical Standard: Process for limiting orbital debris P.41," National Aeronautics and Space Administation , 25 04 2019. [Online]. Available: file:///C:/Users/gary-/Downloads/nasa-std-8719.14b.pdf. [Accessed 21 03 2020].
- [5] R. A. C. Schonenberg and H. F. R. Schoyer, "Solid Propulsion De-orbiting and Re-orbiting," *NASA Astrophysics Data System* , p. p.67, 03 01 2009.
- [6] N. L. Johnston, "Medium Earth Orbits: Is there a need for a third protection region.," NASA, 2010. [Online]. Available: <https://ntrs.nasa.gov/archive/nasa/casi.ntrs.nasa.gov/20100007939.pdf>. [Accessed 16 04 2020].
- [7] J. Leslie and J. Bateman, "Graveyard Orbits and the Satellite Afterlife," National Oceanic and Atmospheric Society , 26 10 2015. [Online]. Available: <https://www.nesdis.noaa.gov/content/graveyard-orbits-and-satellite-afterlife>. [Accessed 01 04 2020].
- [8] I. G. Petrovski and T. Tsuji, "Where do all the satellites go? A satellite life cycle and space garbage," in *Digital Satellite Navigation and Geophysics: A Practical Guide with GNSS Signal Simulator and Receiver Laboratory*, Cambridge, New York, Cambridge University Press, 2012, pp. p.62-66.
- [9] R. R. Bate, D. D. Mueller and J. E. Whit, Fundamentals of Astrodynamics, New Yrok: Dover Publications, Inc., 1971.
- [10] A. D. Vallando, Fundamentals of Astrodynamics and Applications. 4th Edition, New York: Microcosm, 2013.
- [11] T. N. Edelbaum. AIAA Journal, "Optimum Low-Thrust Rendezvous and Station Keeping," *AIAA Journal*, 1964.
- [12] D. M. Goebel, "Ion & Hall Thrusters," in *Fundamentals of electric propulsion*, Hoboken, NJ, Wiley, 2008.
- [13] J. D. Aziz, Low-Thrust Many-Revolution Trajectory Optimization, Colorado: University of Colorado, 2018.

- [14] E. Bryson and Y. C. Ho, *Applied Optimal Control*, Waltham: Ginn and Company, 1969.
- [15] T. Edelbaum, "Propulsion requirements for controllable satellites.," *ARS Journal*, p. 1079–1098, 1961.
- [16] MIT, "Analytical Approximations for Low Thrust Maneuvers," *MIT Openware*, vol. https://ocw.mit.edu/index.htm, p. p.3, 2015.
- [17] J. M. Longuski, J. Guzmán and J. E. Prussing, *Optimal Control with Aerospace*, El Segundo, CA: Microcosm Press, Springer, 2014.
- [18] A. Ionel, "Performance evaluation of propulsion systems as LEO deorbiting devices," *INCAS - National Institute for Aerospace Research*, vol. 9, no. 3, pp. p.55-69, 2017.
- [19] F. Covello, "Application of electrical propulsion for an active debris removal system: a system engineering approach.," *Advances in Space Research (COSPAR)*, vol. 50, no. 918-931, pp. P.3-5, 2012.
- [20] G. Colasurdo and L. Casalino, "Optimal Low-Thrust Maneuvers in Presense of Earth Shadow," *AIAA Papers*, vol. 2004, no. 5087, 2004.
- [21] J. A. Kechichian, "Reformulation of Edelbaum's Low-Thrust Transfer Problem Using Optimal Control Theory," *Journal of Guidance, Control and Dynamics*, vol. Vol 20, no. No. 5, p. p.988–994, 1997.
- [22] C. A. Kluever, "Using Edelbaum's Method to Compute Low-Thrust Transfers with Earth Shadow Eclipsing," *Journal of Guidance, Control and Dynamics*, vol. 34, no. 01 - January, pp. p300-303, 2011.
- [23] N. Hill, "Newtons Third Law Applied to Aerodynamics," NASA, 05 05 2015. [Online]. Available: <https://www.grc.nasa.gov/www/k-12/airplane/newton3.html>. [Accessed 04 04 2020].
- [24] J. M. Lafferty, *Foundations of vacuum science and technology*, New York, N.Y.: J. Wiley and Sons, 1998.
- [25] D. K. Huzel and D. H. Huang, *Design of Liquid Propellant Rocket Engines*, Reston, VA: AIAA, 1992.
- [26] M. Tajmir, "Chemical Propulsion Systems," in *Advanced Space Propulsion Systems*, New York, Springer - verlag wein, 2003, pp. p23-37.
- [27] M. L. Turner, *Rocket & Spacecraft Propulsion*, Chichester, UK: Springer, Verlag-Berlin, 2005.
- [28] N. Kubota, "Survey of Rocket Propellants and their Combustion Characteristics - Chapter 1," *Fundamentals of Solid Propellant Combustion*, vol. Vol 90, pp. p.971-987, 1984.
- [29] S. D. Heister and R. J. Davis, "Predicting Burn Time Variations in Solid Rocket Motors," *Journal of Propulsion & Power*, vol. Vol. 8 , no. No. 3, 1992.
- [30] D. Altman, "Hybrid Rocket Development History," *AIAA Paper*, vol. Vol 91, p. p.2515, 1991.

- [31] G. Zilliac and M. Karabeyoglu, "Hybrid Rocket Fuel Regression Rate Data and Modeling," in *42nd AIAA/ASME/SAE/ASEE Joint Propulsion Conference & Exhibit*, Sacramento, California, 2006.
- [32] R. G. Jahn, Physics of Electric Propulsion, Mineola, New York: Dover Publications, 2012.
- [33] E. Stuhlinger, Ion propulsion for space flight, New York: McGraw-Hill, 1964.
- [34] R. G. Jahn and E. Y. Choueiri, "Electric Propulsion Encyclopedia," *Encyclopedia of Physical Science and Technology*, vol. Volume 5, no. Third edition, pp. p.125-137, 2002.
- [35] P. J. Turchi, "Space Propulsion Analysis and Design," in *Electric Rocket Propulsion System - Chapter 9*, New York, McGraw-Hill, 1995, pp. p509-598.
- [36] D. M. Zube, P. G. Lichon, P. Cohen, D. A. Lichtin and D. V. Cheillini, "Initial on-orbit performance of Hydrazine Arcjets on A2100 Satellites," *AIAA*, p. p99, 1999.
- [37] "MIT, 16.522 Space Propulsion: Lecture 9 Notes: Overview of the Physics in the Plasma Sheath," Massachusetts Institutde of Technology (MIT), 2015. [Online]. Available: https://ocw.mit.edu/courses/aeronautics-and-astronautics/16-522-space-propulsion-spring-2015/lecture-notes/MIT16_522S15_Lecture9.pdf. [Accessed 12 04 2020].
- [38] George P Sutton and O. Biblarz, "Electric Propulsion," in *Rocket Propulsion Elements*, Hoboken, New Jersey, Wiley Interscience, 2010, pp. p.622-658.
- [39] R. Fitzpatrick, "The hall effect," University of Texas, 14 07 2007. [Online]. Available: <http://farside.ph.utexas.edu/teaching/3021/lectures/node74.html>. [Accessed 2020 04 14].
- [40] M. Martinez-Sanchez and J. E. Pollard, "Spacecraft Electric Propulsion - An overview," *Journal of Propulsion and Power*, vol. Vol. 14, no. No. 5, pp. p.688-699, 1998.
- [41] S. Hughes, "The Lorentz Force Law," Massachusetts Institute of Technology, Department of Physics, 2005. [Online]. Available: <http://web.mit.edu/sahughes/www/8.022/lec10.pdf>. [Accessed 12 04 2020].
- [42] E. P. Division, "Satellite Power Systems," Technology Programmes in Space, [Online]. Available: <http://www.esa.int/esapub/br/br202/br202.pdf>. [Accessed 24 02 2020].
- [43] J. Climer, "Boeing Satellite Family," Boeing, 15 05 2015. [Online]. Available: http://www.boeing.com/resources/boeingdotcom/space/boeing_satellite_family/pdf/Bkgd_702SP.pdf. [Accessed 12 04 2020].

- [44] W. J. Larson and L. K. Pranke, "Designing Power Systems," in *Human Spaceflight: Mission Analysis & Design*, New York, McGraw-Hill, 1999, pp. p.643-659.
- [45] NASA, "The Prius of Space," NASA Jet Propulsion Laboratory, September 2007. [Online]. Available: <https://www.jpl.nasa.gov/news/?feature=1468>. [Accessed 26 02 2020].
- [46] W. B. Machine, "Asteroid explorer Hayabusa-mounted ion engin," Internet Archive , 2015. [Online]. Available: <https://web.archive.org/web/20060819093452/http://www.ep.isas.ac.jp/muses-c/>. [Accessed 03 03 2020].
- [47] J. S. Sovey, V. K. Rawlin and M. J. Patterson, "Ion Propulsion Development project in US. Space Electric Rocket Test I to Deep Space 1," *Journal of Propulsion and Space* , vol. Volume 17, no. 3, pp. P.517-526, 2001.
- [48] P. De Selding, "Airbus Charges Ahead with Electric Propulsion," Space - News, 07 04 2015. [Online]. Available: <https://spacenews.com/airbus-charges-ahead-with-electric-propulsion/>. [Accessed 01 04 2020].
- [49] S. Bailey and R. Ryne, "Operation of Solar Cells in a Space Environment," in *Practical Handbook of Photovoltaics*, Amsterdam, Elseveir, 2012, pp. p.863-870.
- [50] F. Dimroth, T. N. Tibbus, M. Niemeyer, F. Predan, P. Beattal and C. Kartcher, "Four-Junction Wafer-Bonded Concentrator Solar Cells," *IEEE; Jounrnal of Photovoltaics* , vol. Vol. 6, no. No. 1, pp. p.343-349, 2016.
- [51] R. Walters, S. Messenger , G. Summers, T. Morton, G. La Roche, C. Signoriri and et al, "Displacement damage dose analysis of the COMETS and Equator-S spacesolar cell flight experiments,,," in *Proceedings of the Sixteenth European Photovoltaic Solar Energy Conference*, Glasgow, 2000.
- [52] T. W. Kerslake, "Effect of Voltage Level on Power System Design for Solar Electric Propulsion Missions," *Journal of Solar Energy Engineering*, vol. Vol. 126, no. No. 3, pp. p.936-944, 2004.
- [53] I. G. Mikellides, G. A. Jongeward, T. Schnieder, m. Hovater, M. R. Carruth, T. Peterson, T. W. Kerslake, D. Snyder, D. Ferguson and A. Hoskins, "Assessment of High-Voltage Solar Array Concepts for a Direct Drive Hall Effect Thruster System," in *AIAA/ASME/SAE/ASEE Joint Propulsion Conference and Exhibit*, Huntsville, Alabama, 2003.
- [54] V. Kim, "Main Physical Features and Processes Determining the Performance of Stationary Plasma Thrusters," *Journal of Propulsion and Power*, vol. Vol. 14, no. No. 5, pp. p.736-743, 1998.
- [55] L. R. Pinero, G. E. Bowers and E. M. Lafontaine, "Development status of a power processing unit for low power ion thrusters," in *36th Joint Propulsion Conference and Exhibit*, Huntsville, Alabama, 2000.

- [56] C. H. McLean, J. B. McVey and D. T. Schappell, "Testing of a U.S Built HET system for orbit transfer applications," *AIAA Paper 99-2574*, 1999.
- [57] T. Oliphant and P. Pearu, "Integration and ODEs (scipy.integrate)," SciPy, 2001. [Online]. Available: <https://docs.scipy.org/doc/scipy/reference/integrate.html>. [Accessed 20 10 2020].
- [58] T. Oliphant, "NumPy v1.19.dev0 Manual," NumPy, 2006. [Online]. Available: <https://numpy.org/>. [Accessed 1 09 2020].
- [59] R. Battin, An Introduction to the Mathematics and Methods of Astrodynamics, NY: AIAA, 1999.
- [60] F. A. Tewari, Atmospheric and Spaceflight Dynamics, Modelling and Simulations with MATLAB and SIMULINK, New York: Springer, 2007.
- [61] J. C. Butcher, "Adams Method," in *Numerical Methods for Ordinary Differential Equations*, Hoboken, Ney Jersey, Wiley, 2003, pp. p105-121.
- [62] P. J. Montenbruck and G. Eberhard, "Keplarian Orbital Elements," in *Satellite Orbits: Models, Methods, Applications.*, New York, Springer, Heidelberg, 2005, p. p28.
- [63] R. Schwarz, "Cartesian State Vectors > Keplerian Orbit Elements (Memorandum #2)," 2017. [Online]. Available: rene-schwarz.com. [Accessed 13 1 2020].
- [64] H. Curtis, "Section 4.7," in *Orbital Mechanics for Engineering Students*, London, Heinemann, 2005, pp. p.177-181.
- [65] H. J. Anton , C. De Ruite and J. R. Forbes, Spacecraft dynamics and control : an introduction, Hoboken, Ney York: Wiley, 2012.
- [66] National Aeronautics and Space Administration,, "The Drag Equation - Glen Research Centre," Glen Research Centre, 2012. [Online]. Available: <https://www.grc.nasa.gov/www/k-12/airplane/drageq.html>. [Accessed 17 01 2020].
- [67] D. M. Prieto, B. P. Graziano and P. C. E. Roberts, "Spacecraft Drag Modelling," *Progress in Aerospace Sciences*, pp. p 2-3, 2016.
- [68] National Aeroautics and Space Administration, "US Standard Atmosphere 1976," NASA, 10 1976. [Online]. Available: <https://ntrs.nasa.gov/archive/nasa/casi.ntrs.nasa.gov/19770009539.pdf>. [Accessed 05 02 2020].
- [69] A. M. Society, "Glossary of Meteorology: Scale Height," American Meteorological Society , 2012. [Online]. Available: http://glossary.ametsoc.org/wiki/Scale_height. [Accessed 12 02 2020].
- [70] S.-H. Chen, "ATM60 - Coriolis Effect," University of California Davis, 2013.
- [71] T. S. Kelso, "Active elements," Celestrak, 01 03 2020. [Online]. Available: <https://www.celestrak.com/Norad/elements/active.txt>. [Accessed 02 03 2020].

- [72] A. Gaudel, C. Hourtolle, J. F. Goester and M. Ottavianni, "De-orbit stratagies with Low Thrust Propulsion," in *Mission Architecture For Active Space Debris Removal Using The Example of SL-8 Rocket Bodies*, Hoboken, Springer, 2015, pp. P.55-59.
- [73] S. Luong, "What is a lithium-ion battery and how does it work?," Clean Energy Institute - University of Washington, 2020. [Online]. Available: <https://www.cei.washington.edu/education/science-of-solar/battery-technology/>. [Accessed 2020 03 09].
- [74] V. M. Andreev, "GaAs and highly efficient space cells," in *Practical Handbook of Photovoltaics: Fundamentals and Applications*, Amsterdam, Elseveir, 2012, pp. p.319-413.
- [75] D. Pettit, "The Tyranny of the Rocket Equation," NASA, 05 01 2012. [Online]. Available: https://www.nasa.gov/mission_pages/station/expeditions/expedition30/tryanny.html. [Accessed 2020 02 25].
- [76] SpaceX, "Capabilities & Services," SpaceX, [Online]. Available: <https://www.spacex.com/about/capabilities>. [Accessed 15 03 2020].
- [77] China Satellite Navigation Office , "Development of the BeiDou Navigation," China Satellite Navigation Office, Bejing, 2019.
- [78] M. Martinez-Sanchez and J. E. Pollard, "Spacecraft Electric Propulsion - An Overview," *Journal of Propulsion and Power*, vol. Vol. 14, no. No. 5, pp. p.688-699, 1998.
- [79] D. Lev, R. Myers, K. Lemmer, J. Kolbeck, M. Keidar, H. Koizumi, H. Liang and et al, "The Technological and Commercial Expansion of Electric Propulsion in the past 24 years," in *35th International Electric Propulsion Conference*, Atlanta, Georgia, 2017.
- [80] ESA, "GNSS Service Centre, Orbital and Technical Parameters," European GNSS Agency, [Online]. Available: <https://www.gsc-europa.eu/system-status/orbital-and-technical-parameters>. [Accessed 04 2020].
- [81] R. L. Easton and M. J. Votaw, "Vanguard IIGY Satellite (1958 Beta)," *Rev. Sci. Instrum*, vol. Vol 30, no. no. 2, pp. p.70-75, 1959.

9.0 Appendices

Appendix 1 – Source code Hyperlink

<https://github.com/Gary-stewart1992/GS-ME409>

Appendix 2 – Main Script

```
##Gary Stewart
##Main Script

import numpy as np
import datetime
from math import sqrt
from mpl_toolkits.mplot3d import Axes3D
import planetary_data_file as pd
import tools as t
from orbit_propagator import orbit_propagator as op
from orbit_propagator import null_perts

#span of time in which the simulation occurs
tspan = 350*24*3600
#time step
dt = 500.0

#loads earths data from the planatery data file
cb=pd.earth

# special variable which defines the code is being written in main script
# and not imported
if __name__ == '__main__':

    #attributes values to the null dictionary defined in orbit propagator
    perts=null_perts()
    perts['thrust']=0.28
    perts['thrust_direction']=-1
    perts['isp']=3550
    perts['J2']=True
    perts['aerodrag']=True
    perts['Cd']=2.2
    perts['A']= 5.2e-6 #km2

    #satellite dry mass
    mass0 = 2000

    #initialises the solver

    op=op(t.tle2coes('EUTELSAT3B.txt'),tspan,dt,coes=True,deg=False,mass0=mass0,perts=perts)

    #plots altitude vs time plot
    op.plot_alts(show_plot=True,hours=True)

    #plots 3D plot
    op.plot_3d(show_plot=True)

    #calculates plots
    op.calculate_coes()

    #plots coes, requires time within bounds of r1 and r2
    op.plot_coes(show_plot=True,hours=True)
```

Appendix 3 - Planetary Data File

```

#Gary Stewart
#Planetary data file

#Imports
import math as m
import datetime
import numpy as np

#Universal constant
G_meters = 6.67408e-11
G=G_meters*10**-9 #required units

#sun dictionary definition
sun={
    'name':'Sun',
    'mass':1.989e30,
    'mu':1.32712e11,
    'radius':695700.0
}

#earth atmospheric array
atm=np.array([[63.096,2.059e-4],[251.189,5.909e-11],[1000.0,3.561e-15]])
#[altitude,density]

#earth value dictionary
earth={

    'name':'Earth',
    'mass':5.972e24,
    'mu':5.972e24*G,
    'radius':6378.0,           #earth radius
    'J2':-1.082635854e-3, #j2 constant
    'deorbit_altitude':0, #deorbit altitude (km)
    'zs':atm[:,0], #altitude (km)
    'rhos':atm[:,1]*10**8, #density (kgm3)
    'atm_rot_vector':np.array([0.0,0.0,72.9211e-6]) #how earth rotates
(rads/s)
}

```

Appendix 4 - Orbit Propagator

Gary Stewart
#Orbit Propagator

```
#Add in packages
import numpy as np
import matplotlib.pyplot as plt
from scipy.integrate import ode
from mpl_toolkits.mplot3d import Axes3D
from matplotlib.lines import Line2D
import Planetary_data_file as pd
import tools as t

#defines hours and days for later use
hours=3600.0
days=hours*24

#empty dictionary to be passed into ODE and defined in main script for
ease
def null_perts():
    return {
        'J2':False,
        'aerodrag':False,
        'thrust':0,
        'thrust_direction':0,
        'isp':0,
        'Cd':0,
        'rho':0,
        'A':0
    }

#define the normalised value of velocity
def norm(v):
    return np.linalg.norm(v)

#define the normalised unit vector for thrusting
def normed(v):
    return np.array(v)/norm(v)

#created class
class orbit_propagator:
    #initialisation
    def
    __init__(self,initial_state,time_span,time_step,coes=False,deg=True,mass0=
    0,perts=null_perts(),cb=pd.earth,propagator='lsoda',sc={}):
        #if coes have been defined as input run this:
        if coes:
            self.r0,self.v0,_=t.coes2rv(initial_state,deg=deg,mu=cb['mu'])

        #else if position and velocity vector defined as input run this.
        else:
            self.r0 = initial_state[:3]
            self.v0 = initial_state[3:]
        self.cb=cb
        self.time_step=time_step
        self.mass0=mass0
        self.time_span=time_span

        #ceil function rounds float up to nearest whole number and int.
        transforms the float to a interger
```

```

        self.n_steps = int(np.ceil(self.time_span/self.time_step))+1

        #initialise arrays
        self.ts=np.zeros((self.n_steps+1,1))
        self.y=np.zeros((self.n_steps+1,7))
        self.alts=np.zeros((self.n_steps+1))

        #7 states (vx,vy,vz,ax,ay,az, mass) preallocating memory (instead
        #of creating a new list, it allowed memory to overwrite existing
        #list
        self.propagator=propagator
        self.step = 0

        #initial condition at first step
        self.y[0,:] = self.r0.tolist() + self.v0.tolist()+[self.mass0]
        self.alts[0]=t.norm(self.r0)-self.cb['radius']

        # initiate solver (lsoda)fast, high order
        self.solver = ode(self.ODE)

        # Adam-Bashford multistep
        self.solver.set_integrator(self.propagator)

        # initial state at t0 defined
        self.solver.set_initial_value(self.y[0,:],0)

        self.perts=perts

        #store stop conditions and dictionary
        self.stop_conditions_dict=sc

        #define dictionary to map internals method
        self.stop_conditions_map={'min_alt':self.check_min_alt}

        #create stop conditions function list with deorbit always checked
        self.stop_condition_functions=[self.check_deorbit]

        #fill in the rest of the stop conditions.
        for key in self.stop_conditions_dict.keys():
            if key in self.stop_conditions_map:

                self.stop_condition_functions.append(self.stop_conditions_map[key])

        #propagate the orbit
        self.propagate_orbit()

        #check if satellite has deorbited
        def check_deorbit(self):
            if self.alts[self.step]<self.cb['deorbit_altitude']:
                print('Satellite deorbited after %.1f seconds' %
self.ts[self.step])
                return False
            return True

        #check if minimum altitude exceeded
        def check_min_alt(self):
            if self.alts[self.step]<self.stop_conditions_dict['min_alt']:
                self.ts_in_hours=self.ts[self.step]/3600.0
                self.ts_in_days=self.ts[self.step]/86400.0

```

```

        print('Satellite reached minimum altitude after %.1f seconds'
% self.ts[self.step])
        return False
    return True

#function called at each timestep to check stop conditions
def check_stop_conditions(self):

    #for each stop condition
    for sc in self.stop_condition_functions:

        #if returns False
        if not sc():

            #stop conditions reached and will return False
            return False

    #if no stop conditions reached, return true.
    return True

#propagate orbit on the initial conditions defined within the init()
function
def propagate_orbit(self):
    print('Propagating orbit...')

    #propagate orbit. check for max time and stop conditions at each
    time step
    while self.solver.successful() and self.step<self.n_steps and
    self.check_stop_conditions():

        # propogate orbit integrator step
        self.solver.integrate(self.solver.t+self.time_step)
        self.step += 1
        self.ts[self.step] = self.solver.t
        self.y[self.step] = self.solver.y
        self.alts[self.step]=t.norm(self.solver.y[:3])-self.cb['radius']

    #extract the position array(60x6) we want all rows and all steps
    up to up to coloum 0,1,2 etc.
    self.ts=self.ts[:self.step]
    self.rs = self.y[:self.step,:3]
    self.vs = self.y[:self.step,3:6]
    self.masses=self.y[:self.step,6]
    self.alts=self.alts[:self.step]

#define ODE
def ODE(self,t_,y,):
    rx,ry,rz,vx,vy,vz,mass = y
    r = np.array([rx,ry,rz])
    v = np.array([vx,vy,vz])

    #norm of the radius vector, linalg is a sub library of numpy for
    linear algebra
    norm_r = np.linalg.norm(r)

```

```

#law of gravitation, as r is vector a has output as a vector
a = -r * self.cb['mu'] / norm_r**3

#J2 acceleration calculation
if self.perts['J2']:

    z2=r[2]**2
    r2=norm_r**2
    tx=r[0]/norm_r*(5*z2/r2-1)
    ty=r[1]/norm_r*(5*z2/r2-1)
    tz=r[2]/norm_r*(5*z2/r2-3)

    #J2 acceleration added to the acceleration vector

a+=1.5*self.cb['J2']*self.cb['mu']*self.cb['radius']**2.0/norm_r**4.0*np.array([tx,ty,tz])

#calculate aerodynamic drag
if self.perts['aerodrag']:

    #calculate altitude and air density
    z=norm_r-self.cb['radius'] # find altitude
    rho=t.calc_atmospheric_density(z) #find air density at given
    altitude

    #calculate motion of s/c with respect to a rotating atmosphere
    v_rel=v-np.cross(self.cb['atm_rot_vector'],r)

    #aerodynamic drag calculation
    drag=-
    v_rel*0.5*rho*t.norm(v_rel)*self.perts['Cd']*self.perts['A']/mass

    #addition of the aerodrag to the acceleration vector
    a+=drag

    #calculate thrust
    if self.perts['thrust']:

        #thrust calculation using newtons 2nd law with vnorm/v to
        calculate thrust direction.

a+=(self.perts['thrust_direction']*t.normed(v)*self.perts['thrust']/mass)/
1000.0

        #calculates mass flow rate
        mass_flow=-self.perts['thrust']/(self.perts['isp']*9.81)

    #returns the [7x1] solution vector
    return [vx,vy,vz,a[0],a[1],a[2], mass_flow]

#COES to be calculated for the plot coes function.
def calculate_coes(self,degrees=True,print_results=False):
    print('Calculating COEs....')
    self.coes=np.zeros((self.n_steps,6))
    for n in range(self.n_steps):

        self.coes[n,:]=t.rv2coes(self.rs[n,:],self.vs[n,:],mu=self.cb['mu'],degree
        s=degrees)
        #function plots the six orbital elements

```

```

def
plot_coes(self,hours=False,days=False,show_plot=False,save_plot=False,title='COES plot',figsize=(16,8)):
    print('Plotting COEs...')
    fig1,axs1 = plt.subplots(nrows=2,ncols=3,figsize=figsize)

    #figure title stated
    fig1.suptitle(title,fontsize=20)

    #x-axis units
    if hours:
        ts=self.ts/3600.0
        xlabel='Time (hours)'

    elif self.days:
        ts=self.days/3600.0/24.0
        xlabel='Time Elapsed (days)'

    else:
        ts=self.ts
        xlabel='Time Elapsed (seconds)'

    #reduced excess space around plot
    fig1.tight_layout(pad=6.0)

    #plotting true anomaly
    axs1[0,0].plot(ts,self.coes[:,3])
    axs1[0,0].set_title('True Anomaly vs. Time')
    axs1[0,0].grid(True)
    axs1[0,0].set_ylabel('True Anomaly (deg)')
    axs1[1,1].set_xlabel(xlabel)

    #plotting semi major axis
    axs1[1,0].plot(ts,self.coes[:,0])
    axs1[1,0].set_title('Semi-Major Axis vs. Time')
    axs1[1,0].grid(True)
    axs1[1,0].set_ylabel('Semi-Major Axis (km)')
    axs1[1,0].set_xlabel(xlabel)

    #plotting eccentricity
    axs1[0,1].plot(ts,self.coes[:,1])
    axs1[0,1].set_title('Eccentricity vs. Time')
    axs1[0,1].grid(True)
    axs1[0,1].set_xlabel(xlabel)

    #plotting argument of periapse
    axs1[0,2].plot(ts,self.coes[:,4])
    axs1[0,2].set_title('Argument of Perigee vs. Time')
    axs1[0,2].grid(True)
    axs1[0,2].set_ylabel('Argument of Perigee (deg)')
    axs1[0,2].set_xlabel(xlabel)

    #plotting inclination
    axs1[1,1].plot(ts,self.coes[:,2])
    axs1[1,1].set_title('Inclination vs. Time')
    axs1[1,1].grid(True)
    axs1[1,1].set_ylabel('Inclination (deg)')
    axs1[1,1].set_xlabel(xlabel)

    #plotting raan

```

```

        axs1[1,2].plot(ts,self.coes[:,5])
        axs1[1,2].set_title('RAAN vs. Time')
        axs1[1,2].grid(True)
        axs1[1,2].set_ylabel('RAAN (deg)')
        axs1[1,2].set_xlabel(xlabel)

        if show_plot:
            plt.show()

        if save_plot:
            plt.savefig(title+'.png',dpi=500)

    def
plot_alts(self,show_plot=False,save_plot=False,hours=False,days=False,title='alt plot',figsize=(16,8),dpi=500):

    #define x axis units
    if hours:
        ts=self.ts/3600.0
        xunit='Time Elapsed (hours'

    elif self.days:
        ts=self.days/(3600.0/24.0)
        xunit='Time Elapsed (days'

    else:
        ts=self.ts
        xunit='Time Elapsed (seconds)'

    #states figure size in function definition
    plt.figure(figsize=figsize)

    #plots empty graph
    plt.plot(ts,self.alts, Label="XIPS-25")

    if show_plot:                      #show plot
        plt.show()
    if save_plot:
        plt.savefig(title+'.png',dpi=dpi)

#3D visual plot
def plot_3d(self,show_plot=False,save_plot=False, title='Deorbiting Manoeuvre Trajectory',dpi=500):

    #projection - '3d' essential import
    fig0 = plt.figure(figsize=(16,8))

    #add subplot 111 - 1st row,1st column 1st value
    ax0 = fig0.add_subplot(111,projection='3d')

    #plots trajectory and starting point
    ax0.plot(self.rs[:,0],self.rs[:,1],self.rs[:,2],'k',
label='Trajectory') #trajectory
    ax0.plot([self.rs[0,0]],[self.rs[0,1]],[self.rs[0,2]],'ko', label ='Initial Position') #initial position

    #creates spherical earth as sub-plot

```

```

_u,_v = np.mgrid [0:2*np.pi:20j,0:np.pi:20j] # define sphere
_x = self.cb['radius'] * np.cos(_u) * np.sin(_v)      # trig
_y = self.cb['radius'] * np.sin(_u) * np.sin(_v)      # trig
_z = self.cb['radius'] * np.cos(_v)                   # trig

#surface plot creates a solid surface (x,y,z variables cmap=colour
plot)
ax0.plot_surface(_x,_y,_z, cmap='Blues')

#plot the x, y, z vectors
l=self.cb['radius']*2.0

#origin of arrow plot
x,y,z = [[0,0,0],[0,0,0],[0,0,0]]

#finish of arrow plot
u,v,w = [[50,0,0],[0,50,0],[0,0,50]]

#quiver is the arrow function with the above arguements and
k=colour
ax0.quiver(x,y,z,u,v,w,color='k')

#this helps normalise the axis and displays equal magnitudes i.e
cubic looking
max_val=np.max(np.abs(self.rs))

#set labels and titles
ax0.set_xlim([-max_val,max_val])
ax0.set_ylim([-max_val,max_val])
ax0.set_zlim([-max_val,max_val])
ax0.set_xlabel('X (km)')
ax0.set_ylabel('Y (km)')
ax0.set_zlabel('Z (km)')

#Title
ax0.set_title('EP Manoeuvre Trajectory')

if show_plot:
    plt.show()
if save_plot:
    plt.savefig(title+'.png',dpi=500)

```

Appendix 5 - Tools

#Gary Stewart
#Tool functions

```

#add in packages
import math as m
import datetime
import numpy as np
import matplotlib.pyplot as plt
from mpl_toolkits.mplot3d import Axes3D

#user defined
import Planetary_data_file as pd

#radians/degree conversion
d2r = np.pi/180.0
r2d = 180.0/np.pi

#normalised velocity and unit velocity vector
def norm(v):
    return np.linalg.norm(v)

def normed(v):
    return np.array(v)/norm(v)

#COES2RV algorithm at Rene-Schwarz m003
def coes2rv(coes,deg=True,mu=pd.earth['mu']):

    #if imput is in degrees
    if deg:
        a,e,i,ta,aop,raan,date=coes
        i*=d2r
        ta*=d2r
        aop*=d2r
        raan*=d2r

    #if input is radians
    else:
        a,e,i,ta,aop,raan,date = coes

    E=ecc_anomaly([ta,e], 'tae')
    r_norm=a*(1-e**2)/(1+e*np.cos(ta))

    #calculate r and v vectors in perifocal frame
    r_perif = r_norm*np.array([m.cos(ta),m.sin(ta),0])
    v_perif=m.sqrt(mu*a)/r_norm*np.array([-m.sin(E),m.cos(E)*m.sqrt(1-e**2),0])

    #rotation matrix from the perifocal to ECI
    perif2eci = np.transpose(eci2perif(raan,aop,i))

    #calculate r and v vectors in inertial frame
    r = np.dot(perif2eci,r_perif)
    v = np.dot(perif2eci,v_perif)

    return r,v,date

#RV2COES Algorithm at Rene-Schwarz m002
def rv2coes(r,v,mu=pd.earth['mu'],degrees=False,print_results=False):

    #norm of position vector

```

```

r_norm=norm(r)

#specific angular momentum vector
h=np.cross(r,v)
h_norm=norm(h)

#inclination
i=m.acos(h[2]/h_norm)

#eccentricity vector
e=((norm(v)**2-mu/r_norm)*r-np.dot(r,v)*v)/mu

#eccentricity scalar
e_norm=norm(e)

#node-line
N=np.cross([0,0,1],h)
N_norm=norm(N)

#RAAN
raan=m.acos(N[0]/N_norm)
if N[1]<0: raan=2*np.pi-raan #quad check

#argument of perigee
aop=m.acos(np.dot(N,e)/N_norm/e_norm)
if e[2]<0: aop=2*np.pi-aop #another quad check

#true anomaly
ta=m.acos(np.dot(e,r)/e_norm/r_norm)
if np.dot(r,v)<0: ta=2*np.pi-ta #another quad check

#semi-major axis
a=r_norm*(1+e_norm*m.cos(ta))/(1-e_norm**2)

if print_results:
    print('a',a)
    print('e',e_norm)
    print('i',i*r2d)
    print('RAAN',raan*r2d)
    print('AOP',aop*r2d)
    print('TA',ta*r2d)

#convert to degrees if it has been specified
if degrees: return [a,e_norm,i*r2d,ta*r2d,aop*r2d,raan*r2d]
else: return [a,e_norm,i,ta,aop,raan]

def eci2perif(raan,aop,i):

    row0 =[-m.sin(raan)*m.cos(i)*m.sin(aop)+ m.cos(raan)*m.cos(aop),
    m.cos(raan)*m.cos(i)*m.sin(aop)+ m.sin(raan)*m.cos(aop),
    m.sin(i)*m.sin(aop)]
    row1 =[-m.sin(raan)*m.cos(i)*m.cos(aop)- m.cos(raan)*m.sin(aop),
    m.cos(raan)*m.cos(i)*m.cos(aop)- m.sin(raan)*m.sin(aop),
    m.sin(i)*m.cos(aop)]
    row2 =[m.sin(raan)*m.sin(i), -m.cos(raan)*m.sin(i), m.cos(i)]

    return np.array([row0,row1,row2])
def ecc_anomaly(arr,method,tol=1e-8):
    if method=='newton':
        #newtons method for iteratively finding E

```

```

Me,e=arr
if Me<np.pi/2.0: E0=Me+e/2.0
else: E0 = Me- e
for n in range(200):
    ratio=(E0-e*np.sin(E0)-Me)/(1-e*np.cos(E0));
    if abs(ratio)<tol:
        if n==0: return E0
        else: return E1
    else:
        E1=E0-ratio
        E0=E1

    #failure to converge
    return False
elif method == 'tae':
    ta,e=arr
    return 2*m.atan(m.sqrt((1-e)/(1+e))*m.tan(ta/2.0))
else:
    print('Invalid method for eccentric anomaly')

#used to convert two line elements to orbital elements
def tle2coes(tle_filename,mu=pd.earth['mu'],deg=True,print_results=False):

    #read the tle text file from celetrak
    with open(tle_filename, 'r') as f:
        lines=f.readlines()

    #break the text file into three seperate lines
    line0 = lines[0].strip() #satellite name
    line1 = lines[1].strip().split
    line2 = lines[2].strip().split

    #epoch (year and day)
    epoch=line1()[3]
    year,month,day,hour=calc_epoch(epoch)

    #gather COE's from .txt

    #inclination
    i=float(line2()[2])*d2r #in radians

    #RAAN
    raan=float(line2()[3])*d2r #in radians

    #eccentricity
    e_string=line2()[4]
    e=float('0.'+e_string)

    #arguement of perigee
    aop=float(line2()[5])*d2r #in radians

    #mean_anomaly
    Me=float(line2()[6])*d2r #in radians

    #mean motion
    mean_motion=float(line2()[7]) #in revolutions per day

    #period
    T=1/mean_motion*24*3600 #in units of seconds

    #semi-major axis

```

```

a=(T**2*mu/4.0/np.pi**2)**(1/3.0)

#calculate eccentric anomaly
E=ecc_anomaly([Me,e], 'newton')

#calculate true anomaly
ta=true_anomaly([E,e])

#magnitude of radius vector
r_mag=a*(1-e*np.cos(E)) #####potential issue

return a,e,i,ta,aop,raan,[year,month,day,hour]

def calc_epoch(epoch):

    #epoch year
    year=int('20'+epoch[:2])

    epoch=epoch[2:].split('.')

    #day of year
    day_of_year=int(epoch[0])-1

    #decimal hour of day
    hour=float('0.'+epoch[1])*24

    #year/month/day
    date=datetime.date(year,1,1)+datetime.timedelta(day_of_year)

    #extract month and day from tle
    month=float(date.month)
    day=float(date.day)

    return year,month,day,hour

def true_anomaly(arr):
    E,e=arr
    return 2*np.arctan(np.sqrt((1+e)/(1-e))*np.tan(E/2.0))

def tle2rv(tle_filename):
    return coes2rv(tle2coes(tle_filename))

#calculate atmospheric density from given altitude
def calc_atmospheric_density(z):
    rhos,zs=find_rho_z(z)
    if rhos[0]==0: return 0.0

    Hi=-(zs[1]-zs[0])/np.log(rhos[1]/rhos[0])
    return rhos[0]*np.exp(-(z-zs[0])/Hi)

#find endpoints of altitude and density surrounding input altitude
def find_rho_z(z,zs=pd.earth['zs'],rhos=pd.earth['rhos']):
    if not 1.0<z<1000.0:
        return [[0.0,0.0],[0.0,0.0]]

    #find the two points surrounding the given input
    for n in range(len(rhos)-1):
        if zs[n]<z<zs[n+1]:
            return[[rhos[n],rhos[n+1]],[zs[n],zs[n+1]]]
    #if out of range return zeros
    return [[0.0,0.0],[0.0,0.0]]

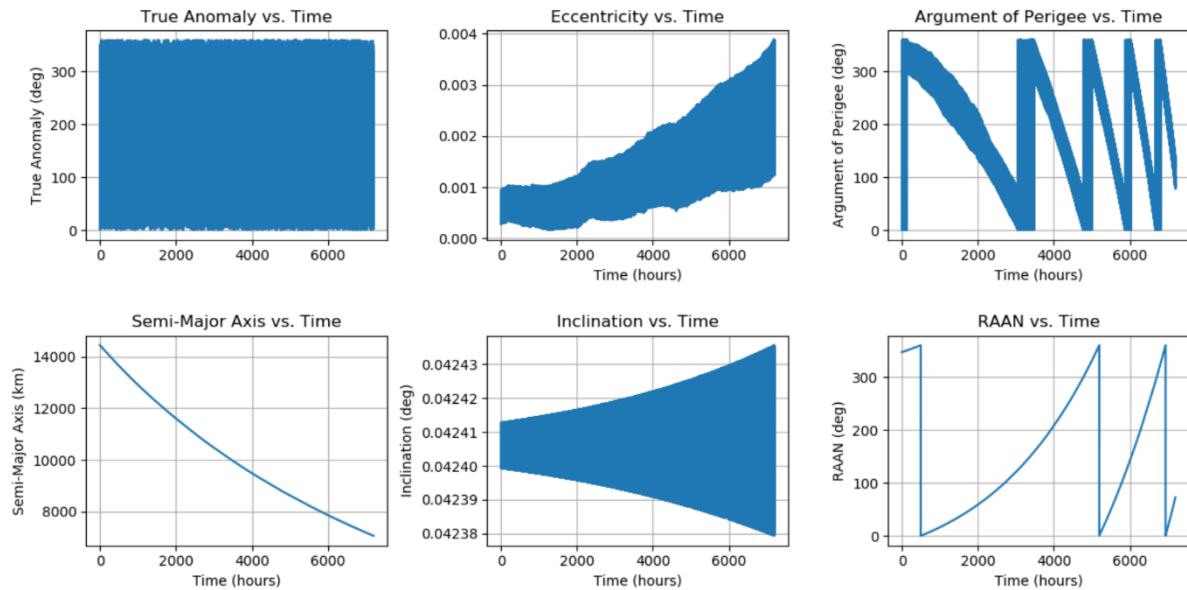
```

Appendix 6 – ‘SAT-1’ Satellite Details

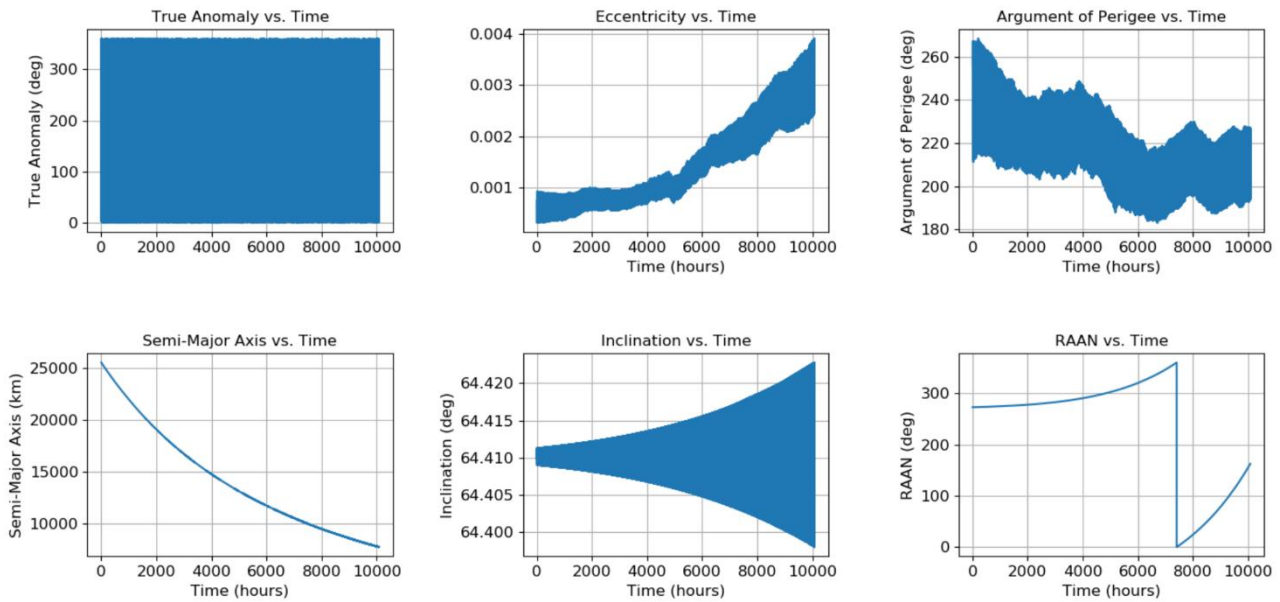
Devised Satellite Details			
Satellite Name	Dry Mass (kg)	Satellite Cross-section (m ²)	Coefficient of Drag
Sat-1	2000	5.60E-06	2.2

Appendix 7 - Auxiliary Orbital Element Plots

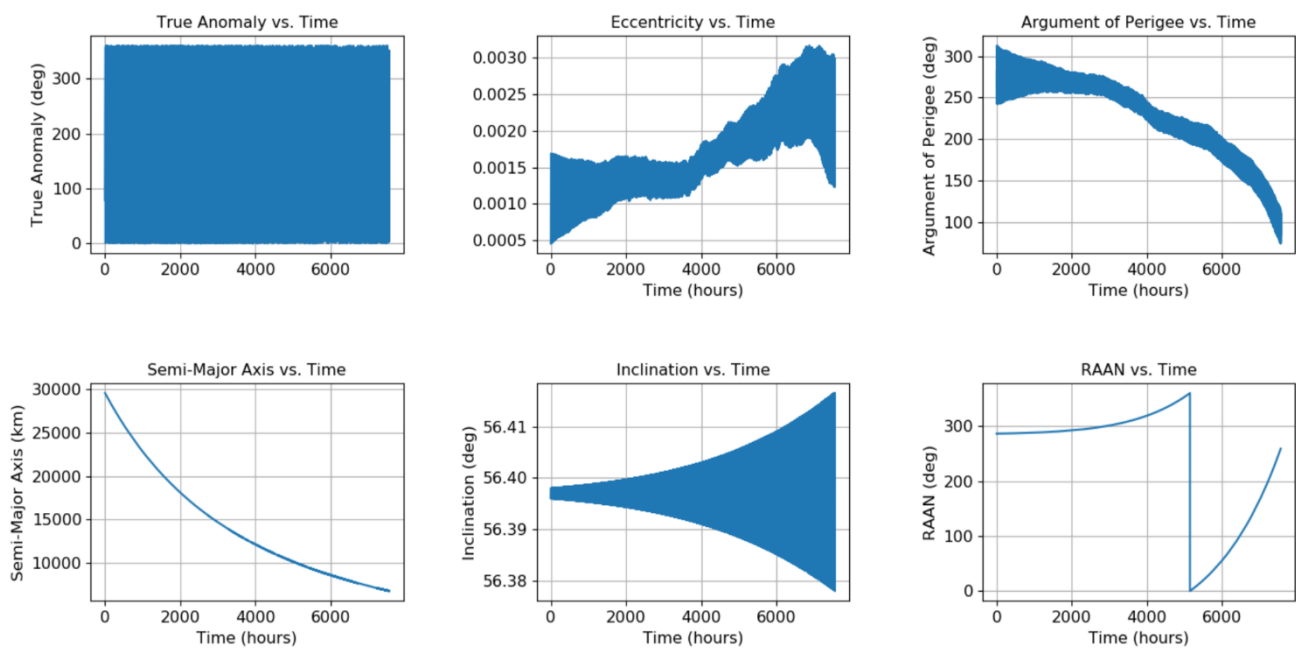
Change in COES at 7825km with XIPS-25



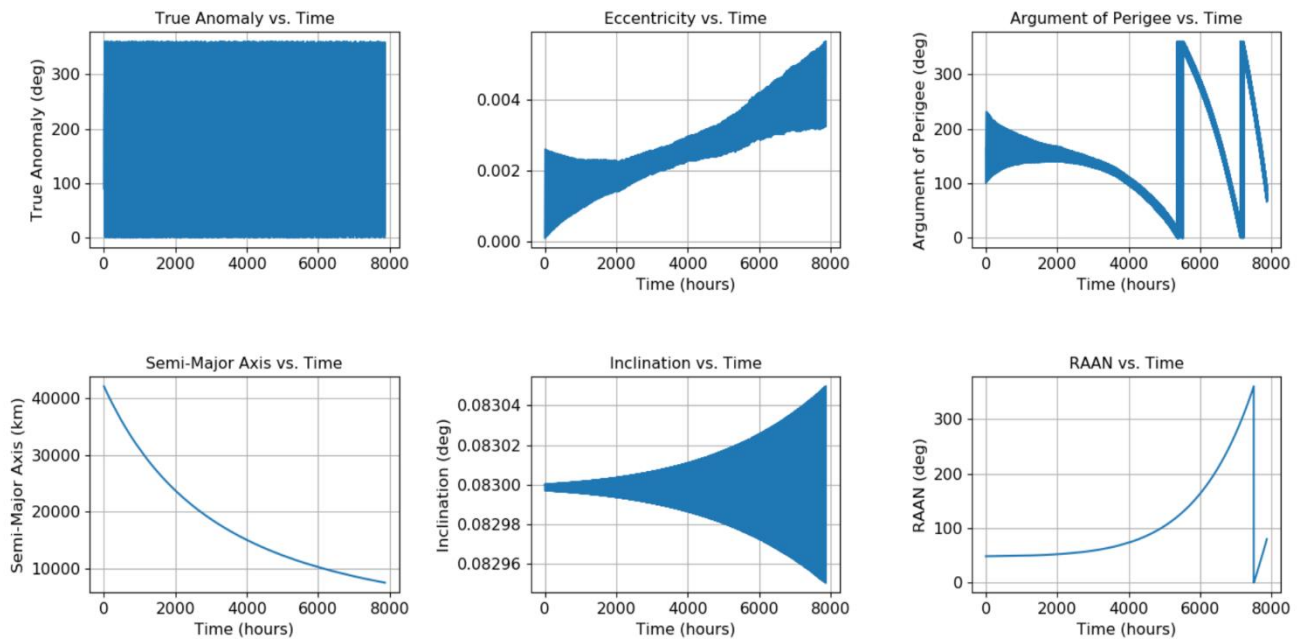
Change In COES at 19100km with XIPS-25



Change In COEs at 23222km with BPT4000



Change In COEs at 35786km with BPT4000



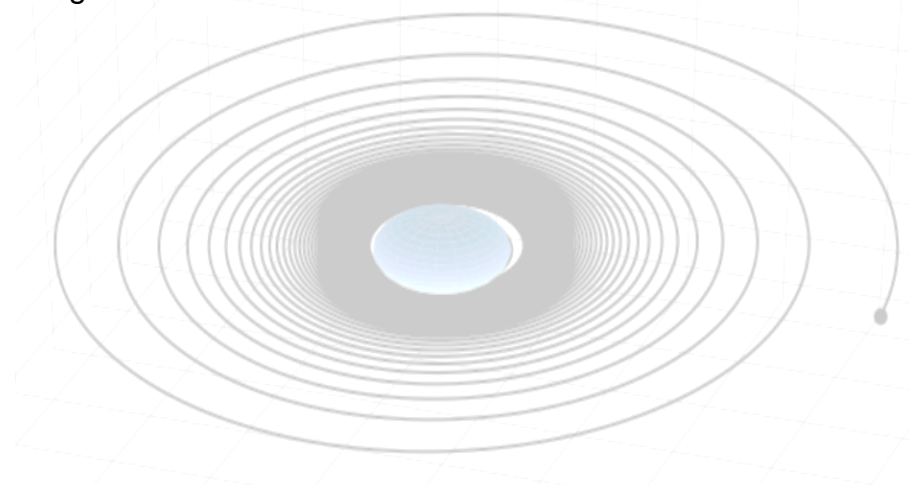
Appendix 8 – Attached Technical Paper

Class Code/ Title: ME409: Individual Project
Technical paper title: An investigation of the feasibility of using electric propulsion as a means of deorbiting end of life satellites in middle and geostationary orbits (MEO) (GEO).

Student Name/ Number: 201607942
Supervisor: Dr S. Grey
Date: 25/03/2020
Word count: 2998

Abstract

This work investigated the use of electric propulsion as a space-debris mitigation technique for higher altitude satellites. The proposed solutions had to adhere to current industry regulations while reducing the risk of further collisions in orbit. A numerical model of a two-body orbit was devised in Python 3.7 to simulate the thrust, J2-effect and aerodynamic-drag acting on the spacecraft, several qualified thrusters were simulated across a series of orbital altitudes. Thrusters were evaluated in terms of power, mass, cost and manoeuvre times. The results indicated two candidates that could manoeuvre a 2000kg satellite from GEO to a deorbit altitude of 200km; one offered shorter manoeuvre times with reduced power requirements, however, the other offered a significant reduction in propellant mass at the expense of higher power. Utilising electric propulsion over chemical propulsion yielded an average 94.2% propellant saving which translated to an estimated \$30-65M USD saving from launch.



Contents

Nomenclature.....	iii
1.0 Introduction	1
1.1 Scope.....	1
2.0 Literature Review	1
2.1 Propulsion in Space.....	1
2.2 Post Mission Disposal Manoeuvre (PMD).....	4
3.0 Method	5
3.1 Deriving the System: Two body Mechanics	5
3.1.1 Newton's Law of Gravitation.....	5
3.1.2 Implementation of numerical integrator	6
3.1.3 State Vector to Classical Orbital Elements (COES)	6
3.2 Implementation of orbital perturbations.....	7
3.2.1 J2 Effect	7
3.2.2 Aerodynamic Drag.....	8
3.2.3 Thrusting	10
3.3 Mission Parameters	10
3.3.1 Thruster Selection	10
3.3.2 Orbit Selection.....	11
3.3.3 Stop Conditions	11
4.0 Results	11
4.1 Simulation Outputs	12
4.2 Model Validation	17
5.0 Discussion.....	18
5.1 Model Limitations	18
5.2 Thruster Evaluation.....	18
5.3 Power Source	19
5.4 Cost Benefit Analysis.....	20
6.0 Conclusions	21
7.0 References.....	22
8.0 Appendices	26
8.1 Source-code Hyperlink.....	26
8.2 Satellite Details	26
8.3 Auxiliary Orbital Element plots	26

Nomenclature

<u>Symbol</u>	<u>Description</u>	<u>Units</u>
A	Satellite area	m^2
ATM	Atmospheric direction vector	ms^{-1}
a_{j2}	J2 component of acceleration	ms^{-2}
a_{thrust}	Acceleration component due to thruster	ms^{-2}
C_d	Coefficient of drag	-
e	Orbital eccentricity	-
E_m	Energy required for manoeuvre	GJ
F_t	Total Thrust Force	N
g_0	Gravitational Constant for earth	ms^{-2}
h	Angular momentum vector	m^2s^{-1}
H_i	Scale height	m
i	Orbital Inclination	rad
I_{sp}	Specific Impulse	Sec
M	Mean molecular molar mass	kg.mol^{-1}
m_1	Mass of earth	kg
m_2	Mass of satellite	Kg
m_{prop}	Mass of propellant required for manoeuvre	kg
m_{ppu}	Mass of required power conditioning units	kg
n	Nodal line	m
N	Ratio of initial & final radii	-
R	Gas Constant	-
\vec{r}_1	Radial vector of earth	m
\vec{r}_2	Radial vector, earth to satellite	m
T	Mean atmospheric temperature	K
t_m	Time taken to deorbit	seconds
V	Magnitude of satellite velocity	ms^{-1}
v_{normed}	Velocity unit vector	-
$v_{\text{sc}}_{\text{atm}}$	Spacecraft velocity relative to atmosphere	ms^{-1}
z	Altitude	m
V	Magnitude of satellite velocity	ms^{-1}
α	Semi-major axis	m
Δv	Change in Velocity	ms^{-1}
ΔV_H	Hohmann Transfer – change in velocity	ms^{-1}
ΔV	Perturbation Theory – change in velocity for EP	ms^{-1}
μ	Standard gravitational parameter	m^3s^{-2}
ν	True anomaly	rad
ρ	Air density	kgm^{-3}
ρ_{SL}	Air density at sea-level	kgm^{-3}
$\rho(z)$	Air density as a function of altitude	kgm^{-3}
Ω	Rising ascending node	m
ω	Argument of periapsis	rad

1.0 Introduction

1.1 Scope

The aim of this work was to investigate the feasibility of using electric propulsion (EP) for deorbiting end of life satellites. Several thrusters were simulated across multiple altitudes to investigate the suitability of the thrusters in terms of power, mass, cost and manoeuvre times. Four thrusters were selected, and system architecture was discussed alongside a cost-comparison of chemical propulsion (CP) thrusters to assess the cost benefit of the transition.

It has become evident that space-debris is a serious issue facing the space-industry - if not suitably addressed, current models indicate there is a significant risk of setting off a chain reaction known as the Kessler Syndrome [1]. The reaction would cause an exponential increase in the creation of new debris through a higher object collision rate, which would elevate the risk above a safe level for space-operations. This study investigated EP as a new space-debris mitigation strategy which would, when implemented, reduce the risk of further collisions. Furthermore, it was imperative that solutions adhered to ESA /NASA spaceflight guidelines specified below [2] [3].

1. *“The final orbit shall grant a decay time of less than 25 years...”*
2. *“The final orbit must pose no risk to human space flights...”*
3. *“The final orbit shall allow the debris to leave the region within 1 year.”*

2.0 Literature Review

2.1 Propulsion in Space

In space, there are two methods of producing thrust. The first and most commonly employed method is CP, which produces thrust through a combustion process, occurring typically in a high-pressure reaction chamber where hot gas is accelerated through a nozzle to provide thrust [4].

Conversely, EP is a hypernym for a range of systems that exploit the interaction between an electromagnetic field and charged particles. The interaction is facilitated by the ionisation and acceleration of propellant gas to produce thrust. Although EP systems tend to operate on the same underlying principle, they can be categorised into three groups by how they accelerate particles: Electrothermal, Electrostatic and Electromagnetic [5].

Analysis of the physical phenomena defined above had limited value to the technical study and is out-with the scope of this report. However, an in-depth explanation of their physical characteristics can be found in the literature [5] [6].

The advantages of EP were deduced from table-1 and equation-1, specific impulse I_{sp} was calculated by dividing thrust-force F_t , by a rocket's mass-flow rate \dot{m} , multiplied by the gravitational constant g_0 . Hence, I_{sp} can be defined as the power to thrust ratio of a propulsion system. EP systems' higher I_{sp} ranges yield improvements to payload-mass fractions, due to lower \dot{m} but operate at lower F_t ranges [6].

$$I_{sp} = \frac{F_{thrust}}{\dot{m}g_0} \quad Eqn. 2$$

Table 1 – CP and EP thruster performance ranges [5].

Thruster Type	Specific Impulse (sec)	Thrust Range (mN)	Input Power (kW)	Efficiency (%)	Typical Propellant Utilisation
Cold Gas	50-75	500-60000	-	-	Various
Chemical (monopropellant)	150-225	30-80000	-	-	N_2H_4 H_2O_2
Chemical (Bipropellant)	300-450	30-100000	-	-	Various
Resistojet	300-325	200-300	0.5-1.1	65-90	N_2H_4
Arcjet	500-600	200-1000	0.9-2.2	25-45	N_2H_4
Ion Thruster	1500-4900	0.01-500	0.4-4.3	40-80	Xenon
Hall Thruster	900-2600	0.01-2000	1.5-4.5	35-60	Xenon
PPT's	850-1200	0.05-10	<0.2	7.5-13	Teflon

Table-1 shows that EP is power-intensive compared to CP. The limitations of power generation in space are often the deciding factor in selecting propulsion systems [7]. However, the combined effect of improved solar-arrays, advanced lithium-ion batteries, and sophisticated power-conditioning units led to an increase in spacecraft power-capacity [8]. It was key to identify a nominal power input range to scope thrusters, to compensate for efficiencies and degradation of power systems across a mission life of 10-15 years. After which, designers must assess the spacecraft's power integrity, in order to provide constant power to the thrusters throughout its final manoeuvre. Figure-1 identifies EP systems' regions of mission utility for various thrusters.

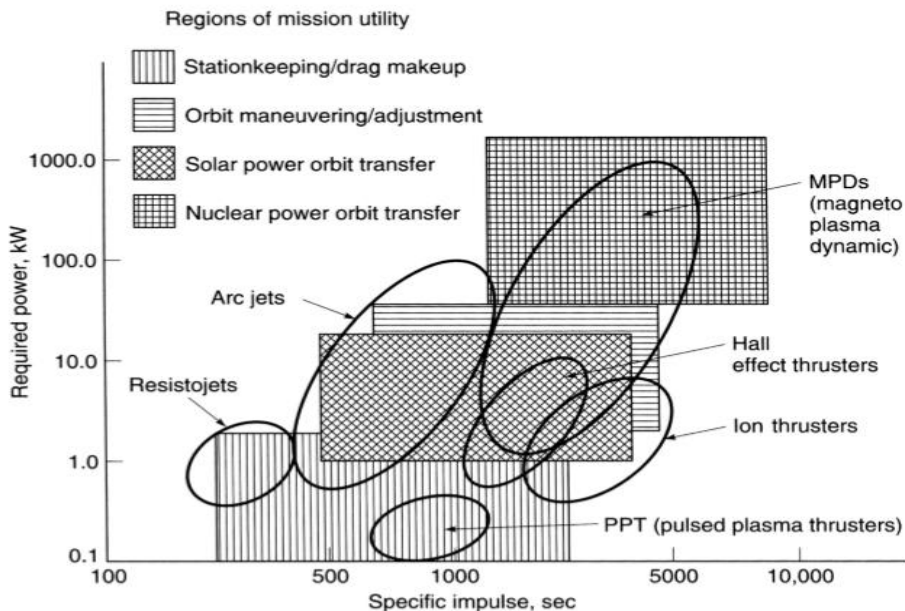


Figure 1 - Regions of mission utility for EP systems [7].

Ion and Hall-effect thrusters (HET) were selected due to their relatively low power range P_{in} , of 0.5-10kW and large I_{sp} , ranges of 1000-5000. Moreover, this assertion was supported by a host of successful missions such as; GOCE, SMART-1, Hayabusa, Deepspace-1 and Dawn [9] [10] [11].

2.2 Post Mission Disposal Manoeuvre (PMD)

The strategy for PMD with CP systems would be modelled on a reversed Hohmann transfer. The method detailed in figure-2 entails scheduled retrograde burns to decrease the apogee velocity until the final circularised orbit has been reached [12]. The final position tends to be within very low earth orbits to allow the atmospheric drag to rapidly decelerate and heat the craft to burn up prior to re-entry.

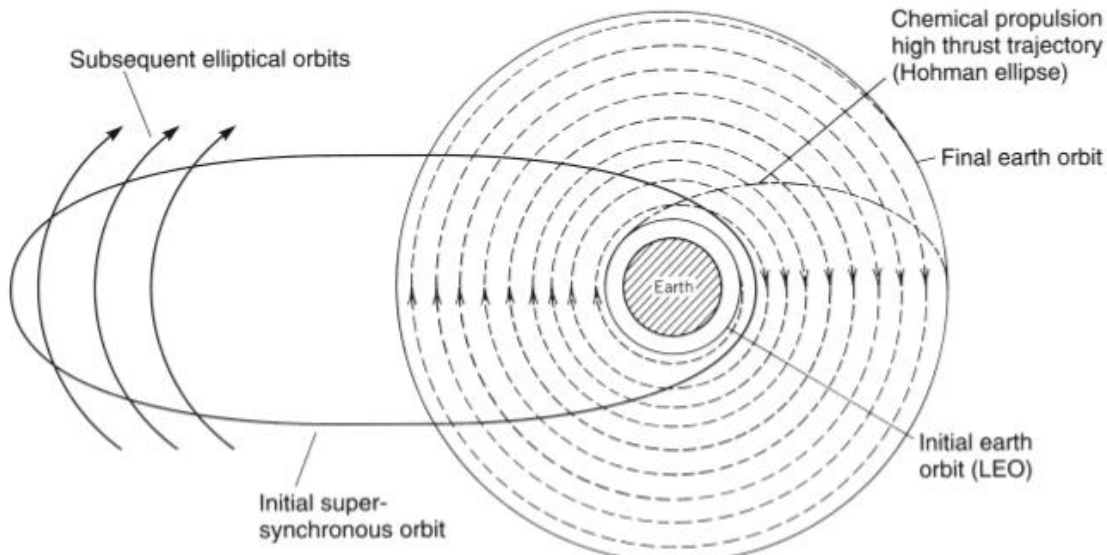


Figure 2 - Proposed CP & EP manoeuvre trajectories detailing a Hohmann transfer and a gradual spiral towards target orbit. [7].

Figure-2 details the desired trajectory for an EP PMD mission, the spiral descent [7] [13]. Unlike Hohmann transfers, spiral manoeuvres are constant thrust and non-Keplerian and are only solvable through numerical integration where time becomes a key parameter. It was noted that the ΔV , for a spiral manoeuvre would be greater than the equivalent Hohmann transfer, but it was considered useful to compare each.

3.0 Method

The below programme was built using Python 3.7 with NumPy, SciPy and Matplotlib [14] [15]. The source code is available in appendix^{7.1} and [GitHub](#). The methodology outlined below details the underlying mathematics used to construct the model.

3.1 Deriving the System: Two body Mechanics

Section 3.1 details key components of building a steady state two-body mechanics problem.

3.1.1 Newton's Law of Gravitation

It was pertinent to the body of work to first understand the underlying physics of two-body orbit problems between a spacecraft and earth. Both objects were treated as point-masses, and in the absence of external forces, the equation of motion for the masses were stated as equation-2-3 [16].

$$m_1 \frac{d^2 \vec{r}_1}{dt^2} = G m_1 m_2 \frac{\vec{r}_2 - \vec{r}_1}{|\vec{r}_2 - \vec{r}_1|^3} \quad Eqn. 2$$

$$m_2 \frac{d^2 \vec{r}_2}{dt^2} = -G m_1 m_2 \frac{\vec{r}_2 - \vec{r}_1}{|\vec{r}_2 - \vec{r}_1|^3} \quad Eqn. 3$$

The position vector was defined as $\vec{r}_2 - \vec{r}_1 = \vec{r}$, and hence equation-3 was subtracted from equation-2 and yielded a single equation of motion below, equation-4.

$$\frac{d\vec{v}}{dt} + \mu \frac{\vec{r}}{r^3} = 0 \quad Eqn. 4$$

Where $v = \frac{dr}{dt}$ and $\mu = G(m_1 + m_2)$. The mass of the satellite m_1 is negligible with respect to the mass of the earth m_2 , therefore $\mu = Gm_1$. Newton's law-of-gravitation was directly integrated, yielding an acceleration vector $a = [a_x, a_y, a_z]$. Equation-4 was defined in the function ODE within the orbit_propagator_script. [17]

3.1.2 Implementation of numerical integrator

The integrator LSODA was selected from the SciPy package to numerically evaluate equation-4. LSODA utilised the Adam-Basford multistep method, which produced highly accurate results and reduced computational cost when compared to lower order schemes [18].

3.1.3 State Vector to Classical Orbital Elements (COES)

The programme required a conversion algorithm with an input of cartesian state-vectors to COES, to accurately define the manoeuvre in all six degrees of freedom [19] [20]. COES were defined as inclination, eccentricity, rising-ascending node, argument of periapsis, true anomaly and semi-major axis.

The angular momentum vector denoted h was required for calculating inclination, eccentricity and node-line, it was computed by taking the cross product of position and velocity vectors in equation-5. The orbital inclination i , was calculated in equation-6 by dividing h_z by the magnitude of the angular momentum vector.

$$h = r \times \dot{r} \quad \left[\frac{m^2}{s} \right] \quad Eqn. 5$$

$$i = \arccos \frac{h_z}{\|h\|} \quad Eqn. 6$$

Next, the eccentricity vector was calculated from equation-7 where $\mu = \mu_{earth} = 6.67408E-11$. Now, as per equation-8 the node-line was computed.

$$e = \frac{h \times \dot{r}}{\mu} - \frac{r}{\|r\|} \quad Eqn. 7$$

$$n = (0 \quad 0 \quad 1)^T \times h = (-h_y \quad h_x \quad 0)^T \quad Eqn. 8$$

The longitude of the rising ascending node Ω , was calculated using equation-9 with applied conditional statements, regarding the input of the node-line vector.

$$if; n_y \geq 0, \quad \Omega = \arccos \frac{n_z}{\|n\|} \quad Eqn. 9$$

$$\text{else; } n_y < 0, \quad \Omega = 2\pi - \arccos \frac{n_z}{\|n\|}$$

Similarly, in equation-10, conditional statements are imposed on the input of eccentricity to calculate the argument of periapsis.

$$\text{if; } e_z \geq 0, \quad \omega = \arccos \frac{\langle n, e \rangle}{\|n\|\|e\|} \quad \text{Eqn. 10}$$

$$\text{else; } e_z < 0, \quad \omega = 2\pi - \arccos \frac{\langle n, e \rangle}{\|n\|\|e\|}$$

The required eccentricity is derived from the normalised magnitude of the eccentricity vector, and henceforth, mathematically $e = \|e\|$.

Normalised eccentricity was used to calculate true anomaly ν .

$$\text{if; } r, \dot{r} \geq 0, \quad \nu = \arccos \frac{\langle e, r \rangle}{\|e\|\|r\|} \quad \text{Eqn. 11}$$

$$\text{else; } \nu = 2\pi - \arccos \frac{\langle e, r \rangle}{\|e\|\|r\|}$$

Finally, the semi-major axis, α was calculated as per equation-12.

$$\alpha = \frac{1}{\frac{2}{\|r\|} - \frac{\| \dot{r} \|^2}{\mu}} \quad \text{Eqn. 12}$$

3.2 Implementation of Orbital Perturbations

Perturbations considered were subsequently defined in sections 3.2.1, 3.2.2 and 3.3.3 – their characteristics were specified within the function; `null_perts()` which returned a dictionary. This allowed the use of Boolean-logic to turn perturbations on and off while building and testing the model.

3.2.1 J2 Effect

The J2-effect [21], or earth's oblateness, is the strongest perturbation of all the non-spherical J-terms, therefore it was practical to consider its effects. The J2-effect was introduced into the model by the addition of the a_{J2} , into equation-13, and was rearranged for acceleration in equation-14, Newton's law-of-gravitation.

$$\frac{d\vec{v}}{dt} + \mu \frac{\vec{r}}{r^3} + a_{J2} = 0 \quad Eqn. 13$$

$$\therefore a_{xyz} = \mu \frac{\vec{r}}{r^3} + a_{J2} \quad Eqn. 14$$

a_{J2} was calculated with perturbation theory by partially differentiating v_{J2} with respect to the spatial directions to generate expressions for acceleration in equation-15 [22].

$$\begin{aligned} a_x &= -\frac{\mu \vec{x}}{r^3} \left\{ 1 + \frac{3}{2} J_2 \left(\frac{r}{r} \right)^2 \left(1 - \frac{5z^2}{r^2} \right) \right\} \\ a_y &= -\frac{\mu \vec{y}}{r^3} \left\{ 1 + \frac{3}{2} J_2 \left(\frac{r}{r} \right)^2 \left(1 - \frac{5z^2}{r^2} \right) \right\} \quad Eqn. 15 \\ a_z &= -\frac{\mu \vec{z}}{r^3} \left\{ 1 + \frac{3}{2} J_2 \left(\frac{r}{r} \right)^2 \left(3 - \frac{5z^2}{r^2} \right) \right\} \end{aligned}$$

The components of equation-15 were passed as an array into equation-14 and were simply added to the acceleration vector.

3.2.2 Aerodynamic Drag

Aerodynamic drag is considered to have a substantial effect in satellites within lower earth orbit. Equation-16 magnitude is dependent on a craft's effective area A, velocity magnitude V, variable density value of ρ and a coefficient of drag C_d - which was assumed to be 2.2 [23] [24].

$$F_d = -C_d \cdot A \cdot \rho \cdot \frac{V^2}{2} \quad Eqn. 16$$

The U.S. Standard Atmosphere model 1976 [25] was applied to model variations in atmospheric density at approximately; 60.096km, 251.189km and 1000km, the vector quantity was stored within the `planetary_data_file`. The first step of the algorithm, equation-17, was to calculate altitude:

$$z = |\vec{r}_2| - |\vec{r}_1| \quad Eqn. 17$$

The algorithm required computation of air density at satellites current altitude. It was assumed that the effects of the atmosphere were negligible above 1000km and hence $\rho = 0$. Therefore, density as a function of altitude can be calculated as equation-18 [26]:

$$\rho(z) = \rho_{SL} \cdot e^{-\frac{z}{H_i}} \quad Eqn. 18$$

Where ρ_{SL} was defined as air density at sea level and H_i was defined as altitude increment where the density decreases by a factor of $e^{-1} \approx 0.4$ which can be derived from gas-law relation observed in equation-19;

$$H_i = \frac{RT}{Mg} \quad Eqn. 19$$

Moreover, the atmosphere is not fixed within the earth centred inertial frame and instead rotates with the earth. Equation-20 was used to calculate the motion of the spacecraft relative to the atmosphere by using spacecraft velocity in the earth centred inertial frame and subtracting the cross-product of the atmospheric velocity vector $|ATM|$, and the spacecraft's position vector.

$$V_{sc/atm} = V - |ATM| \cdot |R| \quad Eqn. 20$$

The atmosphere vector was calculated as per equation-21 by taking one full revolution of earth and dividing it by the hours in one day [27].

$$|ATM| = \frac{2\pi}{86160 \text{ (23 hours 56 minute)}} = |ATM| \hat{z} \quad Eqn. 21$$

The above values were substituted into equation-22 and divided by the satellite mass and added to the acceleration vector.

$$a_d = - \frac{C_d \cdot A \cdot \rho(z) V_{sc/atm}}{m_{sat}} \quad Eqn. 22$$

3.2.3 Thrust

Acceleration provided by EP modules could be calculated using Newton's 2nd law:

$$F_{thrust} = m_{sat} \cdot a_{thrust} \quad Eqn. 23$$

The thrust vector was given direction by taking the velocity vector V and dividing it by the normalised vector quantity, yielding the unit vector [26]. The parameter was assigned a thrust direction integer of -1 to indicate that the thrust vector must act against the velocity vector, and act as a deorbit manoeuvre.

$$v_{normed} = \frac{[v]}{|v|} \quad Eqn. 24$$

Equation-23 and equation-24 were multiplied together and rearranged to yield equation-25:

$$a_{thrust} = -\left(\frac{[v]}{|v|}\right) \frac{F_{thrust}}{m_{sat}} \quad Eqn. 25$$

All perturbations were then substituted into Newton's law-of-gravitation which gives the full equation of motion in equation-26.

$$a = \mu \frac{\vec{r}}{r^3} + a_{J2} + a_{drag} + a_{thrust} \quad Eq. 26$$

3.3 Mission Parameters

3.3.1 Thruster Selection

Table 2 - EP Specifications for thrusters simulated [7] [28].

Thruster	Power (W)	Impulse (sec)	Thrust (mN)	Efficiency (%)	Mass (kg)	Max-Burn (hr)
SPT100D	2500	2200	112	52	4.7	11680
XIPS-25	4250	3550	165	67	13.7	13370
PPS1350	1400	1660	90	55	5.3	9500
BPT 4000	4500	1950	270	59	7.5	8000

Table-2 shows the selected thruster systems, it comprises of both Ion & HET systems and represent a broad range of power, I_{sp} and thrust. Their selection was based on the proven operational history in spaceflight and their use is limited by their respective mass burn time.

3.3.2 Orbit Selection

Manoeuvres were simulated at altitudes of 7825km, 19100km, 23222km and 35786km using the devised 2000kg satellite ‘SAT-1’ – Appendix^{7.2} - to assess various thrusters. Two-line element files were extracted from CelestTrak-API [29] in order to generate accurate satellite input data.

3.3.3 Stop Conditions

The study assumed constant power and did not account for an eclipse period. Thus, continuous thrust was applied from the satellite’s initial position until 200km altitude was reached. The final altitude was considered sufficiently deorbited, due to the prominence of atmospheric-drag at that altitude [30]. With stop conditions defined, total change in velocity ΔV was calculated as equation-27:

$$\Delta V \approx \sqrt{\frac{\mu}{r_0}} - \sqrt{\frac{\mu}{r}} \quad Eqn. 27$$

The Hohmann transfer detailed in Section-2.2 was given as equation-28.

$$\Delta V_H = \left(\sqrt{\frac{2\mu r}{r_0(r+r_0)}} - \sqrt{\frac{\mu}{r_0}} \right) + \left(\sqrt{\frac{\mu}{r}} - \sqrt{\frac{2\mu r_0}{r(r+r_0)}} \right) \quad Eqn. 28$$

Hence, by assuming radii r and r_0 are related by $r = Nr_0$ where N is the number of revolutions, the ratio of divergence from Hohmann transfer was calculated as equation-29:

$$\frac{\Delta V}{\Delta V_H} = \left[\sqrt{2 \left(1 + \frac{2\sqrt{n}}{n+1} \right)} - 1 \right]^{-1} \quad Eqn. 29$$

4.0 Results

Section 4.1 details simulation results for deorbit manoeuvres across various altitudes with thrusters specified in section 3.3.1.

4.1 Simulation Outputs

Figure-3 shows manoeuvre times from 7825km with selected thrusters with additional data in table-3. BPT4000 produced the lowest manoeuvre-time (t_m) of 4319 hours. PPS1350 took 13045 hours, which disqualified its use, as t_m is out-with the thruster's maximum burn-time of 9500 hours. Disqualified thrusters have been highlighted red and suitable thrusters green in tables-3-6.

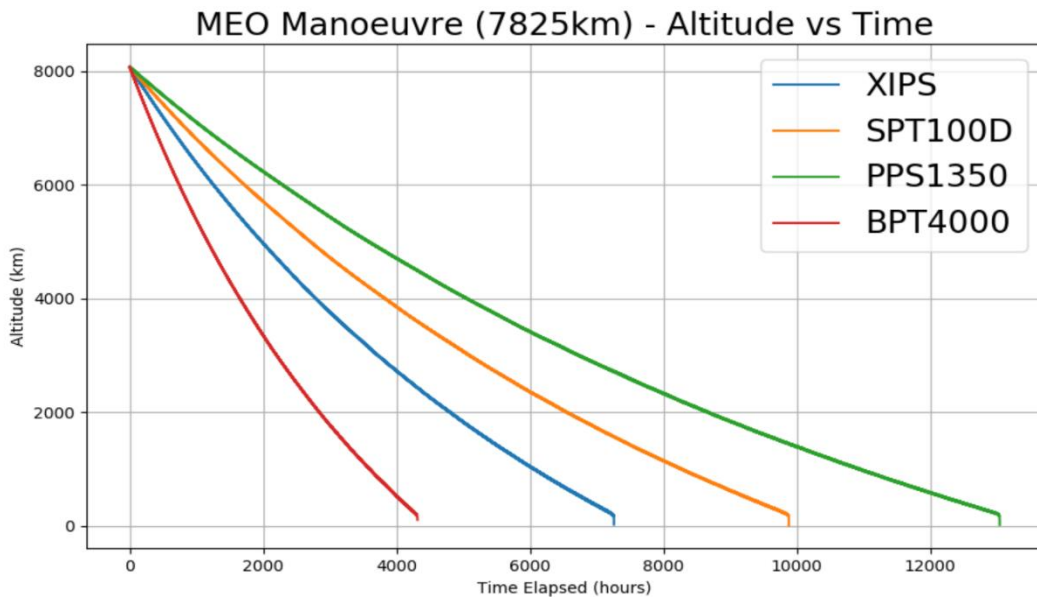


Figure 3 – Simulated manoeuvre from 7825km to 200km with EP systems

Figure-4 and table-4 show results from 19100km, SPT100D was disqualified from use, due to a t_m of 14975 hours with a maximum burn time of 11680 hours.

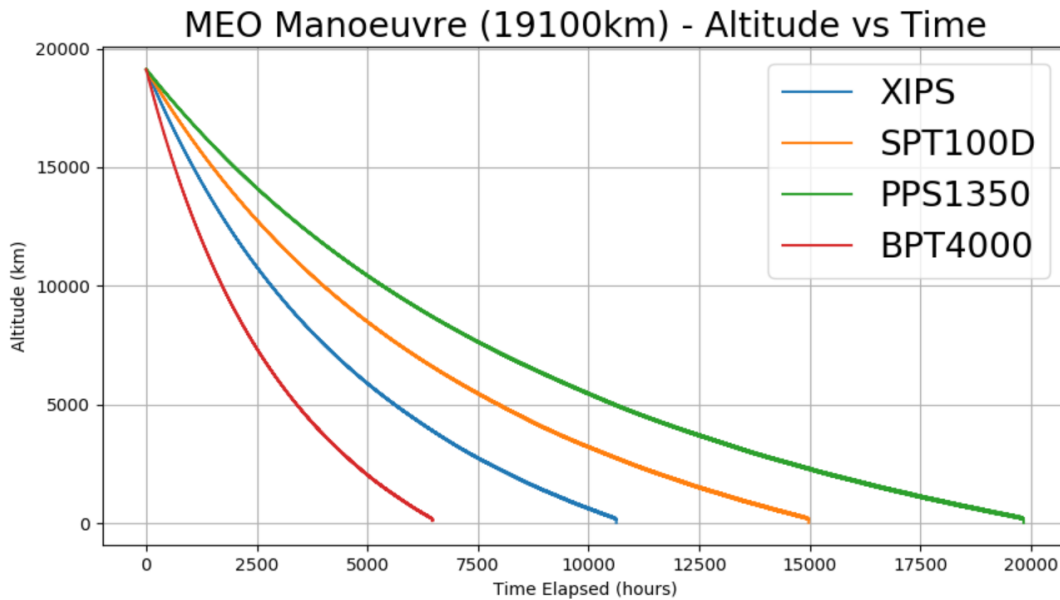


Figure 4 – Simulated Manoeuvre from 19100km to 200km with EP systems.

Table 3 - Results from PMD at 7825km with EP systems, where t_m denoted time, E_m denoted energy used and M denotes mass.

Manoeuvre from 7825km									
	t_m (second)	M_{prop} (kg)	M_{ppu} (kg)	t_m (hour)	t_m (days)	E_m (GJ)	M_{total} (kg)	$\frac{\Delta V}{\Delta V_H}$	Max Burn Time (Hour)
SPT100D	35581350	184.65	20.83	9883.71	411.82	89	2710.18	1.614	11680
XIPS	26140350	123.85	21.57	7261.21	302.55	111	2659.12	1.614	13370
PPS1350	46962750	259.55	14.14	13045.21	543.55	65.7	2778.99	1.614	9500
BPT 4000	15549750	213.99	24.19	4319.38	179.97	70	2745.68	1.614	8000

Table 4 – Results from PMD at 19100km with EP systems, where t_m denoted time, E_m denoted energy used and M denotes mass.

Manoeuvre from 19100km									
	t_m (second)	M_{prop} (kg)	M_{ppu} (kg)	t_m (hour)	t_m (days)	E_m (GJ)	M_{total} (kg)	$\frac{\Delta V}{\Delta V_H}$	Max Burn Time (Hour)
SPT100D	53911200	279.77	31.25	14975.33	623.97	135	2815.72	1.815	11680
XIPS	38260500	181.27	32.36	10627.92	442.83	163	2727.34	1.815	13370
PPS1350	71408700	394.65	21.21	19835.75	826.49	100	2921.17	1.815	9500
BPT 4000	23305050	320.71	36.29	6473.63	269.73	105	2864.50	1.815	8000

Figure-5 details the manoeuvre from 23222km, due to the weakened gravity field and the relatively small distance, similar results were recorded between 19100km and 23222km – see table-4-5.

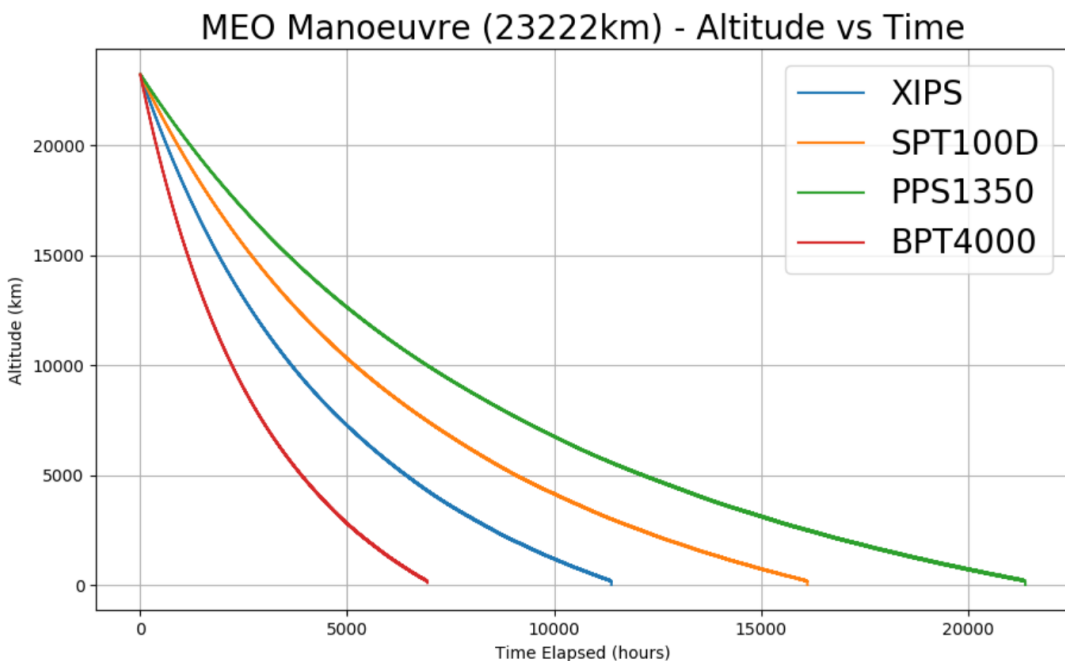


Figure 5 – Simulated manoeuvre from 23222km to 200km with EP systems.

Figure-6 highlights two appropriate thrusters for satellites in geostationary orbits. XIPS-25 and BPT4000 have a suitable range for a 2000kg satellite, XIPS-25 greater I_{sp} , yielded a 181kg propellant saving over BPT4000 but takes a further 4270 hours to complete the manoeuvre. Additional COES data for successful manoeuvres can be viewed in Appendix^{7.3}

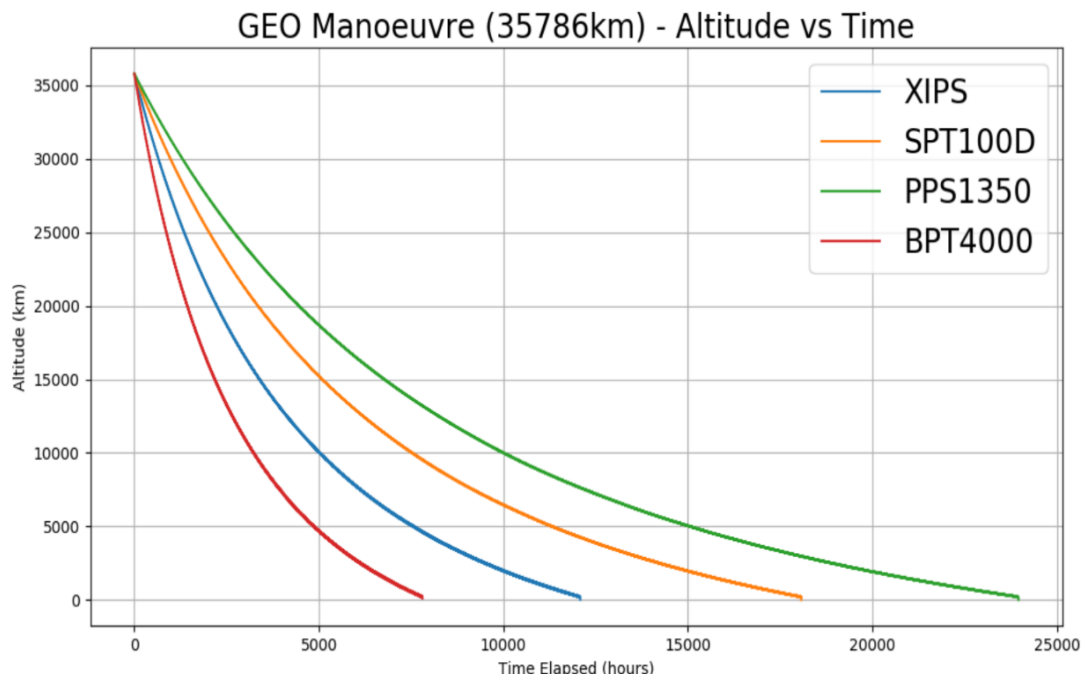


Figure 6 – Simulated manoeuvre from 35786km to 200km with EP systems.

Table 5 - Results from PMD at 23222km with EP systems, where t_m denoted time, E_m denoted energy used and M denotes mass.

Manoeuvre from 23222km									
	t_m (second)	M_{prop} (kg)	M_{ppu} (kg)	t_m (hour)	t_m (days)	E_m (GJ)	M_{total} (kg)	$\frac{\Delta V}{\Delta V_H}$	Max Burn (Hour)
SPT100D	58027800	301.14	41.67	16118.83	671.62	135	2847.50	1.856	11680
XIPS	40985400	194.19	43.15	11384.83	474.37	163	2751.03	1.856	13370
PPS1350	76990650	425.50	28.28	21386.29	891.10	100	2959.09	1.856	9500
BPT 4000	24946800	343.30	48.39	6929.67	288.74	105	2899.19	1.856	8000

Table 6 - Results from PMD at 35786km with EP systems, where t_m denoted time, E_m denoted energy used and M denotes mass.

Manoeuvre from 35786km									
	t_m (second)	M_{prop} (kg)	M_{ppu} (kg)	t_m (hour)	t_m (days)	E_m (GJ)	M_{total} (kg)	$\frac{\Delta V}{\Delta V_H}$	Max Burn (Hour)
SPT100D	65050650	337.58	52.08	18069.63	752.90	163	2894.36	1.94	11680
XIPS	43494300	206.07	53.93	12081.75	503.41	185	2773.71	1.94	13370
PPS1350	86241300	476.63	35.35	23955.92	998.16	121	3017.28	1.94	9500
BPT 4000	28122600	387.01	60.48	7811.83	325.49	127	2954.99	1.94	8000

Performance plots were generated for BPT4000 and XIPS-25 thrusters at geostationary orbits. Figure-7-8 shows BPT4000 and XIPS-25, altitude against t_m plots, where mass was incrementally increased by 200kg up to 6000kg. Thrusters t_m increased on average by 35.68 and 57.6 days per increment for BPT4000 and XIPS-25 respectively.

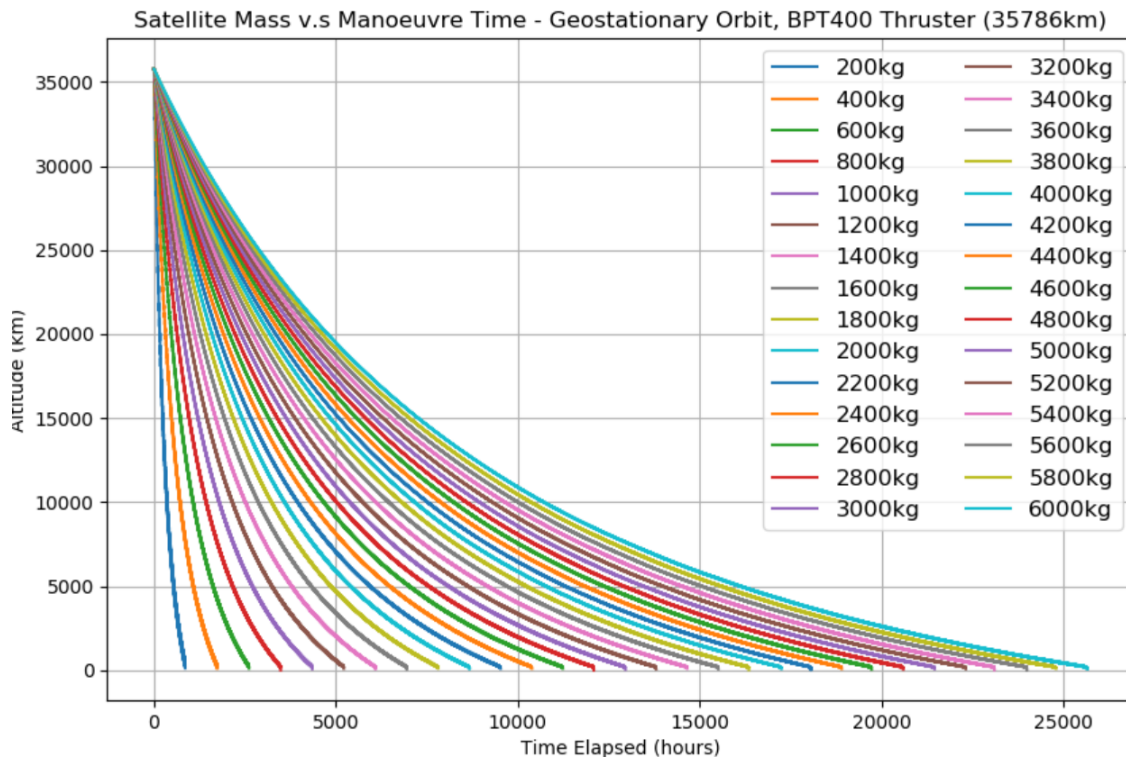


Figure 7 – Performance curve, showing how mass affects deorbit times

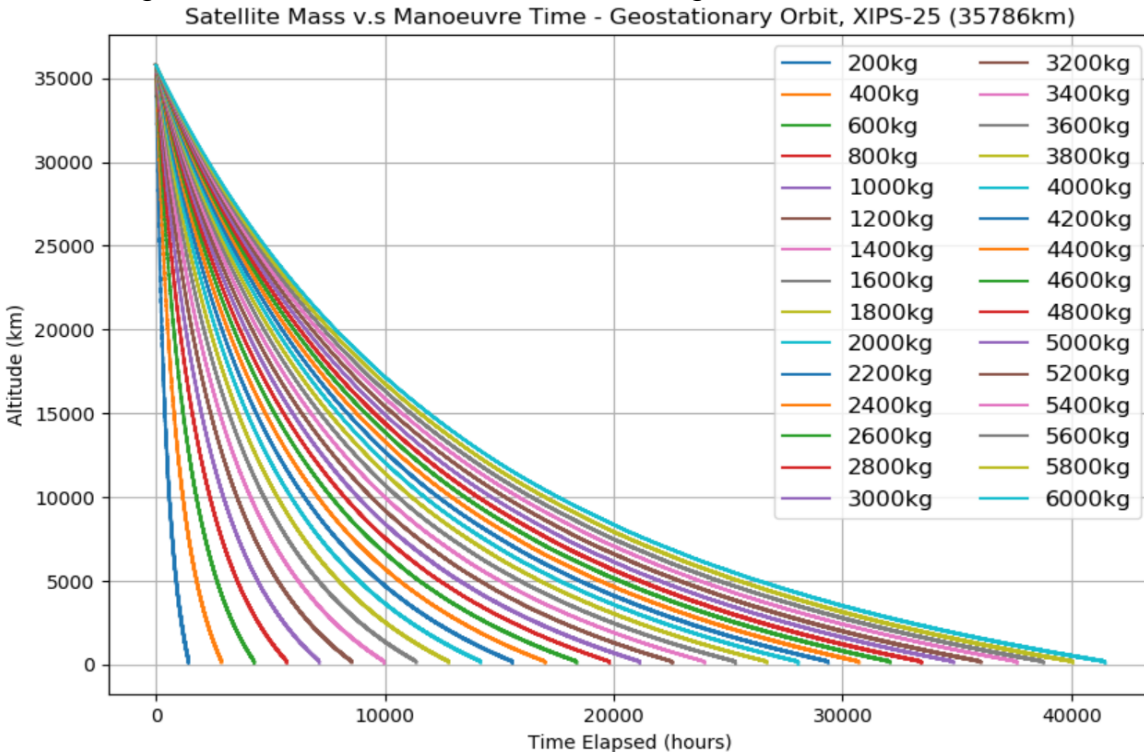


Figure 8 – Mass vs. time performance curve (GEO, XIPS-25)

4.2 Model Validation

The model was validated in order to confirm accuracy of results. Initial velocities were calculated analytically, and the model results, detailed in table-7, were printed to the console.

Table 7 – Model validation with initial velocity.

Velocity at Initial Altitude Verification					
Analytical Solution		Model Solution		Calculated Error	
Altitude (km)	Speed (km/s)	Altitude (km)	Speed (km/s)	ABS Error (km/s)	REL Error (%)
7825	5.29780	7825	5.29759	0.00021	0.0040
19100	3.95539	19100	3.95535	0.00036	0.00092
23222	3.66964	23222	3.66963	0.00016	0.00037
35786	3.07464	35786	3.07466	-0.00019	0.00063

The calculated absolute and relative errors shown in table-7 indicated less than 0.01% error in all recorded instances for initial velocity. The model was built and tested across the range of altitudes, mission ΔV was noted and was calculated analytically for the comparison below, table-8.

Table 8 – Model validation with total mission ΔV 's

Mission ΔV Verification					
Analytical Solution		Model Solution		Calculated Error	
Altitude (km)	Mission ΔV (km/s)	Altitude (km)	Mission ΔV (km/s)	ABS Error (km/s)	REL Error (%)
7825	2.4874	7825	2.4867	0.00073	0.029
19100	3.8298	19100	3.8289	0.00091	0.023
23222	4.1156	23222	4.1147	0.00093	0.022
35786	4.7106	35786	4.7096	0.00096	0.020

Mission ΔV errors between the analytical and model in the absence of perturbations, yielded an approximate relative error of 0.0242%.

5.0 Discussion

5.1 Model Limitations

Errors outlined in Section-4.2 indicated that results gained are highly accurate and, in all instances, yield below 0.01% relative error between analytical and model solutions. However, there were inherent limitations with the model that were abstract and more difficult to quantify – e.g. utilising velocity thrust vectoring, which although appropriate for this estimation, is not the optimal method of transfer. Furthermore, the range of perturbations modelled were limited to the J2 effect and aerodynamic-drag, as they exert the most noticeable perturbation-effects on the satellite. However, given the length of such manoeuvres, there exists a host of J parameters where, in the interest of greater precision, it would be prudent to model [31]. Further simulations could be undertaken to account for eclipse periods, more J parameters, the moon's gravity alongside the implementation of solar-radiation pressure effects. One limitation of deorbiting in this manner would be the manoeuvring of a satellite through debris-dense zones with reduced attitude control capacity, which, may in turn contribute to the problem.

5.2 Thruster Evaluation

The PPS1350 was unsuitable for the range of required manoeuvres. At 7825km, three thrusters (table-3) could perform the manoeuvre, as their maximum burn-time exceeded the t_m . However, at higher altitudes (table-4-6) SPT100D exceeded its burn-time, hence BPT4000 and XIPS-25 were the only thrusters capable of performing the manoeuvre across all altitudes. BPT4000 can supply 41.07% more thrust and is suitable for manoeuvring heavier satellites but requires 170kg more fuel than XIPS-25 to perform a GEO manoeuvre for a 2000kg satellite, conversely, XIPS-25 improved fuel efficiency comes at the expense of greater energy requirements and increased t_m .

This study only simulated single thrusters in operation but in many instances multiple thrusters are clustered together to increase thrust [32]. Clustered configurations were not considered in this work, but their advantages were noted, for comparison the PPS1350 was arranged in a two-thruster arrangement and compared to the XIP-25.

Table 9 - XIPS-25 with PPS1350 (x2) to highlight the effect of clustering.

Thruster Types	Power (W)	Impulse (sec)	Thrust (mN)	Efficiency (%)	Mass (kg)	Run-Time (hr)
XIPS-25 (x1)	4250	3550	165	67	13.7	13370
PPS1350 (x2)	2800	1660	180	55	10.6	9500

Table-9 shows the PPS1350 in a clustered arrangement against XIPS25. PPS1350 remained limited by lower efficiency, maximum runtime and 46.8% of XIPS-25s I_{sp} but PPS1350 requires 15.55W/mN where the XIPS-25 requires 25.75W/mN. The two-thruster configuration yields greater thrust than the XIPS at a significantly lower power, this indicated that the clustered PPS1350 and various smaller systems may be suitable in cluster arrangements. Finally, it was noted that performance curves in figure-7-8 indicated failure to deorbit within max burn-time occurred at approximately 2100kg.

5.3 Power Source

Energy required (E_m) calculated in table-3-6 excluded the use of batteries to power thrusters. An optimistic average of space-qualified lithium-ion batteries yielded power-densities of approximately $250\text{Wh}.\text{kg}^{-1}$ [33]. Given the duration of the missions, the power-supply mass would vary between 70-205 metric-ton.

Solar-arrays were a suitable candidate to generate adequate power. Gallium-arsenide cells (GaAs) are favoured over crystalline silicone in space due to higher efficiencies, and greater resistance to radiation which ensures slower degradation [34]. 3-Junction cell-arrays yield an energy-density of 321Wm^{-2} which meant that the manoeuvre would require $7.8\text{-}14.02\text{m}^2$ of coverage, which would incur additional mass of 90-165kg, if the system was to be an autonomously powered. However, mass-penalties would be avoided if the satellite had enough power available at the end of mission, but must be appropriately oversized to account for redundancies and failures [35].

5.4 Cost Benefit Analysis.

Mass and cost are inextricably linked for space-borne systems. Equation-28 was used to determine ΔV_H for the given altitudes, outputs were then substituted into the Tsiolkovsky Rocket equation [36]. This allowed for the calculation of propellant mass required for an equivalent CP mission, the results were plotted in figure-9.

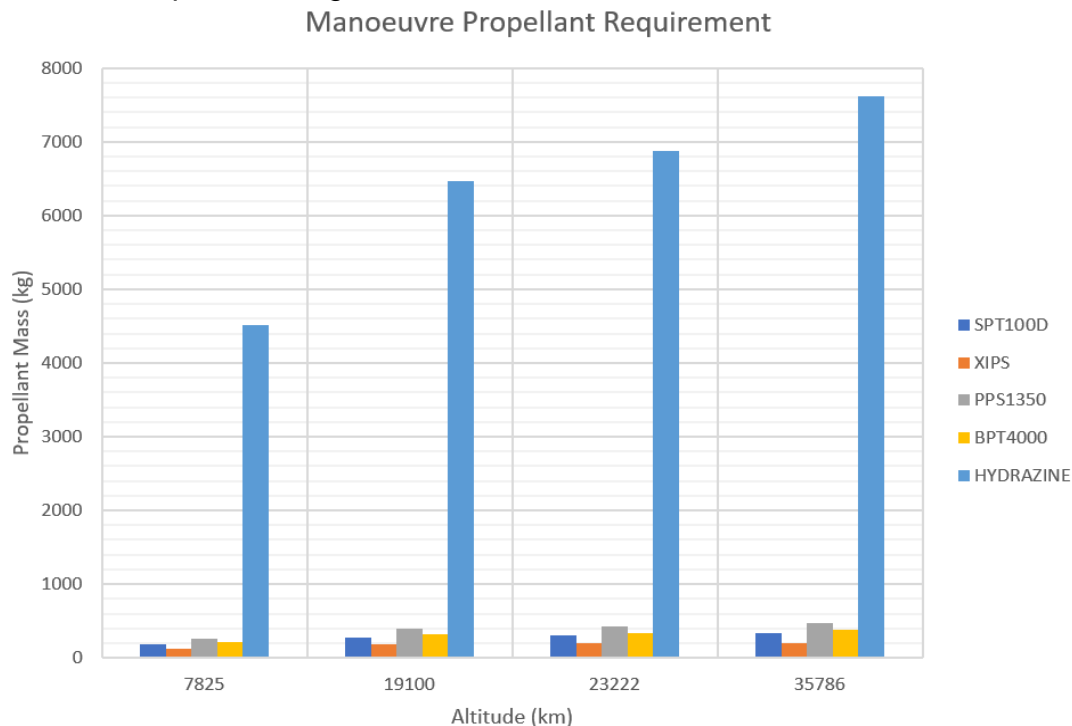


Figure 9 - Propellant mass requirements at tested altitudes for EP & CP.

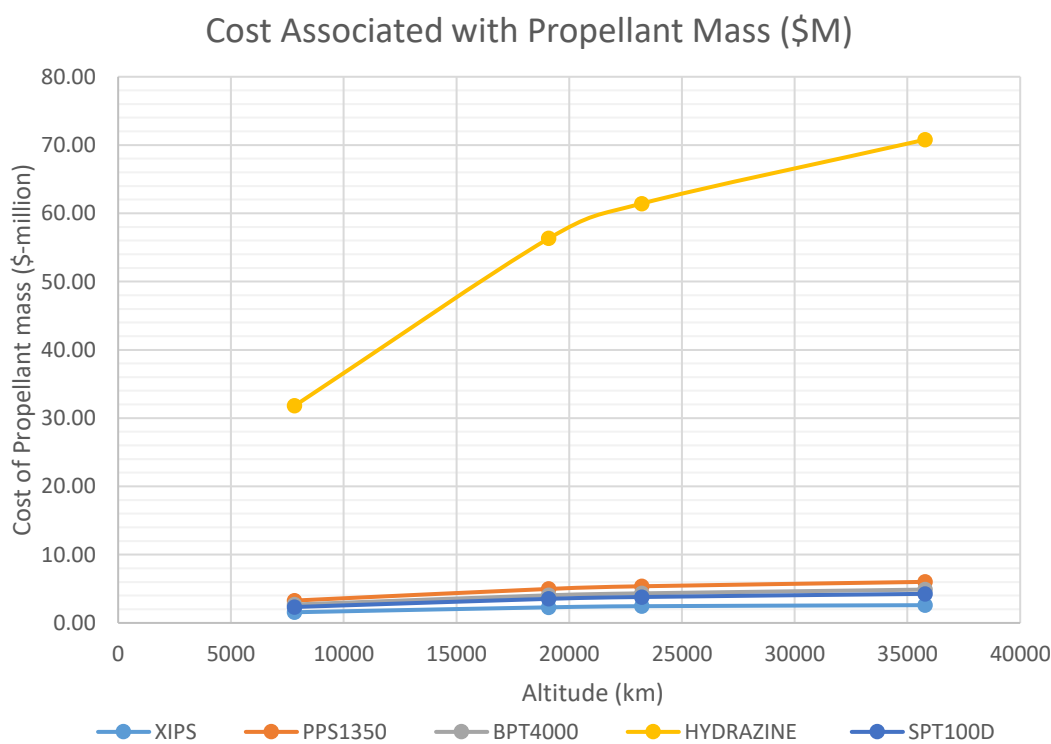


Figure 10 – Costs associated with launching propellant across tested altitudes

It was assumed the 2000kg satellite was launched into a transfer orbit with a Falcon-9 rocket [37]. The \$/kg (USD) to launch for a Falcon-9 was calculated as 12,618.55\$/kg. Figure-10 displays propellant-cost associated with launch. As expected, the largest propellant-cost was incurred at GEO where EP exceeded \$6M, and a hydrazine CP thruster exceeded \$70M which made CP unfeasible for use [37]. Therefore, EP incurred an average propellant saving of 94.2%, yielding \$30-65M savings across tested altitudes. The analysis relates explicitly to launching extra-propellant, and does not pertain to costing the associated technologies.

6.0 Conclusions

The study concluded that EP systems were adequate to manoeuvre a 2000kg MEO and GEO end-of-life satellite to a final orbit of 200km, while conforming with the 25-year mitigation rule, under constant thrust conditions. EP systems would significantly reduce propellant-mass requirements. The propellant-saving could be used to improve payload capacity or reduce propellant costs by at least a factor of ten. BPT4000 and XIPS-25 were the only thrusters capable of performing across all altitudes. Their use would require a trade-off between t_m and propellant savings. While BPT4000 and XIPS-25 were the most appropriate single thrusters, the advantages of clustering smaller thrusters in parallel may yield improved t_m over larger single thrusters. In any case, solar arrays seem the most cost-effective, mission-ready solution in terms of generating power for the manoeuvre. Battery systems were deemed too heavy. Model verification indicated an accuracy greater than 99.99%, but given the timescale of manoeuvres, further-work undertaken would account for all J-parameter perturbations, moons-gravity and solar-radiation pressure to gain a higher degree of accuracy. Furthermore, it would be prudent that further work would include a proposed optimal transfer manoeuvre. Lastly, further work must consider the effectiveness of the ageing control system tasked to react in mitigating further risk of collisions while passing through critical altitudes.

7.0 References

- [1] D. Kessler and B. Cour-Palais, “Collision frequency of artificial satellites: The creation of a debris belt,” *Journal of Geophysical Research*, vol. 83, no. (A6), p. p.2637., 1978..
- [2] Anselmo, P. (ASI), Crowther, T.-S. (BNSC), Alby, Baccini, B. (CNES), A. (DLR), Flury, Jehn and K. (ESA), “European Code of Conduct for Space Debris Mitigation”, no. Issue 2, p. p.6, 2007.
- [3] NASA, “Technical Standard: Process for limiting orbital debris P.41,” National Aeronautics and Space Administation , 25 04 2019. [Online]. Available: file:///C:/Users/gary-/Downloads/nasa-std-8719.14b.pdf. [Accessed 21 03 2020].
- [4] J. M. Lafferty, Foundations of vacuum science and technology, New York, N.Y.: J. Wiley and Sons, 1998.
- [5] R. G. Jahn, Physics of Electric Propulsion, Mineola, New York: Dover Publications, 2012.
- [6] E. Stuhlinger, Ion propulsion for space flight, New York: McGraw-Hill, 1964.
- [7] George P Sutton and O. Biblarz, “Electric Propulsion,” in *Rocket Propulsion Elements*, Hoboken, New Jersey, Wiley Interscience, 2010, pp. p.622-658.
- [8] E. P. Division, “Satellite Power Systems,” Technology Programmes in Space, [Online]. Available: <http://www.esa.int/esapub/br/br202/br202.pdf>. [Accessed 24 02 2020].
- [9] NASA, “The Prius of Space,” NASA Jet Propulsion Laboratory, September 2007. [Online]. Available: <https://www.jpl.nasa.gov/news/?feature=1468>. [Accessed 26 02 2020].
- [10] W. B. Machine, “Asteroid explorer Hayabusa-mounted ion engin,” Internet Archive , 2015. [Online]. Available: <https://web.archive.org/web/20060819093452/http://www.ep.isas.ac.jp/muses-c/>. [Accessed 03 03 2020].
- [11] J. S. Sovey, V. K. Rawlin and M. J. Patterson, “Ion Propulsion Development project in US. Space Electric Rocket Test I to Deep

- Space 1," *Journal of Propulsion and Space* , vol. Volume 17, no. 3, pp. P.517-526, 2001.
- [12] R. A. C. Schonenberg and H. F. R. Schoyer, "Solid Propulsion De-orbiting and Re-orbiting," *NASA Astrophysics Data System* , p. p.67, 03 01 2009.
- [13] MIT, "Analytical Approximations for Low Thrust Maneuvers," *MIT Openware*, vol. <https://ocw.mit.edu/index.htm>, p. p.3, 2015.
- [14] T. Oliphant and P. Pearu, "ntegration and ODEs (scipy.integrate)," SciPy, 2001. [Online]. Available: <https://docs.scipy.org/doc/scipy/reference/integrate.html>. [Accessed 20 10 2020].
- [15] T. Oliphant, "NumPy v1.19.dev0 Manual," NumPy, 2006. [Online]. Available: <https://numpy.org/>. [Accessed 1 09 2020].
- [16] R. Battin, An Introduction to the Mathematics and Methods of Astrodynamics, NY: AIAA, 1999.
- [17] F. A. Tewari, Atmospheric and Spaceflight Dynamics, Modelling and Simulations with MATLAB and SIMULINK, New York: Springer, 2007.
- [18] J. C. Butcher, "Adams Method," in *Numerical Methods for Ordinary Differential Equations*, Hoboken, Ney Jersey, Wiley, 2003, pp. p105-121.
- [19] P. J. Montenbruck and G. Eberhand, "Keplarian Orbital Elements," in *Satellite Orbits: Models, Methods, Applications.*, New York, Springer, Heidelberg, 2005, p. p28.
- [20] R. Schwarz, "Cartesian State Vectors > Keplerian Orbit Elements (Memorandum #2)," 2017. [Online]. Available: rene-schwarz.com. [Accessed 13 1 2020].
- [21] H. Curtis, "Section 4.7," in *Orbital Mechanics for Engineering Students*, London, Heinemann, 2005, pp. p.177-181.
- [22] H. J. Anton , C. De Ruite and J. R. Forbes, Spacecraft dynamics and control : an introduction, Hoboken, Ney York: Wiley, 2012.
- [23] National Aeronautics and Space Administration,, "The Drag Equation - Glen Research Centre," Glen Research Centre, 2012. [Online].

Available: <https://www.grc.nasa.gov/www/k-12/airplane/drageq.html>. [Accessed 17 01 2020].

- [24] D. M. Prieto, B. P. Graziano and P. C. E. Roberts, "Spacecraft Drag Modelling," *Progress in Aerospace Sciences*, pp. p 2-3, 2016.
- [25] National Aeroautics and Space Administration, "US Standard Atmosphere 1976," NASA, 10 1976. [Online]. Available: <https://ntrs.nasa.gov/archive/nasa/casi.ntrs.nasa.gov/19770009539.pdf> . [Accessed 05 02 2020].
- [26] A. M. Society, "Glossary of Meteorology: Scale Height," American Meteorological Society , 2012. [Online]. Available: http://glossary.ametsoc.org/wiki/Scale_height. [Accessed 12 02 2020].
- [27] S.-H. Chen, "ATM60 - Coriolis Effect," University of California Davis, 2013.
- [28] R. G. Jahn and E. Y. Choueiri, "Electric Propulsion Encyclopedia," *Encyclopedia of Physical Science and Technology*, vol. Volume 5, no. Third edition, pp. p.125-137, 2002.
- [29] T. S. Kelso, "Active elements," Celestrak, 01 03 2020. [Online]. Available: <https://www.celestrak.com/Norad/elements/active.txt>. [Accessed 02 03 2020].
- [30] F. Covello, "Application of electrical propulsion for an active debris removal system: a system engineering approach.,," *Advances in Space Research (COSPAR)*, vol. 50, no. 918-931, pp. P.3-5, 2012.
- [31] A. Ionel, "Performance evaluation of propulsion systems as LEO deorbiting devices," *INCAS - National Institute for Aerospace Research*, vol. 9, no. 3, pp. p.55-69, 2017.
- [32] A. Gaudel, C. Hourtolle, J. F. Goester and M. Ottavianni, "De-orbit strategies with Low Thrust Propulsion," in *Mission Architecture For Active Space Debris Removal Using The Example of SL-8 Rocket Bodies*, Hoboken, Springer, 2015, pp. P.55-59.
- [33] S. Luong, "What is a lithium-ion battery and how does it work?," Clean Energy Institute - University of Washington, 2020. [Online]. Available: <https://www.cei.washington.edu/education/science-of-solar/battery-technology/>. [Accessed 2020 03 09].

- [34] S. Bailey and R. Ryne, "Operation of Solar Cells in a Space Environment," in *Practical Handbook of Photovoltaics*, Amsterdam, Elseveir, 2012, pp. p.863-870.
- [35] M. A. V, "GaAs and highly efficient space cells," in *Practical Handbook of Photovoltaics: Fundamentals and Applications*, Amsterdam, Elseveir, 2012, pp. p.319-413.
- [36] D. Pettit, "The Tyranny of the Rocket Equation," NASA, 05 01 2012. [Online]. Available:
https://www.nasa.gov/mission_pages/station/expeditions/expedition30/tyranny.html. [Accessed 2020 02 25].
- [37] SpaceX, "Capabilities & Services," SpaceX, [Online]. Available:
<https://www.spacex.com/about/capabilities>. [Accessed 15 03 2020].
- [38] D. M. Goebel, "Ion & Hall Thrusters," in *Fundamentals of electric propulsion*, Hoboken, NJ, Wiley, 2008.

8.0 Appendices

8.1 Source-code Hyperlink

<https://github.com/Gary-stewart1992/GS-ME409>

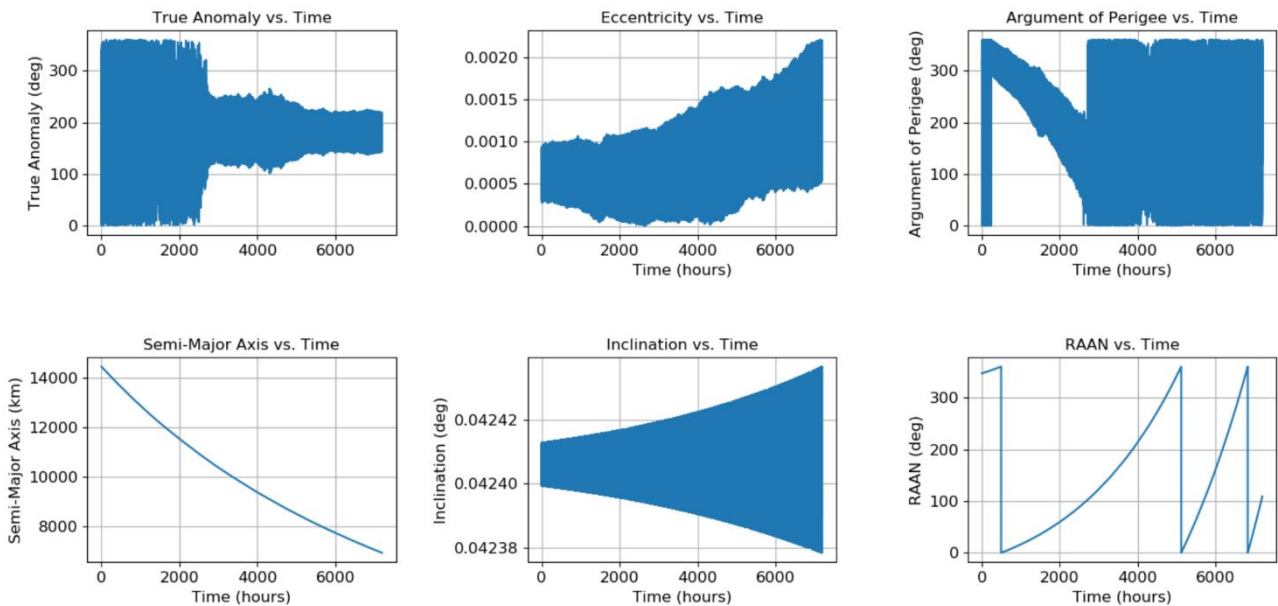
(The source code far exceeds the two-page appendix limit, so could not be placed within this work)

8.2 Satellite Details

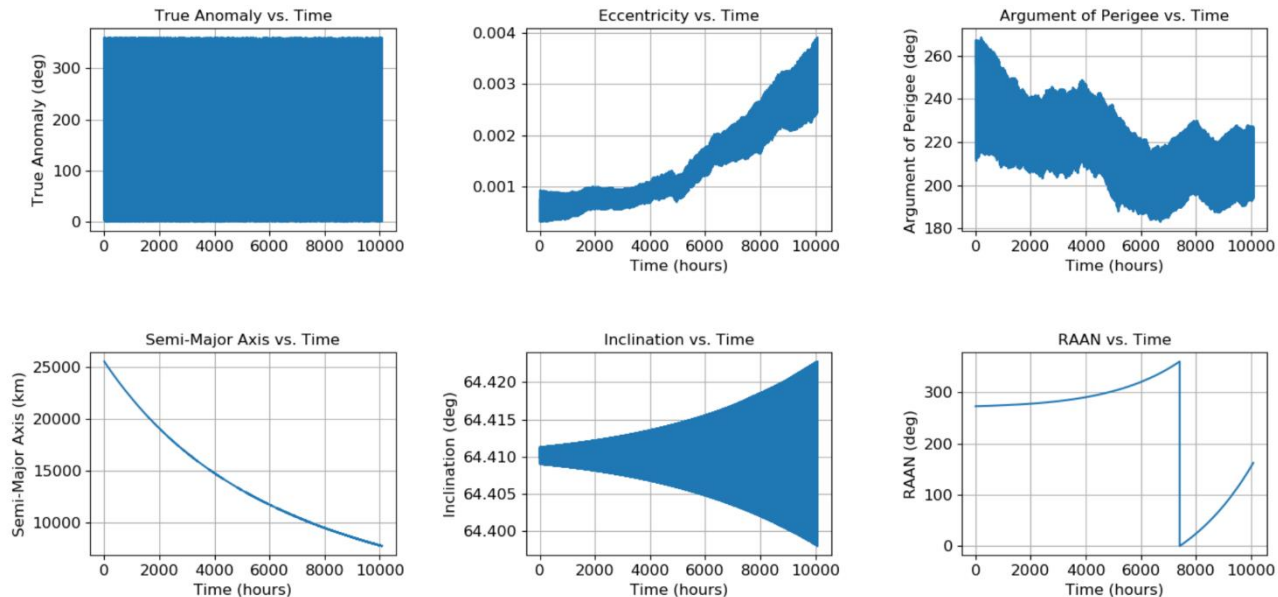
Devised Satellite Details			
Satellite Name	Dry Mass (kg)	Satellite Cross-section (m ²)	Coefficient of Drag
Sat-1	2000	5.60E-06	2.2

8.3 Auxiliary Orbital Element plots

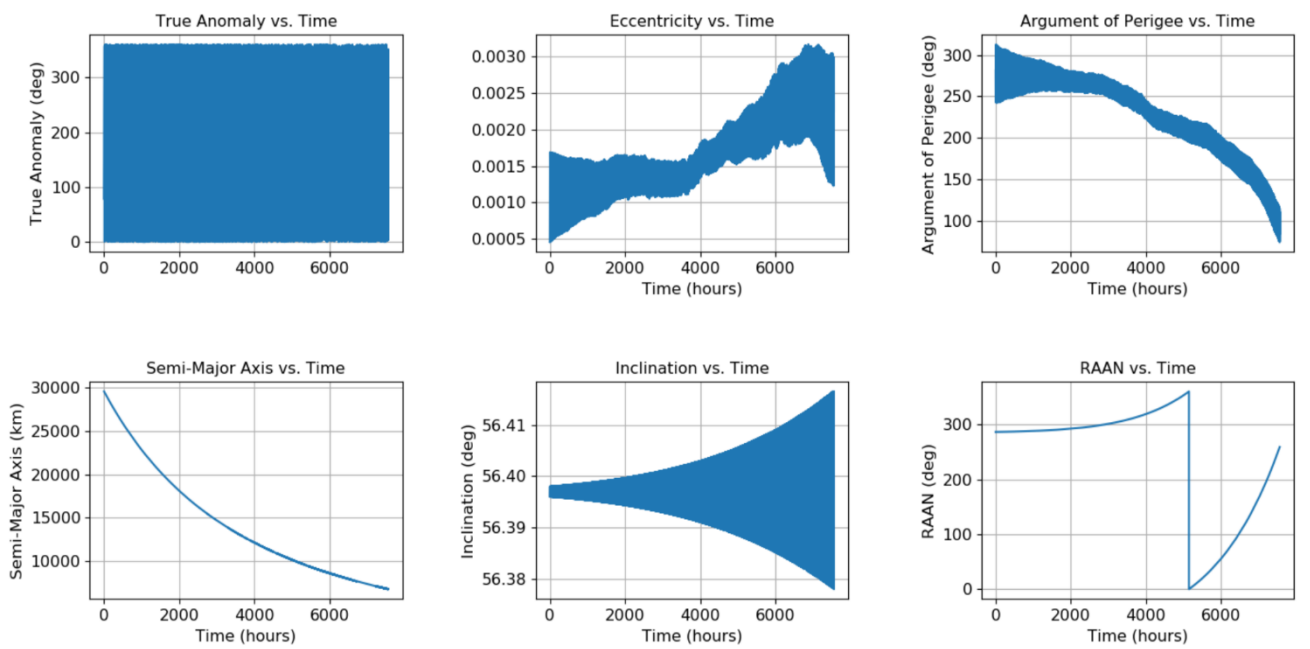
Change In COES at 7825km with XIPS-25



Change In COES at 19100km with XIPS-25



Change In COEs at 23222km with BPT4000



Change In COEs at 35786km with BPT4000

